Cell

Mutation of a U2 snRNA Gene Causes Global Disruption of Alternative Splicing and Neurodegeneration

Yichang Jia,[1] John C. Mu,[2] and Susan L. Ackerman[1,*]
[1]Howard Hughes Medical Institute and The Jackson Laboratory, 600 Main Street, Bar Harbor, ME 04609, USA
[2]Department of Electrical Engineering, Stanford University, Stanford, CA 94305-4065, USA
*Correspondence: susan.ackerman@jax.org
DOI 10.1016/j.cell.2011.11.057

SUMMARY

Although uridine-rich small nuclear RNAs (U-snRNAs) are essential for pre-mRNA splicing, little is known regarding their function in the regulation of alternative splicing or of the biological consequences of their dysfunction in mammals. Here, we demonstrate that mutation of *Rnu2-8*, one of the mouse multicopy U2 snRNA genes, causes ataxia and neurodegeneration. Coincident with the observed pathology, the level of mutant U2 RNAs was highest in the cerebellum and increased after granule neuron maturation. Furthermore, neuron loss was strongly dependent on the dosage of mutant and wild-type snRNA genes. Comprehensive transcriptome analysis identified a group of alternative splicing events, including the splicing of small introns, which were disrupted in the mutant cerebellum. Our results suggest that the expression of mammalian U2 snRNA genes, previously presumed to be ubiquitous, is spatially and temporally regulated, and dysfunction of a single U2 snRNA causes neuron degeneration through distortion of pre-mRNA splicing.

INTRODUCTION

Splicing of pre-mRNAs is performed by the spliceosome machinery consisting of numerous proteins and five small nuclear RNAs (snRNAs) (Wahl et al., 2009). Assembly of the major spliceosome, responsible for splicing of over 90% of human pre-mRNAs, begins with the recruitment of U1 snRNPs (small nuclear ribonucleoprotein particles) to the pre-mRNA 5′ exon/intron junction via base pairing of the U1 snRNA with the splice site. U2 snRNPs subsequently bind to the pre-mRNA branchpoint sequence (BPS) near the 3′ intron boundary, also in part via base-pairing interactions. Further remodeling of the spliceosome results in the recruitment of additional snRNPs, including U6 snRNPs that will replace U1 snRNPs at 5′ pre-mRNA splice sites. Base pairing of U6 with U2 snRNAs juxtaposes the 5′ splice site and the BPS, the reactants of the first transesterification reaction. Thus, recognition and removal of introns and subsequent exon ligation depend in part on the dynamic base pairing of snRNAs with pre-mRNAs and with each other.

Given the critical importance of pre-mRNA splicing to the regulation of gene expression and proteome diversity, it follows that mutations in RNA-processing proteins that may influence pre-mRNA splicing cause human disease (Cooper et al., 2009; Licatalosi and Darnell, 2006). Indeed, dominant mutations in multiple ubiquitously expressed protein components of the U4/U5/U6 tri-snRNP cause retinitis pigmentosa (Mordes et al., 2006). Mutations in the *SMN1* (survival of motor neuron 1) gene, which encodes a protein essential for U snRNP biogenesis, cause motor neuron degeneration in patients with spinal muscular atrophy (SMA) (Lefebvre et al., 1995). Although *SMN* is ubiquitously expressed, alterations in the levels of individual snRNAs and numerous aberrant transcripts were observed in a tissue-specific fashion in *SMN*-deficient mice (Zhang et al., 2008). Mutations in genes encoding the ubiquitously expressed DNA/RNA-binding proteins, TDP-43 and FUS/TLS, are associated with some cases of familial and sporadic amyotrophic lateral sclerosis and frontotemporal dementia (Lagier-Tourenne et al., 2010; Lemmens et al., 2010). Recent studies demonstrated that decreased expression or altered subcellular localization of TDP-43 resulted in reduced expression and altered splicing of multiple mRNAs (Polymenidou et al., 2011; Tollervey et al., 2011). These findings strongly implicate alterations in RNA processing as a key event in several neurodegenerative disorders. However, given the multiple functions of these proteins, the pathogenic basis of these diseases remains unclear.

Recently, mutations in the gene encoding U4atac snRNA, a component of the minor spliceosome that splices a restricted (U12-dependent) class of introns found in less than 1% of human genes, have been linked to the developmental disorder microcephalic osteodysplastic primordial dwarfism (Edery et al., 2011; He et al., 2011). However, to date, mutations in the major spliceosomal snRNA genes have not been associated with disease, perhaps in part due to their ubiquitous expression and essential function. Furthermore, unlike the *U4atac* gene, the snRNAs of the major spliceosome are encoded by multiple genes and pseudogenes in metazoans (Marz et al., 2008), suggesting that these genes are highly redundant. Although differing in organization (e.g., U1 and U2 genes exist in large chromosomal

clusters in the human genome, whereas other snRNA genes are not clustered; Manser and Gesteland, 1982; Van Arsdell and Weiner, 1984; Westin et al., 1984), sequence analysis of snRNA genes suggests that they have apparently undergone concerted evolution, i.e., members of gene families are identical or nearly so within a species (Marz et al., 2008; Pavelitz et al., 1995). However, the effect of polymorphisms in individual members of these repetitive gene families on pre-mRNA splicing and the extent to which the expression of single genes is independently regulated are largely unknown.

Here, we report that a 5 nucleotide (nt) deletion in one member of a cluster of mouse U2 snRNA genes causes neurodegeneration and alternative splicing defects, including the retention of small introns. Our study provides definitive evidence for the causative role of splicing dysfunction in neurodegeneration and a model to dissect the role of major spliceosomal snRNAs on the regulation of mammalian pre-mRNA splicing.

RESULTS

Progressive Neurodegeneration in *NMF291* Mutant Mice

The *NMF* (Neuroscience Mutagenesis Facility) *291* mutation was identified in a chemical mutagenesis screen for recessive mutations that result in neurological phenotypes (Bult et al., 2004). Mice homozygous for this mutation developed mild tremors by 8 weeks of age, which progressed to overt truncal ataxia by 12 weeks (see Movie S1 available online). At 4 weeks of age, the brains of mutant mice appeared grossly normal (Figures S1A–S1D). However, histological analysis revealed granule cells with pyknotic nuclei in the mutant cerebellum beginning at 4 weeks of age (data not shown). Neuron loss was progressive, and by 4 months of age, most granule cells had degenerated (Figures 1A–1F). However, other cerebellar neurons, including Purkinje cells, did not degenerate, even in aged mice (data not shown). Although neuron death was most severe in the cerebellum, later-onset degeneration of granule cells in the dentate gyrus region of the hippocampus was also observed (Figures S1E–S1H).

To determine the nature of neuron death, immunostaining with activated caspase-3 antibodies was performed on cerebellar sections from 6-week-old mice. Many immunopositive granule cells were observed in the mutant, but not the wild-type (WT) cerebellum, suggesting that mutant neurons undergo apoptosis (Figures 1G and 1H). Granule cell apoptosis was confirmed by TUNEL (TdT-mediated dUTP nick end labeling) analysis (Figures 1I and 1J).

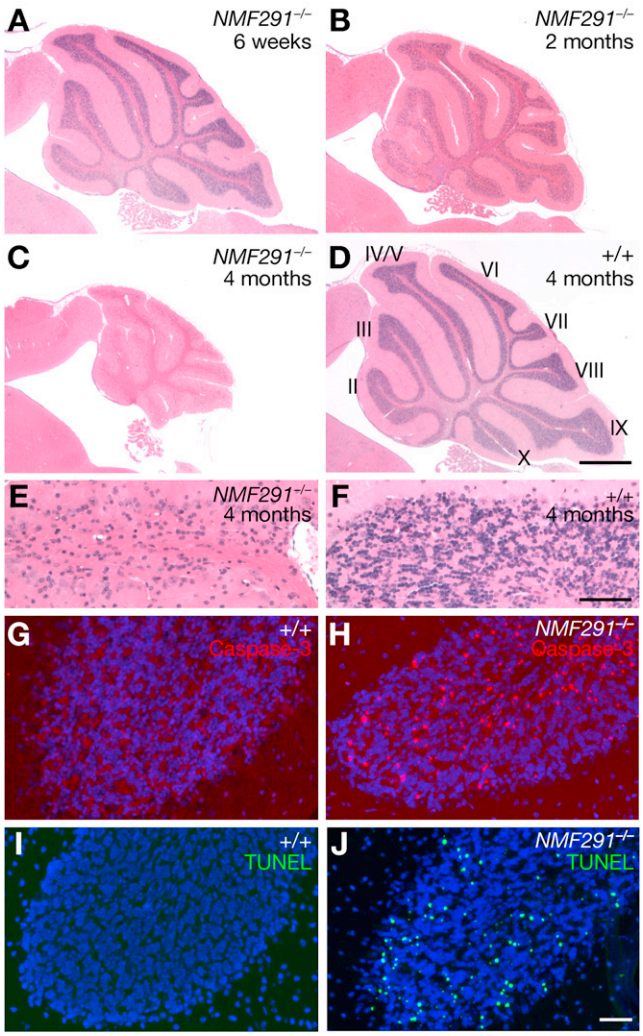

Figure 1. Progressive Granule Cell Degeneration in the *NMF291*$^{-/-}$ Cerebellum

(A–F) Hematoxylin and eosin-stained sagittal sections of WT (+/+) and *NMF291*$^{-/-}$ cerebella. Cerebellar lobules are indicated by Roman numerals (D). (E and F) Higher-magnification images of lobule IV/V from (C) and (D).

(G–J) Cleaved caspase-3 immunostaining (G and H) and TUNEL analysis (I and J) of sections from 6-week-old cerebella. Sections were counterstained with Hoechst 33342.

Scale bars, 500 μm (D), 50 μm (F), and 10 μm (J). See also Figure S1 and Movie S1.

The *NMF291* Mutation Deletes 5 nt in the *Rnu2-8* U2 snRNA

The *NMF291* mutation was initially localized to distal Chromosome 11 by a genome scan analysis of F2 mice using polymorphic microsatellite markers. Additional recombination mapping narrowed the mutation interval to a 0.52 cM (0.34 Mb) region between *D11Mit200* and *D11Mit199* containing eight protein-coding genes (Figures 2A, 2B, and S2A). No coding sequence polymorphisms between mutant and WT DNA were found in these genes, nor did we observe differences in the expression of the cerebellar transcripts of these genes between genotypes (data not shown).

In addition to the protein-coding genes, a cluster of five U2 snRNA (*Rnu2-6* to *Rnu2-10*) genes also resides in the *NMF291* critical interval (Figure 2B). The RNAs encoded by these genes are identical, except for a single nucleotide polymorphism in *Rnu2-6* (Figure S2B). Sequencing of mutant genomic DNA revealed a 5 bp deletion between nt 30 and 34 (30AGUGU34) in a highly conserved region of the *Rnu2-8* transcription unit (Figures 2C and 2D). This deletion removes the first 2 nt of the U2 consensus branch site recognition sequence (BSRS)

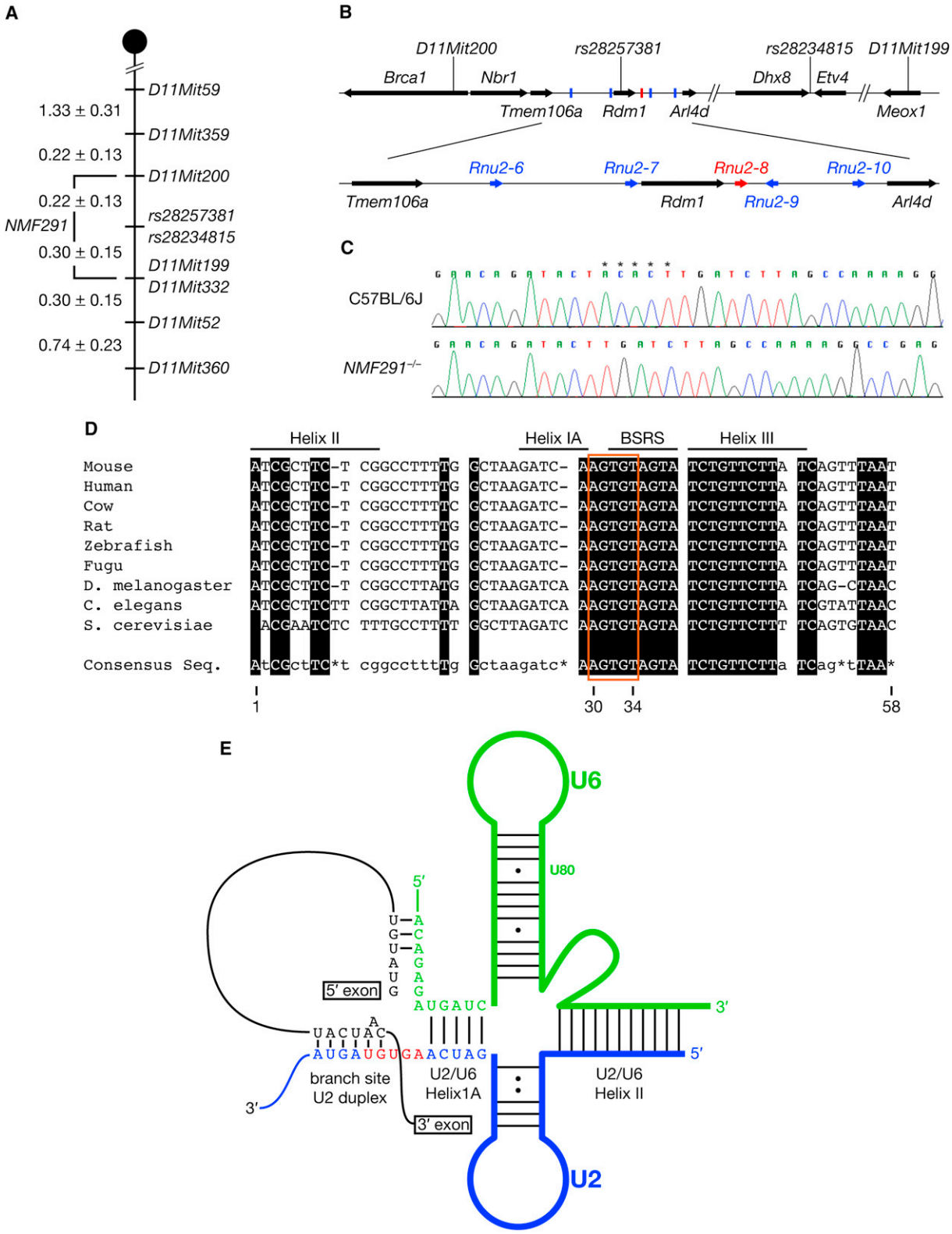

Figure 2. The *NMF291* Mutation Is a 5 nt Deletion in a U2 snRNA Gene

(A) The *NMF291* mutation was mapped to Chromosome 11 between *D11Mit200* and *D11Mit199* (values are in cM ± SEM).

(B) The *NMF291* critical interval contains eight protein-coding genes (arrows) and five U2 snRNA genes (*Rnu2-6*–*Rnu2-10*; bars, top panel).

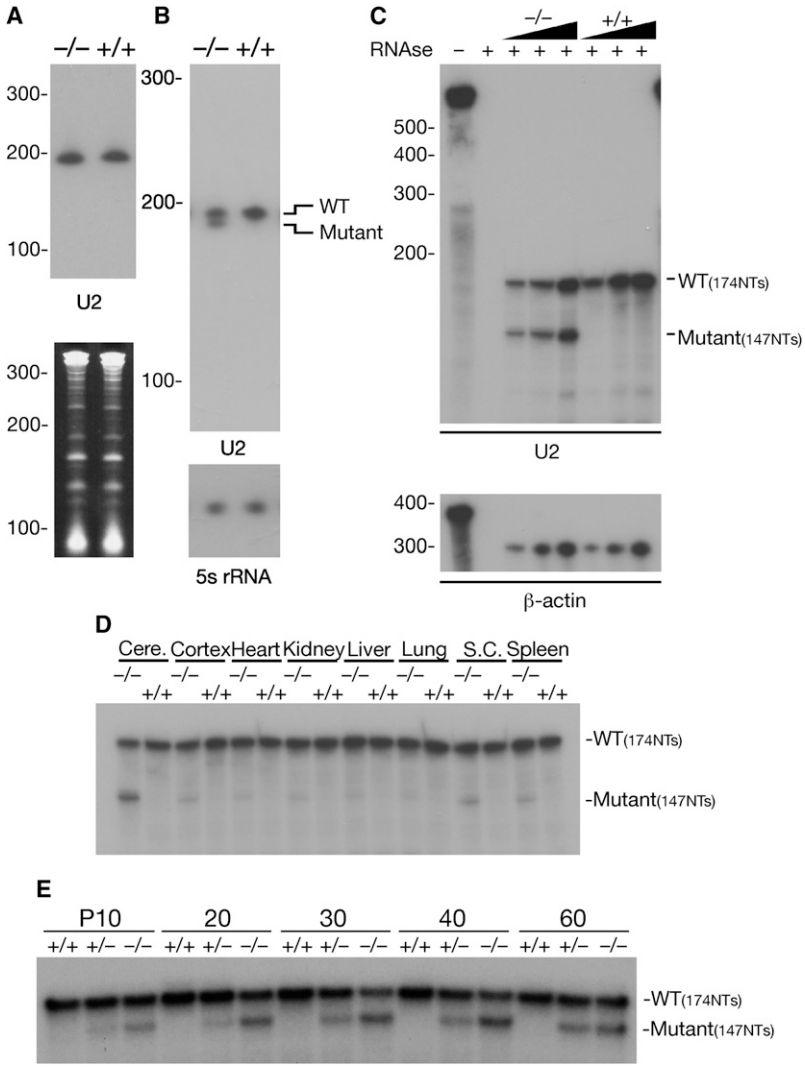

Figure 3. The Expression of *Rnu2-8* Is Temporally and Spatially Regulated

(A and B) Total RNA from WT and *NMF291*$^{-/-}$ (−/−) P30 cerebella was separated by denaturing acrylamide gels for shorter (A) or longer (B) periods and subsequently analyzed by northern blot analysis using an U2-specific oligonucleotide probe. For loading controls, the gel was stained with ethidium bromide (A, bottom), or the membrane was rehybridized with a probe for 5S rRNA (B).

(C) RPA using increasing amounts of cerebellar RNA (0.2–1 μg) from P30 WT and *NMF291*$^{-/-}$ mice. For loading controls, RPA was also performed using a β-actin RNA probe.

(D) RPA analysis of U2 snRNAs in various tissues taken from P30 WT and *NMF291*$^{-/-}$ mice.

(E) RPA analysis of U2 snRNAs in WT, *NMF291*$^{+/-}$ (+/−), and *NMF291*$^{-/-}$ cerebella at different postnatal (P) ages (days after birth). Cere., cerebellum; S.C., spinal cord.

See also Figure S3.

RNase protection assays (RPAs) using cerebellar RNA isolated from P30 WT and mutant mice. Total U2 snRNA levels were similar between the WT and the *NMF291*$^{-/-}$ cerebellum (Figure 3A), and both WT and the deletion-containing *Rnu2-8* RNAs were detected in the mutant cerebellum (Figures 3B and 3C), with the mutant transcript found at 78.9% ± 6.3% (n = 6) of the level of the WT U2 snRNA (or ~45% of total U2 levels). Similar analysis of highly pure granule cell cultures demonstrated that both WT and mutant U2 RNAs were expressed within the same cell type (data not shown). Finally, immunoprecipitation experiments using Y12 antibody, which precipitates U snRNPs (Lerner et al., 1981), demonstrated that the mutant U2 snRNAs were assembled into mutant cerebellar U2 snRNPs (Figures S3A and S3B), consistent with previous reports that the free snRNA pool is relatively very small and unstable (Sauterer et al., 1988).

Mammalian U2 snRNAs, like other U snRNAs, are believed to be ubiquitously and highly expressed (Egloff et al., 2008; Hernandez, 2001). However, neurodegeneration in *NMF291*$^{-/-}$ mice was very distinct, with profound neuron loss occurring within the cerebellum beginning at P30. To determine if expression of mutant *Rnu2-8* correlates with the specificity of pathological changes, we performed RPA and northern blot assays using neuronal and non-neuronal tissues from the P30 WT and

(33GUAGUA38) and the 3 nt linker region (30AGU33) between the BSRS and U2/U6 helix IA (Figures 2D and 2E) (Wahl et al., 2009). The deletion was not observed in genomic DNA from several other inbred stains, including C57BL6/J and 129S4/SvJae, from which the F1 ES cells used for mutagenesis were derived (data not shown).

Rnu2-8 Is Spatially and Temporally Regulated

To confirm that the U2 gene disrupted by the *NMF291* deletion is indeed expressed, we performed northern blot analysis and

(C) Sequence chromatograms of WT (C57BL6/J) and mutant (*NMF291*$^{-/-}$) *Rnu2-8* genomic DNA amplified using unique primers outside of the transcription unit. Asterisk (*) indicates nucleotides deleted in the mutant genome.

(D) Deleted nucleotides are evolutionarily conserved. Conserved nucleotides are boxed in black and indicated in uppercase letters in the consensus sequence. Nucleotides with one or more mismatches or absent across species are indicated in the consensus sequence in lowercase letters or with an asterisk, respectively. The U2 BSRS, and the nucleotides in helices IA, II, and III, which base pair with U6 snRNA, are indicated. Nucleotides are numbered according to the mouse sequence.

(E) The schematic of RNA:RNA interactions contributing to the first step of splicing. The 5 nt deletion in *Rnu2-8* is highlighted in red.

See also Figure S2.

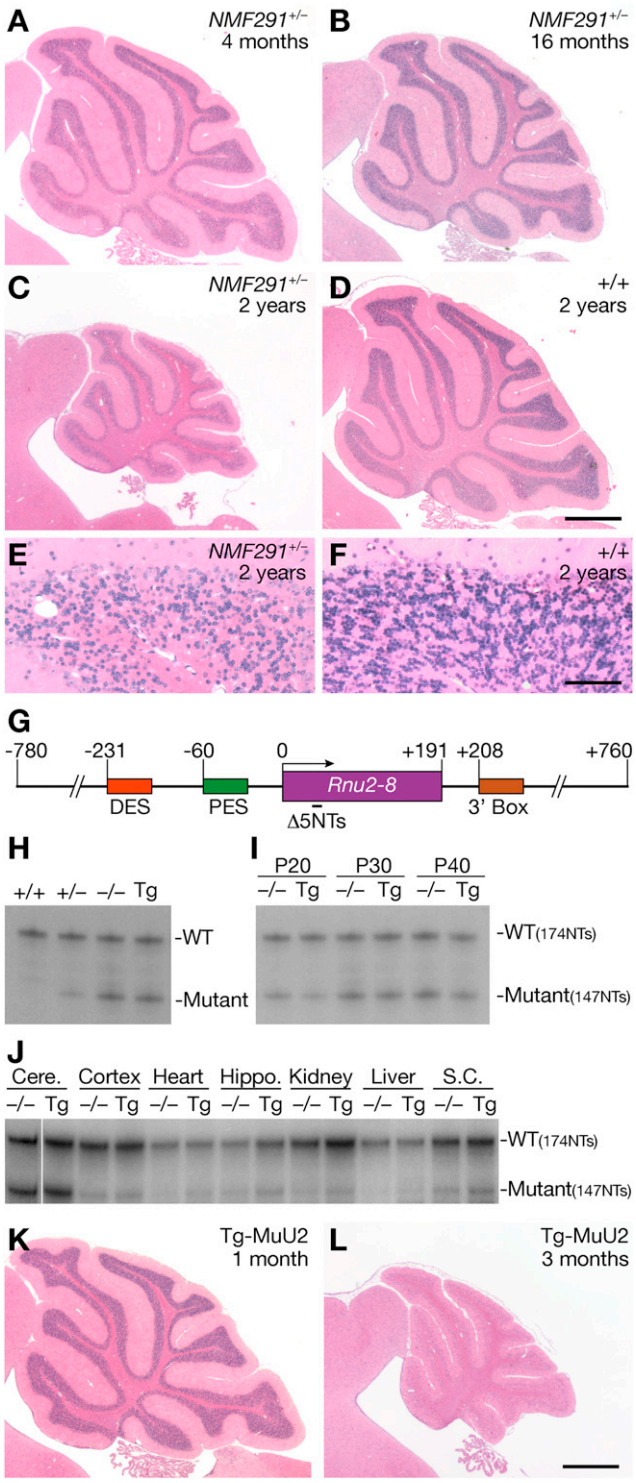

Figure 4. Mutant *Rnu2-8* Acts in a Dosage-Dependent Fashion on Neuron Survival

(A–F) Hematoxylin and eosin-stained sagittal sections of *NMF291*$^{+/-}$ and WT (+/+) cerebella. (E and F) Higher-magnification images of lobule IV/V from (C) and (D).

(G) The 1.5 kb DNA fragment, containing the transcription unit of the mutant *Rnu2-8* and its 5′ and 3′ flanking sequences, used for pronuclear injection.

(H) RPA analysis of cerebellar RNA from P30 WT, *NMF291*$^{+/-}$, *NMF291*$^{-/-}$ mice, and mice hemizygous for the mutant *Rnu2-8* transgene (Tg).

(I) RPA analysis of cerebellar RNA from P20, P30, and P40 *NMF291*$^{-/-}$ mice and mice hemizygous for the transgene (Tg).

(J) RPA analysis of tissues from P30 *NMF291*$^{-/-}$ and hemizygous Tg-MuU2 mice. Note that the *NMF291*$^{-/-}$ cerebellar lane was run on a separate gel.

(K and L) Hematoxylin and eosin-stained sagittal sections of Tg-MuU2 cerebella. DES, distal sequence element; PES, proximal sequence element. Scale bars, 500 μm (D and L) and 50 μm (F). See also Figure S4.

homozygous mutant mice (Figures 3D and S3C). Surprisingly, mutant *Rnu2-8* was differentially expressed between tissues, with highest levels observed in the cerebellum. Furthermore, mutant *Rnu2-8* expression was also temporally regulated in the postnatal cerebellum. Mutant U2 RNAs comprised ~20%–25% of the total U2 RNA levels in the P10 and P20 *NMF291*$^{-/-}$ cerebellum but rose to ~45% of the total level at P30 (Figures 3E, S3D, and S3E). This increase was maintained at P40 but dropped slightly at P60, likely due to neuron loss in the mutant cerebellum. This temporal regulation of expression was also observed in heterozygous mice, where amounts of mutant U2 RNA were approximately half of that observed in homozygous mice (Figures 3E and S3E). Together, these data suggest that mammalian U2 snRNAs display previously unsuspected temporal and spatial variation with the expression of mutant *Rnu2-8* correlating with the onset and specificity of neurodegeneration in the *NMF291*$^{-/-}$ mouse.

Mutant *Rnu2-8* Induces Neurodegeneration in a Dosage-Dependent Manner

Although mice homozygous for the *NMF291* mutation were originally ascertained in our screen, the site of the *Rnu2-8* deletion, the multicopy nature of the U2 genes, and the expression of WT U2 snRNAs in the mutant cerebellum suggested that this mutation might act in a gene dosage-dependent fashion. To investigate this possibility, we performed histological analysis of the cerebellum of *NMF291*$^{+/-}$ mice. Apoptotic granule cells were observed in the cerebellum of 1-month-old and older *NMF291*$^{+/-}$ mice, but the number of dying neurons was considerably reduced compared to that observed in homozygous *NMF291* mice (data not shown). Differences in the overall size of the *NMF291*$^{+/-}$ cerebellum were not obvious until mice were close to 2 years of age, when mild tremors were apparent, and histological analysis revealed that many granule cells had degenerated (Figures 4A–4F).

To further test the mechanism of the *Rnu2-8* mutation, we generated mice transgenic for a 1.5 kb genomic DNA fragment containing the mutant *Rnu2-8* transcriptional unit and the basal regulatory elements necessary for U2 transcription and processing (Figure 4G) (Egloff et al., 2008; Hernandez, 2001). Mice from one transgenic line (Tg-MuU2) expressed mutant *Rnu2-8* in the cerebellum, and expression was temporally and spatially regulated similar to that observed in *NMF291*$^{-/-}$ mice (Figures 4H–4J and S4A). Like *NMF291*$^{-/-}$ mice, hemizygous mice from this line developed pronounced ataxia by 12 weeks of age (data not shown). Histological analysis revealed dying granule cells in the cerebellum of 1-month-old transgenic mice, and by 3 months of age, most granule cells had died, similar to the

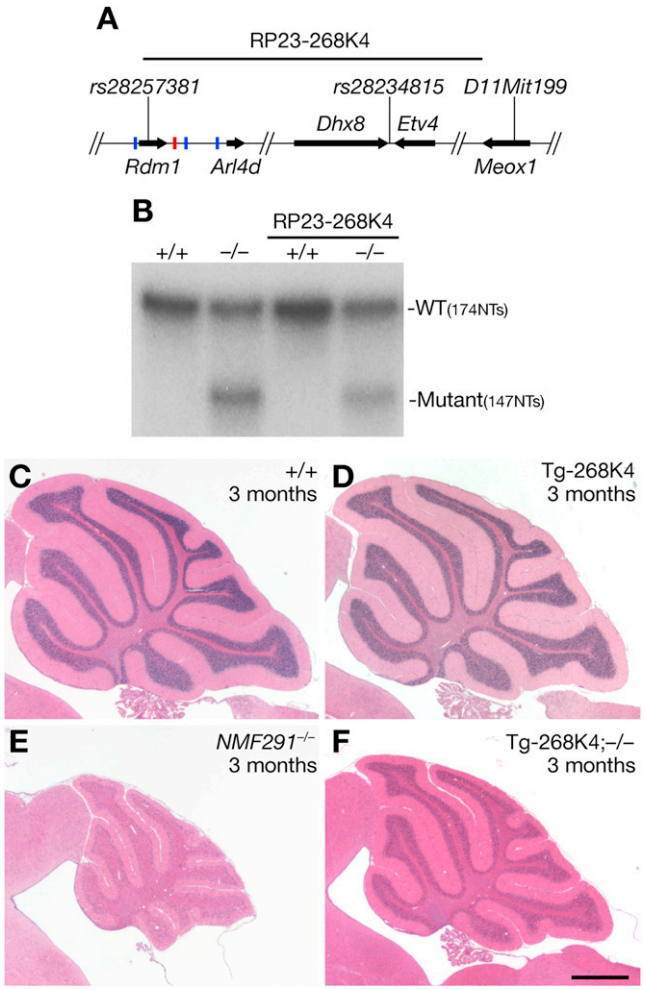

Figure 5. Transgenic Expression of WT U2 snRNAs Partially Rescues the *NMF291*$^{-/-}$ Phenotype

(A) Schematic of the RP23-268K4 BAC, containing three snRNA genes (*Rnu2-8*, red bar; *Rnu2-9* and *-10*, blue bars), used for transgenesis.

(B) RPA of cerebellar RNA from 1-month-old WT (+/+) or *NMF291*$^{-/-}$ (–/–) mice with or without the BAC transgene (RP23-268K4).

(C–F) Hematoxylin and eosin-stained sagittal sections of WT (+/+), RP23-268K4 (Tg-268K4), *NMF291*$^{-/-}$, and Tg-268K4; –/– cerebella.

Scale bar, 500 μm (F). See also Figure S5.

time course of neuron death in *NMF291*$^{-/-}$ mice (Figures 4K and 4L; data not shown). As observed in *NMF291*$^{-/-}$ mice, neuron loss in the dentate gyrus was observed in 3-month-old transgenic mice (Figures S4B and S4C).

If the severity of neurodegeneration is indeed dependent on the ratio of mutant to WT snRNAs, then the complementary experiment in which an increase in expression of WT U2 RNA on the *NMF291*$^{-/-}$ background should lead to attenuation of pathology. To test this hypothesis, we generated a transgenic mouse line carrying a BAC (bacterial artificial chromosome RP23-268K4) containing *Rnu2-8* and two other U2 genes (*Rnu2-9* and *-10*; Figure 5A). This line was crossed to *NMF291* mice to generate *NMF291*$^{-/-}$ mice carrying the BAC transgene. The percentage of mutant/total U2 snRNA was reduced in the cerebellum of Tg-268K4; *NMF291*$^{-/-}$ and Tg-268K4; *NMF291*$^{+/-}$ mice relative to that observed in the cerebellum of age-matched *NMF291*$^{-/-}$ and *NMF291*$^{+/-}$ mice (Figures 5B, S5A, and S5B). Neurodegeneration was also decreased in the cerebellum of 3-month-old Tg-268K4; *NMF291*$^{-/-}$ mice relative to that of age-matched *NMF291*$^{-/-}$ mice (Figures 5C–5F). Surprisingly, when mutant U2 RNAs represented ~17% of total U2 levels, little granule cell loss was observed in aged Tg-268K4; *NMF291*$^{+/-}$ mice (Figures S5C–S5F). When the percentage of mutant/total U2 RNA increased to ~25% as observed in the *NMF291*$^{+/-}$ cerebellum, neurodegeneration was slowly progressive (Figures 4A–4F). However, when this percentage reached ~45% (as in the P30 *NMF291*$^{-/-}$ and Tg-MuU2 cerebellum), rapid granule neuron loss was observed (Figures 1C and 4L). Taken together, our data demonstrate that the expression of the mutant *Rnu2-8* gene is sufficient to induce granule cell death even in the presence of WT U2 expression, and the extent of neuron loss is dependent on the expression level of the mutant U2 snRNAs relative to that of the WT U2 snRNA.

Expression of the Mutant U2 snRNA Decreases Splicing Efficiency

The central role of U2 snRNA in pre-mRNA splicing suggested that abnormalities in this process underlie neurodegeneration in *NMF291*$^{-/-}$ mice. To study the impact of the mutant *Rnu2-8* on pre-mRNA splicing, we employed a previously reported splicing reporter construct, TN24 (ISS+), which encodes both β-galactosidase and luciferase separated by an exon-intron-exon cassette (Kollmus et al., 1996; Nasim et al., 2002). Although β-galactosidase is constitutively expressed from this plasmid, luciferase is only expressed when accurate splicing occurs between the adenovirus 5′ exon and the alternatively spliced SK exon of human *Tpm3* (see diagram in Figure 6C).

HEK293T cells were transfected with ISS+ alone, or cotransfected with the reporter and a 1.5 kb genomic DNA fragment containing the WT or the mutant (Δ5nt) U2 transcription unit (Figures 6A–6C). As controls, cells were cotransfected with the reporter and a plasmid encoding the RNA-binding protein hnRNPG, which has been shown to silence splicing of this exon-intron-exon cassette via binding of the 25 bp intronic-splicing silencer (ISS) (Nasim et al., 2002). Transfection of WT *Rnu2-8* did not have a significant effect on reporter splicing as determined by the ratio of luciferase/β-galactosidase activity or by RT-PCR (Figure 6C). However, transfection of mutant *Rnu2-8* led to a significant decrease (28%; $p < 0.01$) in the splicing efficiency of the reporter compared to that of cells transfected with reporter alone.

Similar experiments were performed using the same reporter lacking the 25 bp ISS (ISS–) (Nasim et al., 2002) (Figure 6D). In agreement with the role of the ISS sequence in splicing silencing, we observed a 4- to 5-fold increase in splicing of this reporter over that of the reporter containing the ISS sequence. As previously shown (Nasim et al., 2002), the inhibitory effect of *hnRNPG* expression on ISS– reporter splicing was greatly reduced (Figure 6D). As observed for the ISS+ reporter, splicing of the ISS– reporter was not changed by expression of the WT U2. However, in contrast to the attenuation of ISS+ reporter splicing

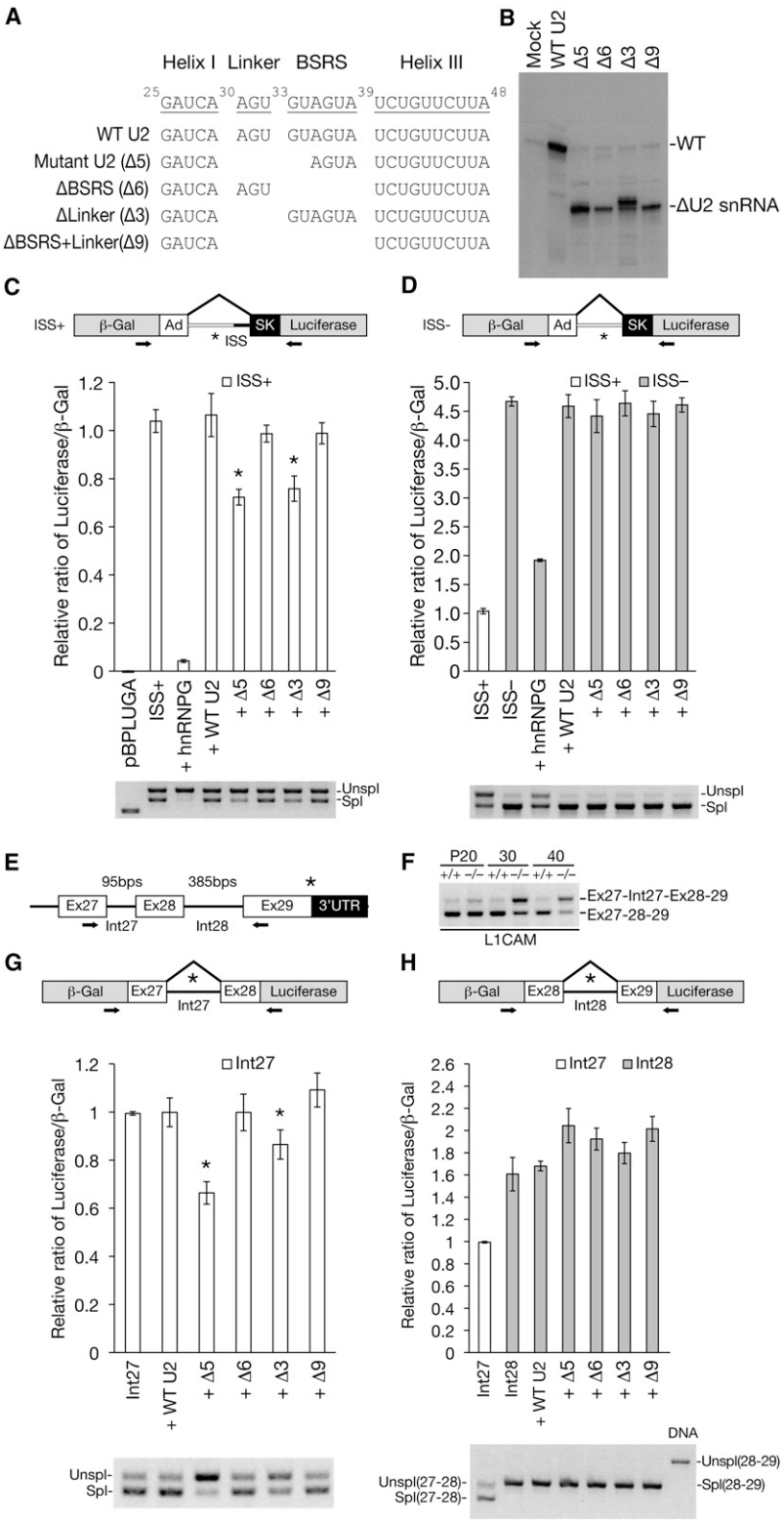

Figure 6. Mutant *Rnu2-8* Selectively Decreases Splicing Efficiency of Introns

(A) The sequences of WT and deletion (Δ) U2 constructs used for cell transfection experiments.

(B) RPA analysis of RNA from mock-transfected HEK293T cells or cells transfected with WT or ΔU2 plasmids.

(C and D) HEK293T cells were transfected with the ISS+ splicing reporter (C) or the ISS− splicing reporter (D), or cotransfected with WT or ΔU2 constructs as indicated. The splicing of pBPLUGA parental vector is shown in (C) as a control, and the splicing of the ISS+ reporter is shown in (D) as a reference. The splicing efficiency of the reporters was measured by luciferase/β-Gal (β-galactosidase) activity (top panels in C and D) and confirmed by RT-PCR (bottom panels). Values represent mean ± SEM, n = 3; *p < 0.01; one-way ANOVA. Asterisk (*) and arrows in reporter diagrams denote stop codons and RT-PCR primers, respectively.

(E) A diagram of the 3′ region of the *L1CAM* gene. Asterisk (*) denotes stop codon. Arrows indicate RT-PCR primers.

(F) RT-PCR was performed on WT (+/+) and *NMF291*$^{-/-}$ (−/−) cerebellar cDNA at indicated ages.

(G and H) HEK293T cells were transfected with *L1CAM* exon 27-intron 27-exon 28 (G) and exon 28-intron 28-exon 29 (H) splicing reporters with or without WT or ΔU2 constructs as indicated. Splicing of these reporters was analyzed as described above in (C) and (D). As references, the spliced RT-PCR products of exon 27-intron 27-exon 28 reporter and the unspliced PCR product amplified from the exon 28-intron 28-exon 29 reporter plasmid (DNA) are also shown in (H). Values represent mean ± SEM, n = 3; *p < 0.01; one-way ANOVA. Asterisks (*) in reporter diagrams denote stop codons.

by expression of the mutant U2 construct, expression of the mutant U2 did not significantly affect splicing of the ISS− reporter. These results suggest that alterations in splicing efficiency mediated by the expression of the mutant U2 snRNA may be dependent on the presence of splicing regulatory sequences.

The presence of intronic or exonic splicing regulatory sequences often accompanies alternative splicing of pre-mRNA (Black, 2003); thus, we initially analyzed several alternative-splicing events that were previously reported to occur in the human cerebellum (Wang et al., 2008). Of the 20 alternative splicing events, including 1 in the neural cell adhesion molecule L1 (*L1CAM*), 4 displayed obvious changes in relative isoform expression between the WT and *NMF291*$^{-/-}$ cerebellum (data not shown). PCR amplification of the distal exons of the *L1CAM* transcript from WT cerebellar RNA generated two isoforms: the major form containing exons 27-28-29, and a minor isoform that retains the 95 bp intron located between exons 27 and 28 (Figures 6E and 6F). Coincident with the decrease of the fully spliced isoform, the abundance of the intron 27-containing isoform was increased in mutant cerebellar RNA. Interestingly, these alterations in splicing were most dramatic in the P30 and P40 cerebellum, demonstrating that the change in the ratio of splicing variants was temporally regulated in a manner coincident with expression of the mutant U2 snRNA.

To directly evaluate the effects of the mutant U2 on splicing of intron 27, we generated *L1CAM* splicing reporters. A cassette containing exon 27, the alternatively spliced intron 27, and exon 28, or a cassette with exon 28, the constitutively spliced intron 28, and exon 29 were cloned into the pBPLUGA plasmid (Figures 6G and 6H). These plasmids were cotransfected into HEK293T cells with the WT or mutant *Rnu2-8* plasmid. Transfection of the intron 27-containing reporter resulted in both spliced and unspliced transcripts as evidenced by RT-PCR (Figure 6G). In contrast only spliced transcripts were observed in cells transfected with the intron 28-containing reporter, and luciferase/β-galactosidase activity was increased accordingly (Figure 6H). Overexpression of the WT U2 had no effect on splicing of either reporter. However, in agreement with our in vivo data, expression of mutant *Rnu2-8* caused a decrease in splicing efficiency (34%; $p < 0.01$) of intron 27, but not of intron 28, the splicing efficiency of which was increased for unknown reasons (Figures 6G and 6H). These reporter data confirm that expression of the mutant U2 disrupts splicing of select introns.

Deletion of the U2/U6 Helix IA Linker Is Sufficient to Disrupt Splicing

The 5 nt deletion in *Rnu2-8* removes 2 nt of the BSRS, which recognizes and forms a duplex with the intronic branch site (BS) of the pre-mRNA that is important for the spliceosome assembly and the first catalytic step of splicing (Wahl et al., 2009). In addition, the *NMF291* deletion removes the 3 nt linker between the BSRS and the sequence that forms the U2/U6 helix IA. The distance between these two sequences has been shown to change splicing kinetics in yeast (McGrail et al., 2006; Ryan and Abelson, 2002; Smith et al., 2009). To further understand the underlying mechanism of mutant *Rnu2-8*-induced splicing defects, we created a series of U2 deletion plasmids: Δ6, in which the entire BSRS was deleted; Δ3, in which the linker sequence between BSRS and U2/U6 helix IA was deleted; and Δ9, in which both the entire BSRS and the linker were deleted (Figure 6A).

Experiments in yeast demonstrated that mutations in U2 snRNA, which disrupt the duplex formation between the BSRS and the BS, inhibit spliceosome assembly and result in the degradation of these RNAs (Smith et al., 2009). In agreement with these studies, we consistently observed lower expression levels of Δ6 and Δ9 *Rnu2-8* RNAs, both of which lack the BSRS, compared to that observed for the WT, Δ5 (the *NMF291* mutant form), and Δ3 *Rnu2-8* RNAs in transfected cells (Figure 6B). Cotransfection of the Δ6 or the Δ9 plasmid with the ISS+ reporter did not affect reporter splicing (Figure 6C). However, expression of the Δ3 construct significantly decreased (24%; $p < 0.01$) splicing of the ISS+ reporter, closely mimicking the repression of splicing that was observed when Δ5 *Rnu2-8* was cotransfected with the reporter. Also as observed with cotransfection of Δ5 *Rnu2-8*, expression of Δ3 construct had no effect on splicing of ISS− splicing reporter (Figure 6D).

Similarly, expression of the Δ3 *Rnu2-8* plasmid was sufficient to reduce splicing (13%; $p < 0.01$) of intron 27 from the *L1CAM* intron 27-containing splicing reporter, although not as efficiently as cotransfection of the reporter with Δ5 *Rnu2-8*, suggesting that the deletion of 2 nt of the BSRS may also contribute to the Δ5 effect on splicing (Figure 6G). Cotransfection of the Δ3 plasmid with the intron 28-containing reporter again led to an increase rather than decrease of splicing, as did expression of the Δ6 and Δ9 plasmids (Figure 6H). Our data suggest that expression of a U2 snRNA with either the *NMF291*-associated 5 nt deletion or lacking the linker sequence between the BSRS and the U2/U6 helix IA disrupts select intron splicing.

Abnormal Alternative Splicing in the *NMF291* Mutant Cerebellum

To analyze alternative splicing in the *NMF291* mutant cerebellum, exon expression was examined by Affymetrix mouse exon 1.0 ST microarrays. Microarrays were hybridized with RNA from three WT and three *NMF291*$^{-/-}$ cerebella isolated at P30, a time when the mutant U2 RNA is expressed at peak levels, but few neurons have degenerated (Figures S1A–S1D, 3E, and S3E). A total of 123 genes were differentially expressed between the WT and mutant cerebellum, as demonstrated by analysis of signal across all probe clusters for a gene (fold change ≥ 1.5; $p < 0.05$) (Table S1A). Differential expression of most (78%) of these genes was relatively low (1.5- to 2-fold), suggesting that overall gene expression was not dramatically altered in the P30 mutant cerebellum.

Paired analysis of the exon splicing index (SI), which was calculated by normalizing exon expression to gene level expression (Clark et al., 2007; de la Grange et al., 2010), revealed that the expression of 206 exons in 178 genes was differentially expressed between the WT and mutant cerebellum (SI fold change ≥ 1.5; $p < 0.05$) (Table S1B). These exons were compared to the comprehensive list of known human and mouse splice variants in the FAST DB database (de la Grange et al., 2007), and 146 (71%) events, representing all major types of alternative splicing patterns, were previously annotated as alternatively spliced

(Table S1B; Figure 7A). To validate our exon array results, RT-PCR was performed using cerebellar cDNA from four independent mice of each genotype. Of these events, 92% (12 of 13) were validated as differentially spliced between the WT and mutant cerebellum (Figure S6A; data not shown).

Interestingly, 14% of the differentially spliced events detected by exon array analysis were annotated as alternatively spliced introns, although introns normally represent a very minor (1%–3%) class of alternative splicing events (Chacko and Ranganathan, 2009; de la Grange et al., 2010; Wang et al., 2008). To examine this more closely and to expand our exon array results, we performed RNA-Seq analysis. Libraries were prepared from cerebellar mRNA from three P30 mutant and two P30 WT mice and sequenced. The resulting reads were aligned to the mouse genome reference sequence via SpliceMap (http://www.stanford.edu/group/wonglab/SpliceMap/), an algorithm that maps exon-exon junctions without relying on previous exon annotations for recovering the splicing junctions (Au et al., 2010). A total of $53.48 \pm 6.35 \times 10^6$ reads per sample were uniquely mapped to the mouse genome, and 61.23% ± 1.18%, 20.80% ± 1.54%, and 6.20% ± 0.19% of these reads uniquely mapped to exons, introns, and splice junctions, respectively (Table S1C).

To identify alternative splicing pattern changes between the WT and *NMF291*$^{-/-}$ cerebellum, splicing junction reads were extracted and normalized for isoform expression to generate the Relative Junction Index (RJI) (Figure S6). Comparison of the RJI between the two genotypes identified 1,636 junctions that were differentially expressed (RJI ratio ≥ 2.0; $p < 0.05$; Table S1D). In addition, 52 and 1,137 junction reads that were present only in the WT and mutant data sets, respectively, indicated that many splicing variants in the mutant cerebellum were not present, or present at a very low levels, in the WT cerebellum (Table S1E). As described above, RT-PCR using WT and mutant cerebellar cDNA was performed to test differential splicing of junctions. A total of 20 of 20 junctions that were originally identified in both genotypes and 20 of 21 (95%) of the junctions identified only in 1 genotype were validated (Figures S6B and S6C; data not shown).

To examine global abnormalities in splicing of introns in the mutant cerebellum, we calculated the Relative Intron retention Index (RII) from our WT and mutant RNA-Seq data sets (Figure S6). Comparison of WT and mutant RIIs indicated that 3,978 introns were retained at higher levels in the mutant cerebellum (RII ratio ≥ 2; $p < 0.05$, Figure 7B; Table S1F), including intron 27 of *L1CAM* (RII ratio = 3.55; $p = 0.0012$). In contrast, we identified only 362 introns that were retained at higher levels in the WT cerebellum (RII ratio ≥ 2; $p < 0.05$). To check the validity of our analysis, we performed RT-PCR on 23 introns that were present at higher levels in the mutant transcriptome by RNA-Seq, and all were validated (Figures S6D and S6E; data not shown). Furthermore, 19 of 23 (82.61%) of these introns, like intron 27 of *LICAM*, and 5 of 7 RT-PCR-validated introns identified by exon array, were also present in WT cerebellum as a minor isoform (Figures S6A and S6D). These results indicate that these introns represent alternative splicing events and are likely to be suboptimal pre-mRNA substrates even in presence of the WT spliceosome. Previous studies have shown that small introns are prone to being retained in human and mouse transcripts in physiological conditions (Sakabe and de Souza, 2007). These prompted us to check the size distribution of the intron retention events identified by RNA-Seq. Indeed, 30.62% of the retained introns in the mutant cerebellum were less than 100 bp, which largely differs from the size distribution of introns in the mouse genome (RefSeq; 5.31% < 100 bp) or those significantly retained in the WT cerebellum (3.31% < 100 bp) (Figure 7C). As expected, differences in splicing of small introns removed by the U12-dependent minor spliceosome were not observed in the mutant cerebellum (Figure S6F). Thus, both exon array and RNA-Seq analysis demonstrated that a group of alternative splicing events, including the splicing of small introns, was altered in the *NMF291*$^{-/-}$ cerebellum.

To check the overlap of our exon array and RNA-Seq analysis, we compared intron retention events (Table S1H). Of these events, 96.4% (27 of 28) detected by exon array displayed differences in the same direction in RNA-Seq data, although only 46.4% (13 of 28) passed our stringent threshold set for RNA-Seq analysis. Although differential events in other splicing event categories ascertained by both analyses were clearly validated by RT-PCR, little overlap was observed in the data sets, likely due to the different experimental and analysis parameters used in the two methods (see Extended Experimental Procedures).

The role of U2 snRNA as a basal component of the spliceosome would predict that splicing of transcripts encoding proteins across many functional classes would be disrupted in the mutant cerebellum. Indeed, splicing alterations between the WT and mutant cerebellum occur in genes with many predicted cellular roles (Tables S1B and S1D–S1F). However, Gene Ontology (GO) analysis of the differentially expressed junctions and spliced introns detected by RNA-Seq and exon array analysis revealed that genes annotated to GO terms of nucleoplasm (GO:0005654) were significantly enriched, as were those annotated to ribonucleotide binding (GO:0032553) (Table S1G). Interestingly, after these two functional clusters, the most significantly enriched genes in the differentially spliced intron data set were annotated to mRNA processing (GO:0006397), including those annotated to the spliceosomal complex (GO:0005681) (Figure 7D; Table S1G). Differentially expressed exons and genes also showed significant enrichment for mRNA processing, although at higher p values.

DISCUSSION

We demonstrate that a mutation in one of the multicopy mouse U2 snRNA genes causes defects in pre-mRNA splicing, leading to neurodegeneration. U2 snRNAs play an essential role in formation of the catalytically active spliceosome by base pairing with both the intron branch point and the U6 snRNA (Wahl et al., 2009). Expression of the mutant U2 snRNA alters pre-mRNA splicing at selective splice sites that are often associated with alternative splicing, demonstrating that U-snRNA dysfunction, like downregulation of core spliceosomal proteins, can influence splice site choice (Corioni et al., 2011; Park et al., 2004; Saltzman et al., 2011; Shaw et al., 2007).

One of the main pathological features of the *NMF291*$^{-/-}$ cerebellum is the increased retention of small introns, which likely

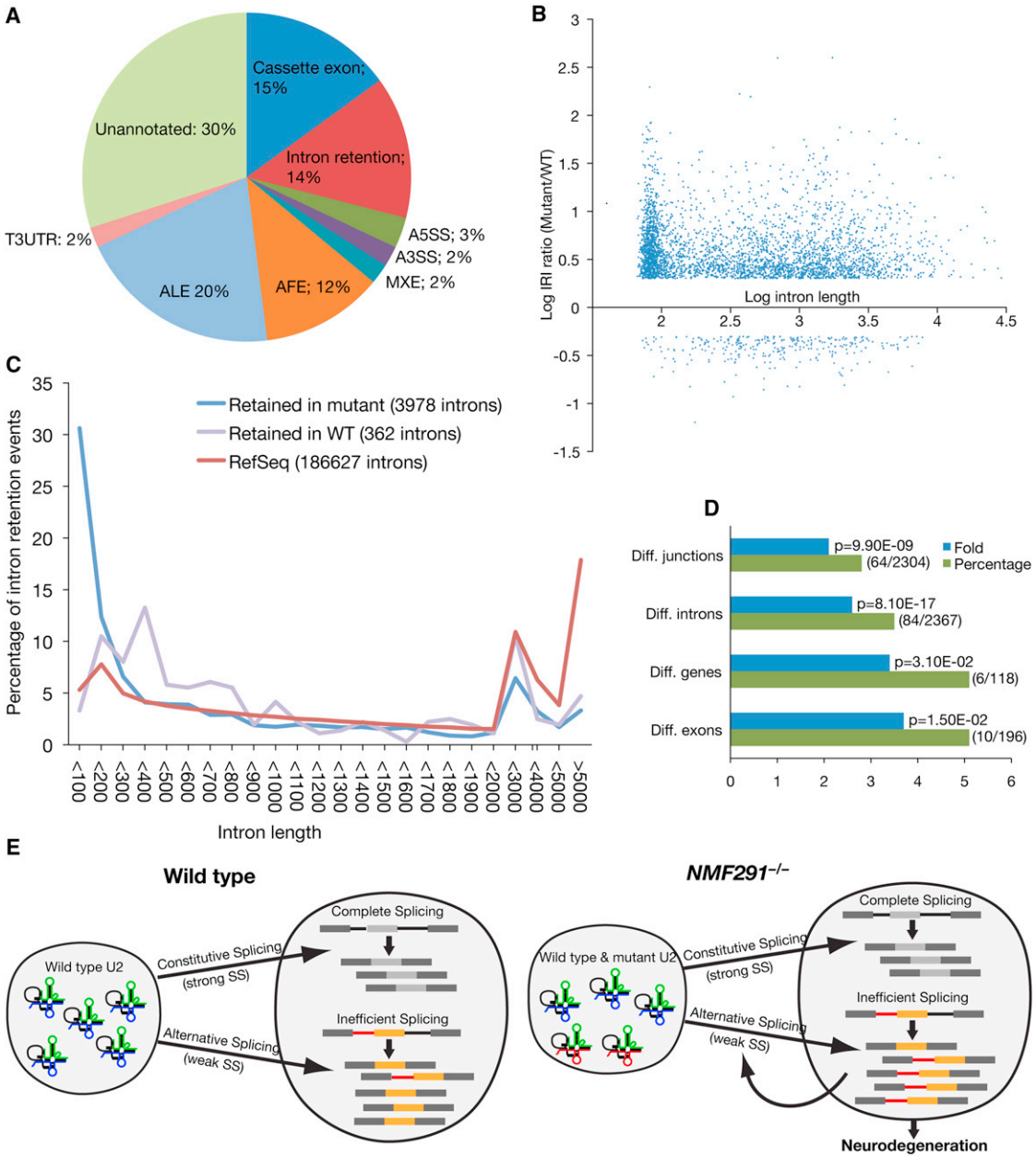

Figure 7. Global Splicing Abnormalities in the *NMF291*$^{-/-}$ Cerebellum

(A) Types of alternative splicing events identified by exon array analysis as differentially spliced between the WT and the *NMF291*$^{-/-}$ cerebellum. A3SS, alternative 3′ splice site; A5SS, alternative 5′ splice site; AFE, alternative first exon; ALE, alternative last exon; MXE, mutually exclusive exon; T3UTR, truncated 3′UTR.

(B) The log of the mutant/WT IRI generated by RNA-Seq analysis plotted against the log of the intron length (bp).

(C) Significantly retained introns in the cerebellum of *NMF291*$^{-/-}$ or WT mice, or RefSeq introns were grouped by length and plotted as a percentage of the total introns.

(D) GO analysis of genes annotated to the pre-mRNA splicing GO term were significantly enriched in the differentially spliced exons (Diff. junctions) and introns (Diff. introns) identified by RNA-Seq, and differentially spliced exons (Diff. exons) and differentially expressed genes (Diff. genes) identified by exon array. Percentage is the number of genes (the numerator in parentheses) annotated to the GO term divided by the total number of inputted genes (the denominator in parentheses). Fold enrichment is the magnitude of enrichment of input genes relative to all mouse genes annotated to pre-mRNA splicing. The p value indicates the significance of gene-term enrichment with a modified Fisher's exact test.

(E) The working model for our findings. The splicing status and biological consequences of expression of WT (blue) and *NMF291* mutant (red) U2 snRNAs in WT and *NMF291*$^{-/-}$ neurons are shown. Our in vivo and in vitro data suggest that expression of mutant U2 snRNA disrupts splicing at many suboptimal or weaker splice sites, including some of those used in alternative splicing. These changes in alternative splicing may be further amplified by altered splicing of RNA-processing factors caused directly by mutant U2 snRNAs or by autoregulation.

See also Figure S6 and Tables S1A–S1H.

represent unique spliceosomal substrates. Unlike splicing of large introns, which is thought to first occur by pairing of splice sites across the exon ("exon definition"), splicing of short introns likely occurs by pairing of 5′ and 3′ splice sites across the intron ("intron definition") (Berget, 1995). Furthermore, even under normal physiological conditions, many of the highly retained introns in the mutant cerebellum are not fully spliced, consistent with the observation that weak splicing sites often flank small introns (Lim and Burge, 2001; Sakabe and de Souza, 2007). Given the disruption of short intron splicing and other alternative splicing events, it is plausible that mutant U2 snRNPs are fully functional on optimal, but not suboptimal, substrates (Figure 7E).

Interestingly, we found that mRNA-processing genes were significantly enriched among the alternative splicing events differentially expressed between the WT and mutant cerebellum, suggesting that neurons may utilize alternative splicing to regulate the function of proteins involved in RNA splicing and processing in an effort to restore splicing homeostasis. Indeed, studies have shown that a number of splicing regulators autoregulate their expression and activity via transcriptional feedback loops and alternative splicing (Ni et al., 2007; Saltzman et al., 2011; Wollerton et al., 2004). However, rather than reestablishing homeostasis, these splicing alterations could in fact act to amplify the amount of abnormal splicing and ultimately prove deleterious. It will be intriguing to see whether the expression level and/or alternative splicing status of these mRNA-processing genes is also affected in SMA patients or ALS/FTD patients with mutations in *TDP-43* or *FUS/TLS*.

The ultimate cause of neuron death in the mutant cerebellum is unclear. Cell death could be caused by the generation of proteins with altered function or by the production of RNAs containing abnormal sequences, which could themselves be toxic as previously reported for trinucleotide repeat expansion diseases (Li et al., 2008). Retained introns may also contribute to neuron death by sequestering splicing regulators and/or other RNA binding proteins. In addition, many of these introns likely harbor premature translation termination codons (PTCs) that would be predicted to trigger the nonsense-mediated mRNA-decay (NMD) pathway. In addition to its role in degradation of abnormal transcripts, NMD also regulates many natural PTC-containing transcripts, including those involved in synaptic physiology and cellular stress (Gardner, 2010; Giorgi et al., 2007). Enhanced and/or prolonged NMD activation could overwhelm the NMD pathway, causing dysregulation of natural NMD targets that might be essential for cell survival, or itself cause cellular stress.

Finally, our data demonstrate the potential for disease-causing mutations in multicopy genes. Although a single U2 gene is present in yeast, multiple copies of these genes exist in higher organisms, each producing identical or nearly identical products. Indeed, the region on human Chromosome 17p21 (homologous to the *Rnu2-6* to *Rnu2-10*-containing region on mouse Chromosome 11) also contains a cluster of stably inherited U2 genes that vary in copy number from 5 to 25 (Van Arsdell and Weiner, 1984; Westin et al., 1984). In addition to our findings of temporal and spatial regulation of a mouse U2 gene, developmental regulation of other snRNA genes, including U2 snRNA genes, has been reported (Forbes et al., 1984; Lund et al., 1985; Sierra-Montes et al., 2005; Stefanovic et al., 1991). Furthermore, the developmental arrest associated with homozygosity for a mutation in 1 of 12 *C. elegans* U1 genes raises the possibility of differences in expression and/or function between *C. elegans* U1 genes (Zahler et al., 2004). Whether individual human U2s (or other multicopy genes) are differentially expressed during development, in different cell types, or even as a result of pathogenic processes is unknown. However, the potential for discrete regulation of individual members of multigene families, combined with their potential for copy number variation, increases the prospect of uncovering disease-causing mutations in repetitive genes.

EXPERIMENTAL PROCEDURES

Mice

The *NMF291* mutant strain was derived from EMS-treated ES cells and a two-generation mating scheme, as described previously (Munroe and Schimenti, 2009). Genetic mapping of the *NMF291* mutation was performed using an intersubspecific intercross (B6; 129 *NMF291* × CAST/Ei). The Jackson Laboratory Animal Care and Use Committee approved all animal protocols.

Histology Analysis

Hematoxylin and eosin staining was performed on Bouin's fixed tissue. Cleaved Caspase-3 (Cell Signaling) immunostaining and TUNEL assays (Roche) were performed as described previously (Zhao et al., 2005). At least three mice of each genotype were used for all histological analyses.

RPA, Northern Blot Assay, and RT-PCR Assay

Total RNA was extracted by TRIzol (Invitrogen) and treated with DNase I (Ambion). RPA analysis was performed as suggested by the manufacturer's instructions (Ambion). For northern blots, total RNA was separated by 10% denaturing polyacrylamide gel, and the membrane was hybridized with end-labeled DNA oligo probes. RT-PCR was performed on random-primed cDNA (Invitrogen). Primers used for RT-PCR are described in Table S2. Density of bands in scanned X-ray films was determined by ImageQuant 5.2 software (Amersham).

Constructs, Cell Culture, Transfection, and Luciferase Assays

The mutant *Rnu2-8* DNA fragment used for generating transgenic mice and the corresponding WT DNA fragment were cloned into pCR2.1-TOPO for expression of WT and mutant U2 snRNA in cultured cells. The Δ3, Δ6, and Δ9 U2 snRNA and ISS− expression constructs were generated by site-directed mutagenesis (Stratagene). Primers used for construct generation are described in Table S2B. HEK293T cells were used for transient transfection (Lipofectamine 2000; Invitrogen). Luciferase and β-galactosidase activities (Promega) were measured in a multilabel counter 48 hr after transfection. Statistical significance was determined by ANOVA analysis (SPSS).

Exon Array, RNA-Seq, and Functional GO Analysis

Data treatment of Mouse Exon 1.0 ST Arrays (Affymetrix) was done by the EASANA analysis and the interface visualization system (GenoSplice Technology, http://www.genosplice.com), which is based on the FAST DB annotations (de la Grange et al., 2007). Probe selection and statistical analysis were preformed as previously described (Clark et al., 2007; de la Grange et al., 2010). The GEO (Gene Expression Omnibus) accession number for our exon array data is GSE33069. For RNA-Seq, mRNA purification and DNA library preparation were performed according to the manufacturer's protocol (Illumina). The library was sequenced on Illumina GAIIX using paired-end read strategy. For de novo identification of junctions, the reads were inputted to SpliceMap 3.3.6 (Au et al., 2010) and aligned to the mouse reference genome. A workflow chart of our RNA-Seq analysis is shown in Figure S6G. RefSeq intron length information was extracted from UCSC. The GO analysis was conducted by using DAVID bioinformatics resources 6.7 (Huang da et al., 2009). Primers

used for exon array and RNA-Seq validation experiments are described in Table S2C.

ACCESSION NUMBERS

Our exon array data have been deposited into the GEO. The GEO accession number is GSE33069. The databank accession numbers for the *Rnu2-6*, *Rnu2-7*, *Rnu2-8*, *Rnu2-9*, and *Rnu2-10* sequences reported in this paper are JN863957, JN863958, JN863956, JN863959, and JN863960, respectively.

SUPPLEMENTAL INFORMATION

Supplemental Information includes Extended Experimental Procedures, six figures, two tables, and one movie and can be found with this article online at doi:10.1016/j.cell.2011.11.057.

ACKNOWLEDGMENTS

We thank The Jackson Laboratory sequencing, gene expression, histology, microinjection, and multimedia services for their assistance. We also thank W.H. Wong for discussions on RNA-Seq analysis, J. Blake and C. Bult for discussion on GO analysis, L. Beverly-Staggs and J. Cook for mouse husbandry assistance, P. de la Grange for exon array analysis, J. Hammer and L. Zhao for graphics assistance, J. McCarthy and M. Nasim for plasmids, and R. Burgess, G. Cox, and M. Hibbs for comments on the manuscript. This work was partially supported by an institutional National Cancer Institute core grant (JAX), and the work of J.C.M. was partially supported by NIH Grants R01HG004634 and R01HG005717. S.L.A. is an investigator of the Howard Hughes Medical Institute.

Received: April 26, 2011
Revised: August 6, 2011
Accepted: November 8, 2011
Published: January 19, 2012

REFERENCES

Au, K.F., Jiang, H., Lin, L., Xing, Y., and Wong, W.H. (2010). Detection of splice junctions from paired-end RNA-seq data by SpliceMap. Nucleic Acids Res. *38*, 4570–4578.

Berget, S.M. (1995). Exon recognition in vertebrate splicing. J. Biol. Chem. *270*, 2411–2414.

Black, D.L. (2003). Mechanisms of alternative pre-messenger RNA splicing. Annu. Rev. Biochem. *72*, 291–336.

Bult, C., Kibbe, W.A., Snoddy, J., Vitaterna, M., Swanson, D., Pretel, S., Li, Y., Hohman, M.M., Rinchik, E., Takahashi, J.S., et al. (2004). A genome end-game: understanding gene function in the nervous system. Nat. Neurosci. *7*, 484–485.

Chacko, E., and Ranganathan, S. (2009). Comprehensive splicing graph analysis of alternative splicing patterns in chicken, compared to human and mouse. BMC Genomics *10* (*Suppl 1*), S5.

Clark, T.A., Schweitzer, A.C., Chen, T.X., Staples, M.K., Lu, G., Wang, H., Williams, A., and Blume, J.E. (2007). Discovery of tissue-specific exons using comprehensive human exon microarrays. Genome Biol. *8*, R64.

Cooper, T.A., Wan, L., and Dreyfuss, G. (2009). RNA and disease. Cell *136*, 777–793.

Corioni, M., Antih, N., Tanackovic, G., Zavolan, M., and Krämer, A. (2011). Analysis of in situ pre-mRNA targets of human splicing factor SF1 reveals a function in alternative splicing. Nucleic Acids Res. *39*, 1868–1879.

de la Grange, P., Dutertre, M., Correa, M., and Auboeuf, D. (2007). A new advance in alternative splicing databases: from catalogue to detailed analysis of regulation of expression and function of human alternative splicing variants. BMC Bioinformatics *8*, 180.

de la Grange, P., Gratadou, L., Delord, M., Dutertre, M., and Auboeuf, D. (2010). Splicing factor and exon profiling across human tissues. Nucleic Acids Res. *38*, 2825–2838.

Edery, P., Marcaillou, C., Sahbatou, M., Labalme, A., Chastang, J., Touraine, R., Tubacher, E., Senni, F., Bober, M.B., Nampoothiri, S., et al. (2011). Association of TALS developmental disorder with defect in minor splicing component U4atac snRNA. Science *332*, 240–243.

Egloff, S., O'Reilly, D., and Murphy, S. (2008). Expression of human snRNA genes from beginning to end. Biochem. Soc. Trans. *36*, 590–594.

Forbes, D.J., Kirschner, M.W., Caput, D., Dahlberg, J.E., and Lund, E. (1984). Differential expression of multiple U1 small nuclear RNAs in oocytes and embryos of Xenopus laevis. Cell *38*, 681–689.

Gardner, L.B. (2010). Nonsense-mediated RNA decay regulation by cellular stress: implications for tumorigenesis. Mol. Cancer Res. *8*, 295–308.

Giorgi, C., Yeo, G.W., Stone, M.E., Katz, D.B., Burge, C., Turrigiano, G., and Moore, M.J. (2007). The EJC factor eIF4AIII modulates synaptic strength and neuronal protein expression. Cell *130*, 179–191.

He, H., Liyanarachchi, S., Akagi, K., Nagy, R., Li, J., Dietrich, R.C., Li, W., Sebastian, N., Wen, B., Xin, B., et al. (2011). Mutations in U4atac snRNA, a component of the minor spliceosome, in the developmental disorder MOPD I. Science *332*, 238–240.

Hernandez, N. (2001). Small nuclear RNA genes: a model system to study fundamental mechanisms of transcription. J. Biol. Chem. *276*, 26733–26736.

Huang da, W., Sherman, B.T., and Lempicki, R.A. (2009). Systematic and integrative analysis of large gene lists using DAVID bioinformatics resources. Nat. Protoc. *4*, 44–57.

Kollmus, H., Flohé, L., and McCarthy, J.E. (1996). Analysis of eukaryotic mRNA structures directing cotranslational incorporation of selenocysteine. Nucleic Acids Res. *24*, 1195–1201.

Lagier-Tourenne, C., Polymenidou, M., and Cleveland, D.W. (2010). TDP-43 and FUS/TLS: emerging roles in RNA processing and neurodegeneration. Hum. Mol. Genet. *19*(R1), R46–R64.

Lefebvre, S., Bürglen, L., Reboullet, S., Clermont, O., Burlet, P., Viollet, L., Benichou, B., Cruaud, C., Millasseau, P., Zeviani, M., et al. (1995). Identification and characterization of a spinal muscular atrophy-determining gene. Cell *80*, 155–165.

Lemmens, R., Moore, M.J., Al-Chalabi, A., Brown, R.H., Jr., and Robberecht, W. (2010). RNA metabolism and the pathogenesis of motor neuron diseases. Trends Neurosci. *33*, 249–258.

Lerner, E.A., Lerner, M.R., Janeway, C.A., Jr., and Steitz, J.A. (1981). Monoclonal antibodies to nucleic acid-containing cellular constituents: probes for molecular biology and autoimmune disease. Proc. Natl. Acad. Sci. USA *78*, 2737–2741.

Li, L.B., Yu, Z., Teng, X., and Bonini, N.M. (2008). RNA toxicity is a component of ataxin-3 degeneration in Drosophila. Nature *453*, 1107–1111.

Licatalosi, D.D., and Darnell, R.B. (2006). Splicing regulation in neurologic disease. Neuron *52*, 93–101.

Lim, L.P., and Burge, C.B. (2001). A computational analysis of sequence features involved in recognition of short introns. Proc. Natl. Acad. Sci. USA *98*, 11193–11198.

Lund, E., Kahan, B., and Dahlberg, J.E. (1985). Differential control of U1 small nuclear RNA expression during mouse development. Science *229*, 1271–1274.

Manser, T., and Gesteland, R.F. (1982). Human U1 loci: genes for human U1 RNA have dramatically similar genomic environments. Cell *29*, 257–264.

Marz, M., Kirsten, T., and Stadler, P.F. (2008). Evolution of spliceosomal snRNA genes in metazoan animals. J. Mol. Evol. *67*, 594–607.

McGrail, J.C., Tatum, E.M., and O'Keefe, R.T. (2006). Mutation in the U2 snRNA influences exon interactions of U5 snRNA loop 1 during pre-mRNA splicing. EMBO J. *25*, 3813–3822.

Mordes, D., Luo, X., Kar, A., Kuo, D., Xu, L., Fushimi, K., Yu, G., Sternberg, P., Jr., and Wu, J.Y. (2006). Pre-mRNA splicing and retinitis pigmentosa. Mol. Vis. *12*, 1259–1271.

Munroe, R., and Schimenti, J. (2009). Mutagenesis of mouse embryonic stem cells with ethylmethanesulfonate. Methods Mol. Biol. *530*, 131–138.

Nasim, M.T., Chowdhury, H.M., and Eperon, I.C. (2002). A double reporter assay for detecting changes in the ratio of spliced and unspliced mRNA in mammalian cells. Nucleic Acids Res. *30*, e109.

Ni, J.Z., Grate, L., Donohue, J.P., Preston, C., Nobida, N., O'Brien, G., Shiue, L., Clark, T.A., Blume, J.E., and Ares, M., Jr. (2007). Ultraconserved elements are associated with homeostatic control of splicing regulators by alternative splicing and nonsense-mediated decay. Genes Dev. *21*, 708–718.

Park, J.W., Parisky, K., Celotto, A.M., Reenan, R.A., and Graveley, B.R. (2004). Identification of alternative splicing regulators by RNA interference in Drosophila. Proc. Natl. Acad. Sci. USA *101*, 15974–15979.

Pavelitz, T., Rusché, L., Matera, A.G., Scharf, J.M., and Weiner, A.M. (1995). Concerted evolution of the tandem array encoding primate U2 snRNA occurs in situ, without changing the cytological context of the RNU2 locus. EMBO J. *14*, 169–177.

Polymenidou, M., Lagier-Tourenne, C., Hutt, K.R., Huelga, S.C., Moran, J., Liang, T.Y., Ling, S.C., Sun, E., Wancewicz, E., Mazur, C., et al. (2011). Long pre-mRNA depletion and RNA missplicing contribute to neuronal vulnerability from loss of TDP-43. Nat. Neurosci. *14*, 459–468.

Ryan, D.E., and Abelson, J. (2002). The conserved central domain of yeast U6 snRNA: importance of U2-U6 helix Ia in spliceosome assembly. RNA *8*, 997–1010.

Sakabe, N.J., and de Souza, S.J. (2007). Sequence features responsible for intron retention in human. BMC Genomics *8*, 59.

Saltzman, A.L., Pan, Q., and Blencowe, B.J. (2011). Regulation of alternative splicing by the core spliceosomal machinery. Genes Dev. *25*, 373–384.

Sauterer, R.A., Feeney, R.J., and Zieve, G.W. (1988). Cytoplasmic assembly of snRNP particles from stored proteins and newly transcribed snRNA's in L929 mouse fibroblasts. Exp. Cell Res. *176*, 344–359.

Shaw, S.D., Chakrabarti, S., Ghosh, G., and Krainer, A.R. (2007). Deletion of the N-terminus of SF2/ASF permits RS-domain-independent pre-mRNA splicing. PLoS One *2*, e854.

Sierra-Montes, J.M., Pereira-Simon, S., Smail, S.S., and Herrera, R.J. (2005). The silk moth Bombyx mori U1 and U2 snRNA variants are differentially expressed. Gene *352*, 127–136.

Smith, D.J., Konarska, M.M., and Query, C.C. (2009). Insights into branch nucleophile positioning and activation from an orthogonal pre-mRNA splicing system in yeast. Mol. Cell *34*, 333–343.

Stefanovic, B., Li, J.M., Sakallah, S., and Marzluff, W.F. (1991). Isolation and characterization of developmentally regulated sea urchin U2 snRNA genes. Dev. Biol. *148*, 284–294.

Tollervey, J.R., Curk, T., Rogelj, B., Briese, M., Cereda, M., Kayikci, M., König, J., Hortobágyi, T., Nishimura, A.L., Zupunski, V., et al. (2011). Characterizing the RNA targets and position-dependent splicing regulation by TDP-43. Nat. Neurosci. *14*, 452–458.

Van Arsdell, S.W., and Weiner, A.M. (1984). Human genes for U2 small nuclear RNA are tandemly repeated. Mol. Cell. Biol. *4*, 492–499.

Wahl, M.C., Will, C.L., and Lührmann, R. (2009). The spliceosome: design principles of a dynamic RNP machine. Cell *136*, 701–718.

Wang, E.T., Sandberg, R., Luo, S., Khrebtukova, I., Zhang, L., Mayr, C., Kingsmore, S.F., Schroth, G.P., and Burge, C.B. (2008). Alternative isoform regulation in human tissue transcriptomes. Nature *456*, 470–476.

Westin, G., Zabielski, J., Hammarström, K., Monstein, H.J., Bark, C., and Pettersson, U. (1984). Clustered genes for human U2 RNA. Proc. Natl. Acad. Sci. USA *81*, 3811–3815.

Wollerton, M.C., Gooding, C., Wagner, E.J., Garcia-Blanco, M.A., and Smith, C.W. (2004). Autoregulation of polypyrimidine tract binding protein by alternative splicing leading to nonsense-mediated decay. Mol. Cell *13*, 91–100.

Zahler, A.M., Tuttle, J.D., and Chisholm, A.D. (2004). Genetic suppression of intronic +1G mutations by compensatory U1 snRNA changes in *Caenorhabditis elegans*. Genetics *167*, 1689–1696.

Zhang, Z., Lotti, F., Dittmar, K., Younis, I., Wan, L., Kasim, M., and Dreyfuss, G. (2008). SMN deficiency causes tissue-specific perturbations in the repertoire of snRNAs and widespread defects in splicing. Cell *133*, 585–600.

Zhao, L., Longo-Guess, C., Harris, B.S., Lee, J.W., and Ackerman, S.L. (2005). Protein accumulation and neurodegeneration in the woozy mutant mouse is caused by disruption of SIL1, a cochaperone of BiP. Nat. Genet. *37*, 974–979.

EXTENDED EXPERIMENTAL PROCEDURES

Mice

The *NMF291* mutant strain was derived from chimeric mice generated from 129S4/SvJae X C57BL/6J F1 ES cells treated with EMS (0.4 μg/ml) and used in a two-generation mating scheme as described (Munroe and Schimenti, 2009). To generate the mutant U2 snRNA transgenic mice, a DNA fragment containing the transcription unit of the mutant *Rnu2-8* and its upstream 780bp and downstream 569bp, was amplified by PCR from the *NMF291* homozygous genomic DNA (Forward, 5′-ctcttgcctagatgggcttg-3′; Reverse, 5′-tctctgcctctatggggttt-3′). The purified DNA fragment was microinjected into the pronuclei of C57BL/6J embryos and founders were identified using PCR. DNA sequencing of amplicons of this primer pair was performed to genotype *NMF291* mice. Genetic mapping of the *NMF291* mutation was performed using an intersubspecific intercross (B6; 129 NMF291 × CAST/Ei). The Jackson Laboratory Animal Care and Use Committee approved all animal protocols.

Histology, Immunohistochemistry, and TUNEL Assay

Mice were intracardically perfused with Bouin's fixative or 4% paraformaldehyde for histology and immunohistology, respectively. Brains were postfixed and embedded in paraffin. Cleaved Caspase-3 (Cell Signaling) immunostaining and TUNEL assays (Roche) were performed as described previously (Zhao et al., 2005).

Immunoprecipitation of snRNPs from Cerebellar Extracts

Frozen mouse cerebella were homogenized with 1ml of reconstitution buffer (20mM HEPES-KOH pH 7.9, 50mM KCl, 5mM $MgCl_2$, 0.2mM EDTA, 5% glycerol) containing 0.01% NP40 as previously described (Gabanella et al., 2007). Homogenates were then passed through a 25G needle five times and centrifuged 15 min at 10,000 rpm at 4°C. Supernatants were collected for IP experiments and protein concentration was measured. Five μg of either the Sm Antigen (Y12) antibody (Lab Vision) or mouse normal IgG (Santa Cruz Biotechnology) conjugated to Dynabeads Protein G (Invitrogen) were incubated with 400μg of cerebellar extracts added to RSB-500 buffer (500mM NaCl, 10mM Tris-HCl pH 7.4, 2.5mM $MgCl_2$) containing 0.1% NP40, protease inhibitor cocktail (Roche), and phosphatase inhibitors (50mM NaF, and 0.2mM Na_3VO_4) at 4°C for 8 hr. After five washes with the same buffer, bound RNAs were recovered from IP products by proteinase K treatment, phenol/chloroform extraction, and ethanol precipitation. Detection of total and mutant U2 snRNAs was performed by real-time PCR as described in Figure S3A.

RNase Protection, Northern Blot, and RT-PCR Assays

Total RNA was extracted from mouse tissues and HEK293 cells using TRIzol (Invitrogen) and treated with DNase I (Ambion). RT-PCR was performed on random-primed cDNA using primer sets described in Tables S2A–S2C. For the RPA probe, a DNA fragment covering nts 7-180 (174nts) of the *Rnu2-8* transcription unit (191nts) was cloned into pCR2.1-TOPO (Invitrogen). The ^{32}P-radiolabeled RNA probe was generated by in vitro transcription of the linearized plasmid and gel purified. RPA analysis was performed as suggested by the manufacturer's instructions (Ambion). Briefly, total RNA was hybridized with radiolabeled RNA probe at 42°C overnight. Non-hybridized RNA was digested by RNase A/T1, and the resulting protected RNA fragments were separated on a 10% denaturing polyacrylamide gel. Density of bands in the scanned X-ray films was determined by ImageQuant 5.2 software (Amersham). Statistical significance was determined by ANOVA and paired t- test (SPSS). For Northern blots, total RNA was also separated on a 10% denaturing polyacrylamide gel. The membrane was hybridized with ^{32}P-end-labeled DNA oligonucleotides corresponding to U2 snRNA (5′- tatcagatattaaactgataagaacagatact-3′) or 5 s rRNA (5′- cctgcttagcttccgagatca-3′).

Constructs and Mutagenesis

For expression of wild-type and mutant U2 snRNA in HEK293T cells, the mutant *Rnu2-8* DNA fragment used to generate transgenic mice and the corresponding wild-type fragment were cloned into pCR2.1-TOPO. The Δ3, Δ6, and Δ9 U2 snRNA expression constructs were generated from the wild-type U2 construct by site-directed mutagenesis (Stratagene). The ISS- (pTN23) reporter was generated from the ISS+ (pTN24) plasmid (Nasim et al., 2002) by deleting the 25bp ISS using the same mutagenesis method. The L1CAM exon27-intron27-exon28 and exon28-intron 28-exon29 cassettes were amplified from C57BL/6J genomic DNA and inserted in frame into pBPLUGA at the SalI and BamHI sites (Kollmus et al., 1996). Primers used for construct generation are described in the Table S2B.

Cell Culture, Transfection, and Luciferase Assays

HEK293T cells grown in DMEM medium containing 10% FBS, were used for transient transfection studies. Briefly, 3 × 10^5 cells/well were plated in a 12-well plate 24 hr before transfection with Lipofectamine 2000 (Invitrogen). 48 hr after transfection, cells were harvested in Passive Lysis Buffer (Promega). Luciferase and β-galactosidase activities were measured as per manufacturer's instructions (Promega) in a multilabel counter. Statistical significance was determined by ANOVA analysis (SPSS).

Functional GO Analysis

The gene lists of differentially expressed genes and exons identified by exon array, differentially expressed junctions found in one or both genotypes and retained introns identified by RNA-Seq, were uploaded into DAVID bioinformatics resources 6.7

(http://david.abcc.ncifcrf.gov/) (Huang da et al., 2009). The functional annotation chart and clustering analysis modules were employed for gene-term enrichment analysis.

Exon Array

Total RNA was isolated by TRIzolPlus (Invitrogen) and cDNA was synthesized, labeled and fragmented using the Affymetrix GeneChip WT Terminal Labeling kit. GeneChip® Mouse Exon 1.0 ST Arrays (Affymetrix) were hybridized with 2.3μg of biotin-labeled cDNA for 16 hr at 45°C. Post-hybridization staining and washing were performed according to manufacturer's protocols using the Fluidics Station 450 instrument (Affymetrix). Arrays were scanned with a GeneChipTM Scanner 3000 (Affymetrix) laser confocal slide scanner.

Affymetrix Expression Console Software was used for array quality assessment. Exon array data treatment was done by the EASANA® analysis system and interface visualization (GenoSplice Technology, http://www.genosplice.com), which is based on the FAST DB® annotations (de la Grange et al., 2007; de la Grange et al., 2005). Data were normalized by using quantile normalization method. Background correction was made using the anti-genomic probes. Probe selection was made as previously described (Clark et al., 2007; de la Grange et al., 2010). Briefly, only probes targeting exons annotated from full-length cDNA were kept for analysis. Among these pre-selected probes, bad quality probes (e.g., probes labeled as ''cross-hybridizing'' by Affymetrix) and probes with intensity signal too low compared to background probes with the same GC content were removed from analysis. Probes with a detection above background (DABG) p value ≤ 0.05 in at least half of chips were considered for further statistical analysis as previously described (Clark et al., 2007; de la Grange et al., 2010). Exon intensities were normalized to the overall intensity of the corresponding gene for each replicate to obtain the normalized exon intensities (NI). The NI of each exon was then compared to that of the other genotype to give the fold change or splicing index. Paired statistical analyses were performed on gene signal intensities and on the splicing index using a Student's paired t test. Results for both gene and exon levels were considered statistically significant at p values < 0.05 and fold-change ≥ 1.5. Note that statistical corrections for sample size were not used to compute p values, thus these values were only used for relative ranking purposes. Primers used for exon array validation are described in the Table S2C. The GEO (Gene Expression Omnibus) accession number for our exon array data is GSE33069.

RNA-Seq Methods

Purification of mRNA, double-stranded cDNA preparation and ligation of barcode-containing adaptors were performed using the mRNA-Seq Sample Prep kit according to the manufacturer's protocol (Illumina). Size selection (300bp) was performed by agarose gel electrophoresis, and PCR was performed to enrich the adaptor-modified DNA fragments. Validation of DNA fragment size was performed using an Agilent Technologies 2100 Bioanalyzer, and DNA concentration was determined by quantitative PCR, following the manufacturer's protocol (Kapa Biosystems). The DNA library was sequenced on an Illumina GAIIX using a 76nt paired-end read strategy following the manufacturer's protocol. The sequences were initially mapped to the mouse genome using CASAVA (Illumina) for assessment of sequence quality. The barcoded reads were separated allowing for 2 mismatches in the barcode tag, and analyzed for their base composition. Any bases at the start of the read deviating from an approximately uniform distribution were removed as they might represent adaptor sequence contamination. After pre-processing, one base was removed from the beginning of all the reads.

For de novo identification of junctions, the pre-processed reads were inputted to SpliceMap 3.3.6 (Au et al., 2010) and aligned to the mouse reference genome (mm9) (Figure S6G). For junctions found only in one genotype, the junctions where the median read number within a genotype was < 3 were filtered out. SpliceMap is not based on previous annotations and thus entire exons adjacent to junction reads were not readily defined. Furthermore the length of ~93.1% of exons in mouse genome is greater than 50bps (Sakharkar et al., 2005). Therefore, we recovered the RPKM (Mortazavi et al., 2008) value of 25bp, which is the minimal exon size SpliceMap 3.3.6 can utilize, upstream and downstream of the donor and acceptor sites of the junction. The larger RPKM value of the two sides was recorded to generate the maxRPKM_25 to represent the isoform expression level. Any junctions in which the ratio of the maxRPKM_25 between the two genotypes was ≥ 2 were also removed. For junctions that appeared in both genotypes, we normalized the junction counts to the isoform expression (maxRPKM_25) to generate the Relative Junction Index (RJI). The log value of RJI was used for two-tailed t tests. Note that statistical corrections for sample size were not used to compute p values for RNA-Seq data, thus these values were only used for relative ranking purposes. To identify differentially expressed junctions with high reliability, we only included the junctions if the median count of junctions within the genotype with higher RJI value was ≥ 3, the ratio of RJI between two genotypes was ≥ 2, and the p value was < 0.05. For intron retention, we only considered reads for further analysis if the maximal median of intron RPKM within one genotype ≥ 2. The maximal RPKM of adjacent exons located to the 5′ and 3′ of the intron (maxRPKM_exon) was recovered for representing the isoform expression. The intron RPKM was normalized to the maxRPKM_exon to generate the Relative Intron retention Index (RII) and the log value of RII was used for two-tailed t tests. To recover retained introns with high reliability, we only included the introns that the ratio of RII between two genotypes was ≥ 2 and the p value was < 0.05.

To associate junctions with genes, junctions were assigned to a given gene if the nearest exon to the donor and acceptor sequence belonged to the same gene in RefSeq annotations, or if the junction matched uniquely to a RefSeq annotated junction. To extract intron length information from RefSeq, annotations were downloaded from UCSC and the length between all annotated exons was recorded. Primers used for RNA-Seq validation are described in Table S2C.

Analysis of Exon Array and RNA-Seq Data Overlap

To analyze the overlap between exon array and RNA-Seq data, we recorded the exon array probe position, which is annotated by the EASANA visualization interface, and localized it in our RNA-Seq data set. For intron retention events detected by exon array, the fold change of the corresponding events from RNA-Seq data was calculated by the ratio of Relative Intron retention Index (RII). For other alternative splicing events detected by exon array, the RNA-Seq junction reads spanning the array probe were recorded if the reads appeared in at least 2 replicates and the ratio of the Relative Junction Index (RJI) was converted into the fold change. If multiple junctions spanned the exon probe, we did not include the event into the comparison analysis. Only 17 non-intron retention events identified by exon array passed these criteria, and our RNA-seq data set indicated 15/17 with the same up-/downregulation direction as detected by exon array. However, these events failed to meet the stringent thresholds set for differential expressed junctions.

SUPPLEMENTAL REFERENCES

Au, K.F., Jiang, H., Lin, L., Xing, Y., and Wong, W.H. (2010). Detection of splice junctions from paired-end RNA-seq data by SpliceMap. Nucleic Acids Res. *38*, 4570–4578.

Clark, T.A., Schweitzer, A.C., Chen, T.X., Staples, M.K., Lu, G., Wang, H., Williams, A., and Blume, J.E. (2007). Discovery of tissue-specific exons using comprehensive human exon microarrays. Genome Biol. *8*, R64.

de la Grange, P., Dutertre, M., Correa, M., and Auboeuf, D. (2007). A new advance in alternative splicing databases: from catalogue to detailed analysis of regulation of expression and function of human alternative splicing variants. BMC Bioinformatics *8*, 180.

de la Grange, P., Dutertre, M., Martin, N., and Auboeuf, D. (2005). FAST DB: a website resource for the study of the expression regulation of human gene products. Nucleic Acids Res. *33*, 4276–4284.

de la Grange, P., Gratadou, L., Delord, M., Dutertre, M., and Auboeuf, D. (2010). Splicing factor and exon profiling across human tissues. Nucleic Acids Res. *38*, 2825–2838.

Gabanella, F., Butchbach, M.E., Saieva, L., Carissimi, C., Burghes, A.H., and Pellizzoni, L. (2007). Ribonucleoprotein assembly defects correlate with spinal muscular atrophy severity and preferentially affect a subset of spliceosomal snRNPs. PLoS One *2*, e921.

Huang, W., Sherman, B.T., and Lempicki, R.A. (2009). Systematic and integrative analysis of large gene lists using DAVID bioinformatics resources. Nat. Protoc. *4*, 44–57.

Kollmus, H., Flohé, L., and McCarthy, J.E. (1996). Analysis of eukaryotic mRNA structures directing cotranslational incorporation of selenocysteine. Nucleic Acids Res. *24*, 1195–1201.

Mortazavi, A., Williams, B.A., McCue, K., Schaeffer, L., and Wold, B. (2008). Mapping and quantifying mammalian transcriptomes by RNA-Seq. Nat. Methods *5*, 621–628.

Munroe, R., and Schimenti, J. (2009). Mutagenesis of mouse embryonic stem cells with ethylmethanesulfonate. Methods Mol. Biol. *530*, 131–138.

Nasim, M.T., Chowdhury, H.M., and Eperon, I.C. (2002). A double reporter assay for detecting changes in the ratio of spliced and unspliced mRNA in mammalian cells. Nucleic Acids Res. *30*, e109.

Pessa, H.K., Ruokolainen, A., and Frilander, M.J. (2006). The abundance of the spliceosomal snRNPs is not limiting the splicing of U12-type introns. RNA *12*, 1883–1892.

Sakharkar, M.K., Perumal, B.S., Sakharkar, K.R., and Kangueane, P. (2005). An analysis on gene architecture in human and mouse genomes. In Silico Biol. (Gedrukt) *5*, 347–365.

Zhao, L., Longo-Guess, C., Harris, B.S., Lee, J.W., and Ackerman, S.L. (2005). Protein accumulation and neurodegeneration in the woozy mutant mouse is caused by disruption of SIL1, a cochaperone of BiP. Nat. Genet. *37*, 974–979.

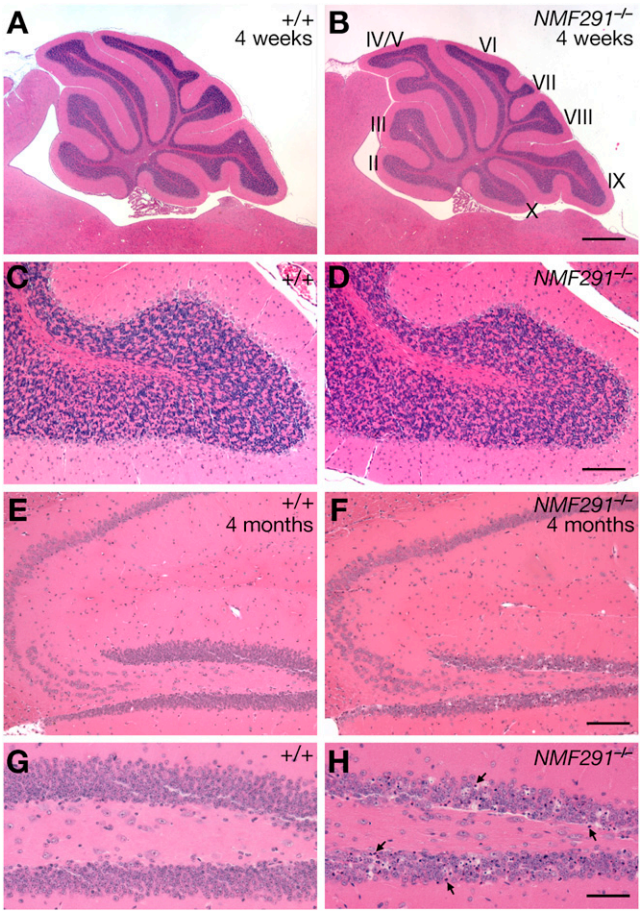

Figure S1. Brain Morphology of *NMF291*$^{-/-}$ Mice, Related to Figure 1

(A–D) Sagittal sections of one-month-old wild-type (+/+, A) and *NMF291*$^{-/-}$ (B) cerebella were stained with hematoxylin and eosin. Cerebellar lobules are indicated by Roman numerals (B). Higher magnification images of lobule IX from wild-type (C) and *NMF291*$^{-/-}$ (D) cerebella.

(E–H) Sagittal sections of the hippocampus of 4-month-old wild-type (E) and *NMF291*$^{-/-}$ (F) mice stained with hematoxylin and eosin. Higher magnification images of the dentate gyrus region from the wild-type (G) and *NMF291*$^{-/-}$ (H) hippocampus. Examples of pyknotic nuclei are labeled by arrows (H). Scale bars: (B), 500 μm; (D), 50 μm; (F), 50 μm; (H), 25 μm.

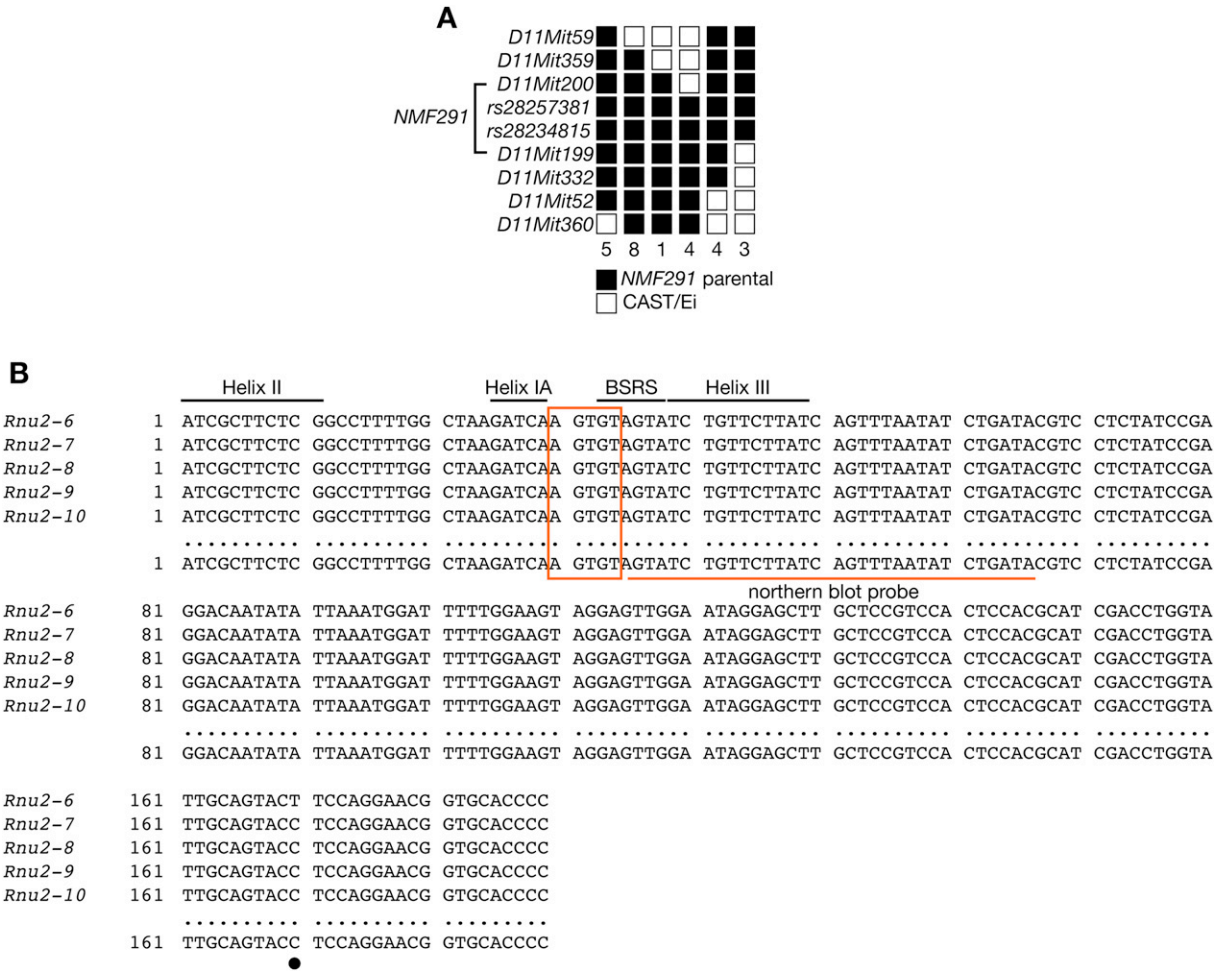

Figure S2. Genetic Mapping of the *NMF291* Mutation and Conservation of *Rnu2-6–Rnu2-10* snRNAs, Related to Figure 2

(A) Haplotypes of recombinant chromosomes from affected mice demonstrated that the *NMF291* mutation is located between *D11Mit200* and *D11Mit199*. The number of mice obtained for each haplotype is shown.

(B) The sequences of *Rnu2-6 – Rnu2-10* snRNAs are identical except for a single nucleotide polymorphism (filled circle) at nucleotide 170 in *Rnu2-6* RNA. The *NMF291* 5-nucleotide deletion is boxed and the U2/U6 Helix Ia, II, and III, and U2 branch site recognition sequences (BSRS) are labeled. The region corresponding to the DNA oligonucleotide probe used for Northern blot analyses is underlined.

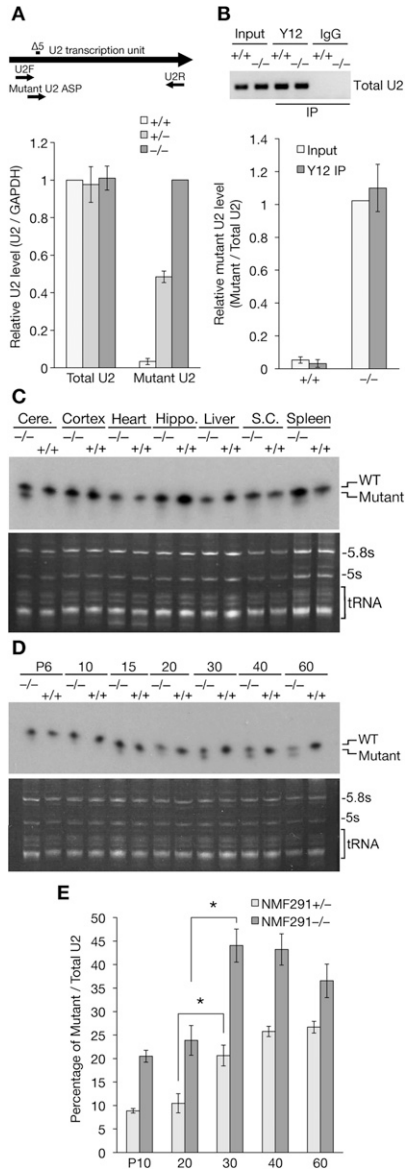

Figure S3. Spatial and Temporal Expression of the Mutant U2 snRNAs and Incorporation of Mutant RNA into Cerebellar U2 snRNPs, Related to Figure 3

(A) Allele specific real-time PCR primers (top) for detecting total U2 snRNA (U2F & U2R) and mutant U2 snRNA (Mutant U2 ASP & U2R) were validated in P30 wild-type (+/+), *NMF291*$^{+/-}$, and *NMF291*$^{-/-}$ cerebellar cDNA (bottom). To generate relative U2 levels, we first normalized total and mutant U2 expression levels to GAPDH levels. Then we defined the wild-type (+/+) normalized total U2 level and *NMF291*$^{-/-}$ normalized mutant U2 level as arbitrary unit one for relative total and mutant U2 expression level, respectively. Note that the relative total U2 snRNA levels in the P30 wild-type, *NMF291*$^{+/-}$, and *NMF291*$^{-/-}$ cerebellum are similar, and that the mutant allele specific primers preferentially (~30 fold) amplify mutant U2 in *NMF291*$^{-/-}$ cerebellar cDNA relative to wild-type U2 in wild-type cerebellar cDNA.

(B) Incorporation of mutant U2 snRNAs into U2 snRNPs in the *NMF291*$^{-/-}$ cerebellum. Immunoprecipitation (IP) experiments were performed using cerebellar supernatants from wild-type and *NMF291*$^{-/-}$ mice. RT-PCR (primers; U2F & U2R, top) detected the total U2 snRNAs present in the input supernatant and in the IP products of the Y12 (*Sm* Antigen) antibody, but not in IP products of the control (normal mouse IgG). Real-time PCR using mutant allele-specific primers demonstrated that the mutant U2 RNAs were present in the mutant input supernatant and Y12 IP products, but not in that of wild-type (bottom).

(C and D) Northern blot analysis of wild-type (+/+) and *NMF291*$^{-/-}$ (–/–) total RNA from P30 neuronal and non-neuronal tissues (C) or from the cerebellum of mice at different postnatal (P) ages (D). The U2 DNA oligo probe for Northern blot is shown in Figure S2B. Ethidium bromide-stained RNA gels are shown as loading controls, and 5.8 s and 5 s rRNA, and tRNA are indicated. Cere, cerebellum; Hippo, hippocampus; S.C., spinal cord.

(E) Quantitative analysis of RNase protection assays performed on *NMF291*$^{+/-}$ and *NMF291*$^{-/-}$ cerebellar RNA at different postnatal (P) ages (days after birth). Values are expressed as the percentage of mutant/total U2 snRNA. Each genotype at each time point was supported by at least three independent mouse samples. *$p < 0.001$, one-way ANOVA.

In all panels, values represent mean ± SEM, n = 3.

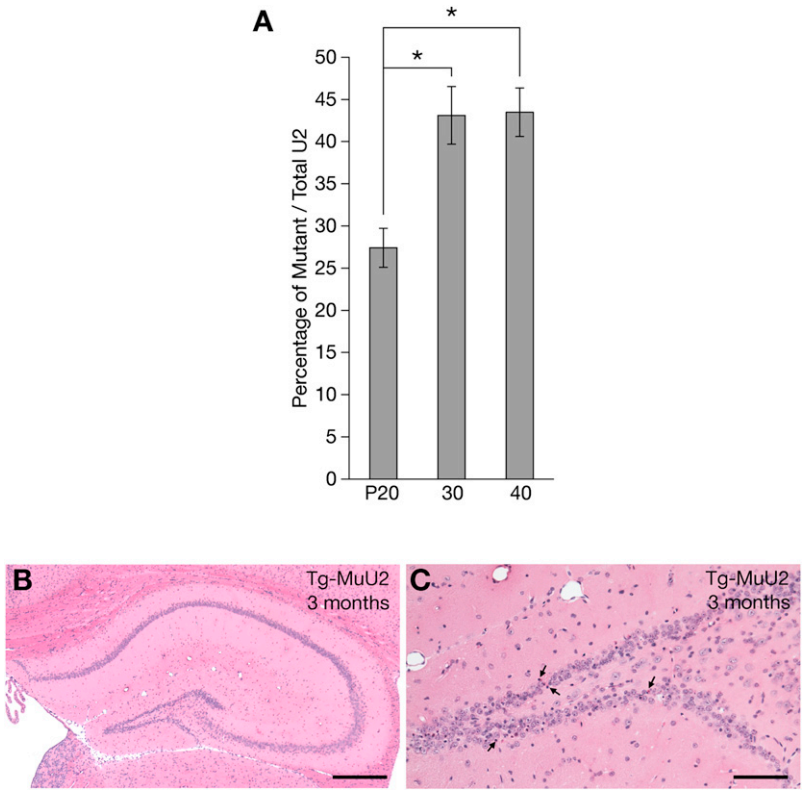

Figure S4. Granule Neuron Loss in Hippocampal Dentate Gyrus Region of Mutant *Rnu2-8* Transgenic Mice, Related to Figure 4

(A) Quantitative analysis of RNase protection assays of Tg-MuU2 mice at different postnatal (P) ages (days after birth). Values are expressed as the percentage of mutant U2 of the total U2 snRNA. Each genotype at each time point was supported by at least three independent mouse samples. *$p < 0.001$, one-way ANOVA. Values represent mean ± SEM, n = 3.

(B and C) Hematoxylin and eosin stained coronal sections of the hippocampus from 3-month-old Tg-MuU2 mice shown at low (B) and higher (C) magnification. Pyknotic nuclei are indicated by arrows (C). Scale bars: (A), 75 μm; (B), 30 μm.

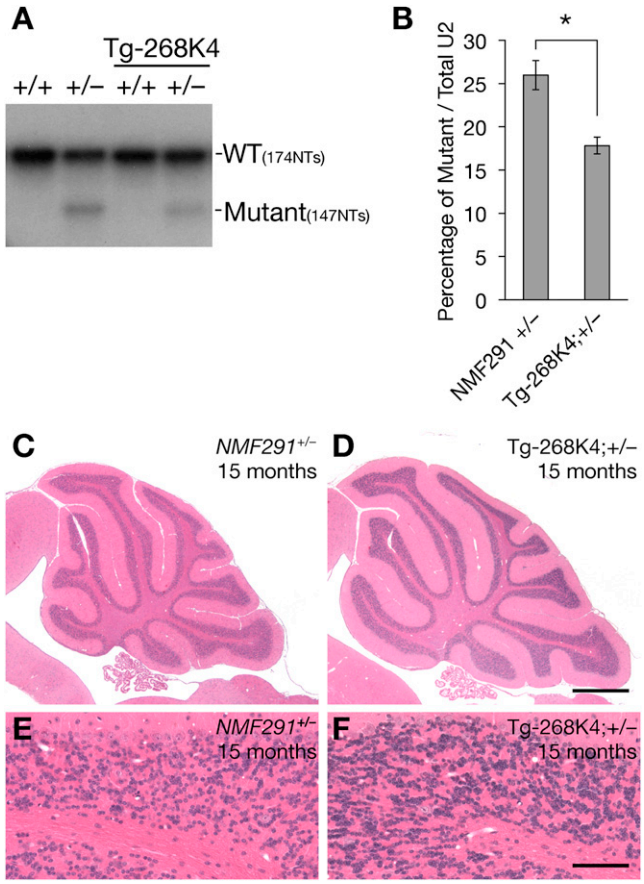

Figure S5. Expression of Wild-Type U2 snRNAs Decreases Neuron Death in Aged Tg-268K4; *NMF291*$^{+/-}$ Mice, Related to Figure 5

(A) RNase protection assays were performed on cerebellar RNA from 15-month-old wild-type (+/+), *NMF291*$^{+/-}$ (+/–), Tg-268K4; +/+, and Tg-268K4; *NMF291*$^{+/-}$ mice.

(B) Quantitative analysis of RNase protection assays of cerebellar RNA from 15-month-old *NMF291*$^{+/-}$ and Tg-268K4; *NMF291*$^{+/-}$ (Tg-268K4; +/–) mice. Values are expressed as the percentage of mutant U2 of the total U2 snRNA. Each genotype was supported by at least three independent mouse samples. *$p < 0.001$, paired t test. Values represent mean ± SEM, n = 3.

(C–F) Hematoxylin and eosin stained sagittal cerebellar sections from aged *NMF291*$^{+/-}$ (+/–; C, E) and Tg-268K4; *NMF291*$^{+/-}$ (Tg-268K4; +/–; D, F) mice. Higher magnification of lobule IV-V is shown in E, F. Note the decreased granule cell loss in the aged Tg-268K4; *NMF291*$^{+/-}$ cerebellum relative to that observed in that of *NMF291*$^{+/-}$ mice. Scale bars: (D), 500 μm; (F), 50 μm.

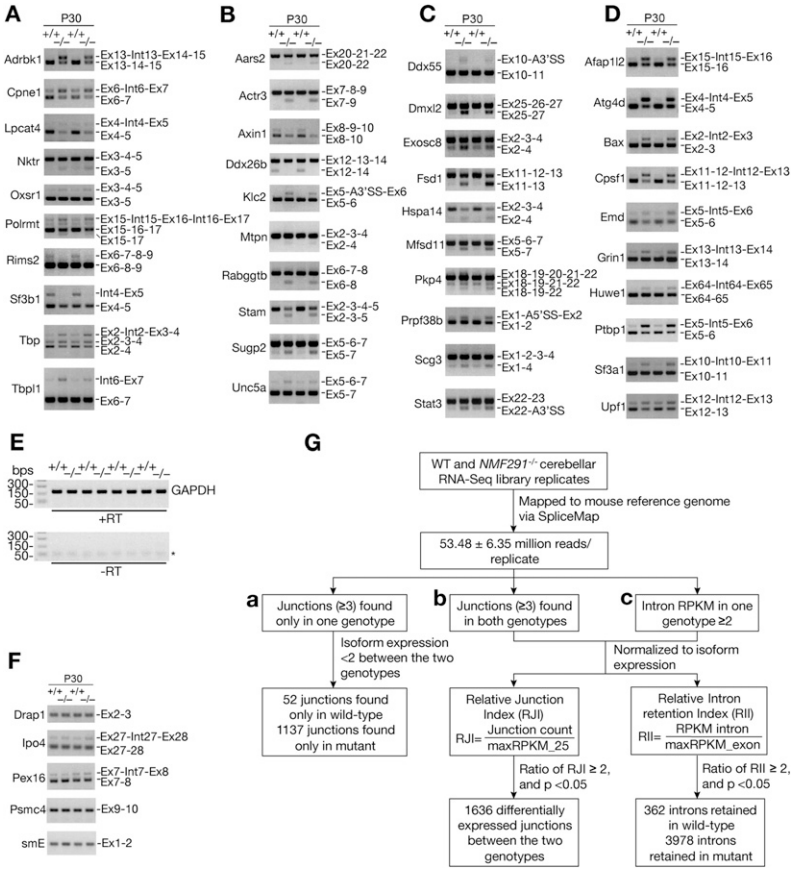

Figure S6. Exon Array and RNA-Seq Analysis, Related to Figure 7

(A) RT-PCR analysis of alternative splicing events predicted to vary between wild-type and *NMF291*$^{-/-}$ mice by exon array analysis. RT-PCR analysis was performed on cerebellar RNA obtained from four pairs of P30 wild-type (+/+) and *NMF291*$^{-/-}$ (–/–) mice, independent of the mice used for the exon array experiment. The identity of RT-PCR products was confirmed by amplicon size and by DNA sequencing. Ten representative reactions from two pairs of wild-type and *NMF291*$^{-/-}$ samples are shown.

(B–D) RT-PCR analysis of junctions differentially expressed between wild-type and mutant cerebella as detected by RNA-Seq analysis. Splicing events in (B) were detected by RNA-Seq as unique junction reads only found in one genotype (median read count $\geq$ 3, and ratio of maxRPKM_25 $\leq$ 2). (C) Junction reads differentially expressed between the two genotypes (ratio of RJI $\geq$ 2, $p < 0.05$). (D) RT-PCR analysis of intron retention events that were predicted by RNA-Seq to increase in the mutant cerebellum. Note these introns were also retained in the wild-type cerebella as a minor form. RT-PCR analysis was performed on cerebellar RNA obtained from four pairs of P30 wild-type (+/+) and *NMF291*$^{-/-}$ (–/–) mice, independent of the mice used for the RNA-Seq experiment. The identity of RT-PCR products was confirmed by amplicon size. Ten representative reactions from two pairs of wild-type and *NMF291*$^{-/-}$ samples (B-D) are shown.

(E) cDNA used for RT-PCR validation of exon array and RNA-Seq analysis was free of genomic DNA contamination. GAPDH was amplified (40 PCR cycles) using a primer pair located within a single exon of the mouse GAPDH gene in the plus RT samples (top), but not in the corresponding minus RT controls (bottom). * indicates PCR primers (bottom).

(F) U12-dependent splicing events were not affected in *NMF291*$^{-/-}$ cerebella. The splicing of five U12-type introns (Pessa et al., 2006) was examined in cerebellar cDNA generated from four pairs of P30 wild-type and *NMF291*$^{-/-}$ mice. The length of *Drap1*, *Ipo4*, *Pex16*, *Psmc4*, and *smE* introns is 85, 117, 85, 182, and 419bps, respectively. Representative gel pictures of reactions from two pairs of wild-type and *NMF291*$^{-/-}$ samples are shown.

(G) RNA-Seq analysis workflow. RNA-Seq libraries were prepared using cerebellar mRNA. Three *NMF291*$^{-/-}$ and two wild-type (WT) mice were used as biological replicates. Libraries were sequenced on an Illumina GAIIX using a 76nt paired-end read strategy and reads were aligned to mouse genome reference via SpliceMap 3.3.6 allowing for a maximum of 4 mismatches. After bar code removal, the length of a mapped read for one end of the pair was 69bp. 53.48 ± 6.35 million reads per replicate were uniquely mapped to the mouse genome. (a) For junctions only found in one genotype, junctions with a median read number $\geq$ 3 were further analyzed. The maximal RPKM of 25bp upstream and downstream of the donor and acceptor site of the adjacent exons (maxRPKM_25) was computed to represent the isoform expression level. Junctions in which the ratio of the maxRPKM_25 $\geq$ 2 between the two genotypes were excluded to avoid potential false positives introduced by differential expression of RNA isoforms between WT and mutant mice. Using these filters, 52 and 1137 junctions were identified as only found in WT and mutant cerebella, respectively. (b) For junctions that were found in both genotypes, we further analyzed those with a median read number $\geq$ 3 for at least one genotype. Junction counts were normalized to the isoform expression (maxRPKM_25) to generate the Relative Junction Index (RJI), and the log value of the RJI was used for a two-tailed t tests. 1636 junctions with a RJI ratio $\geq$ 2 between two genotypes and a p value < 0.05 were identified as differentially expressed between genotypes. (c) For analysis of intron retention, we identified introns with a maximal median of intron RPKM $\geq$ 2 for at least one genotype. The maximal RPKM of adjacent exons (maxRPKM_exon) was computed to represent expression levels of the transcript isoform, and the Relative Intron Retention Index (RII) was generated by normalizing the intron RPKM to the maxRPKM_exon. Two-tailed t tests were performed on the log value of RII. 362 and 3978 introns were identified as differentially retained introns in WT and mutant, respectively, with an RII $\geq$ 2 between the genotypes and a p value < 0.05.

Table S1. Exon Arrays, RNA-Seq, and Functional GO Analysis, Related to Figure 7. (A) Differentially expressed genes detected by exon array. (B) Differentially expressed exons detected by exon array grouped into eight alternative splicing categories. (C) RNA-Seq read details for each replicate. (D) Differentially expressed junctions found in both wild-type and *NMF291*$^{-/-}$ cerebella. (E) Exon junctions found only in wild-type or *NMF291*$^{-/-}$ cerebella. (F) Differential intron retention between wild-type and *NMF291*$^{-/-}$ cerebella. (G) GO analysis for differentially expressed and differentially spliced genes identified by exon array and RNA-Seq. (H) Overlap of intron retention events between exon array and RNA-Seq analyses.

Table S2. Primer Sequences, Related to Experimental Procedures. (A) Primer sequences for real-time PCR. (B) Primer sequences for L1CAM alternative splicing, splicing reporters, and construct mutagenesis. (C) Primer sequences for exon array and RNA-Seq validation.

Movie S1. Progressive Ataxia in *NMF291*$^{-/-}$ Mice, Related to Figure 1. Videos of an *NMF291*$^{-/-}$ mouse taken at 2 week intervals from 4–14 weeks of age demonstrate the progressive loss of motor control.

Cell

Mutation of a U2 snRNA Gene Causes Global Disruption of Alternative Splicing and Neurodegeneration

Yichang Jia,[1] John C. Mu,[2] and Susan L. Ackerman[1,*]
[1]Howard Hughes Medical Institute and The Jackson Laboratory, 600 Main Street, Bar Harbor, ME 04609, USA
[2]Department of Electrical Engineering, Stanford University, Stanford, CA 94305-4065, USA
*Correspondence: susan.ackerman@jax.org
DOI 10.1016/j.cell.2011.11.057

SUMMARY

Although uridine-rich small nuclear RNAs (U-snRNAs) are essential for pre-mRNA splicing, little is known regarding their function in the regulation of alternative splicing or of the biological consequences of their dysfunction in mammals. Here, we demonstrate that mutation of *Rnu2-8*, one of the mouse multicopy U2 snRNA genes, causes ataxia and neurodegeneration. Coincident with the observed pathology, the level of mutant U2 RNAs was highest in the cerebellum and increased after granule neuron maturation. Furthermore, neuron loss was strongly dependent on the dosage of mutant and wild-type snRNA genes. Comprehensive transcriptome analysis identified a group of alternative splicing events, including the splicing of small introns, which were disrupted in the mutant cerebellum. Our results suggest that the expression of mammalian U2 snRNA genes, previously presumed to be ubiquitous, is spatially and temporally regulated, and dysfunction of a single U2 snRNA causes neuron degeneration through distortion of pre-mRNA splicing.

INTRODUCTION

Splicing of pre-mRNAs is performed by the spliceosome machinery consisting of numerous proteins and five small nuclear RNAs (snRNAs) (Wahl et al., 2009). Assembly of the major spliceosome, responsible for splicing of over 90% of human pre-mRNAs, begins with the recruitment of U1 snRNPs (small nuclear ribonucleoprotein particles) to the pre-mRNA 5′ exon/intron junction via base pairing of the U1 snRNA with the splice site. U2 snRNPs subsequently bind to the pre-mRNA branchpoint sequence (BPS) near the 3′ intron boundary, also in part via base-pairing interactions. Further remodeling of the spliceosome results in the recruitment of additional snRNPs, including U6 snRNPs that will replace U1 snRNPs at 5′ pre-mRNA splice sites. Base pairing of U6 with U2 snRNAs juxtaposes the 5′ splice site and the BPS, the reactants of the first transesterification reaction. Thus, recognition and removal of introns and subsequent exon ligation depend in part on the dynamic base pairing of snRNAs with pre-mRNAs and with each other.

Given the critical importance of pre-mRNA splicing to the regulation of gene expression and proteome diversity, it follows that mutations in RNA-processing proteins that may influence pre-mRNA splicing cause human disease (Cooper et al., 2009; Licatalosi and Darnell, 2006). Indeed, dominant mutations in multiple ubiquitously expressed protein components of the U4/U5/U6 tri-snRNP cause retinitis pigmentosa (Mordes et al., 2006). Mutations in the *SMN1* (survival of motor neuron 1) gene, which encodes a protein essential for U snRNP biogenesis, cause motor neuron degeneration in patients with spinal muscular atrophy (SMA) (Lefebvre et al., 1995). Although *SMN* is ubiquitously expressed, alterations in the levels of individual snRNAs and numerous aberrant transcripts were observed in a tissue-specific fashion in *SMN*-deficient mice (Zhang et al., 2008). Mutations in genes encoding the ubiquitously expressed DNA/RNA-binding proteins, TDP-43 and FUS/TLS, are associated with some cases of familial and sporadic amyotrophic lateral sclerosis and frontotemporal dementia (Lagier-Tourenne et al., 2010; Lemmens et al., 2010). Recent studies demonstrated that decreased expression or altered subcellular localization of TDP-43 resulted in reduced expression and altered splicing of multiple mRNAs (Polymenidou et al., 2011; Tollervey et al., 2011). These findings strongly implicate alterations in RNA processing as a key event in several neurodegenerative disorders. However, given the multiple functions of these proteins, the pathogenic basis of these diseases remains unclear.

Recently, mutations in the gene encoding U4atac snRNA, a component of the minor spliceosome that splices a restricted (U12-dependent) class of introns found in less than 1% of human genes, have been linked to the developmental disorder microcephalic osteodysplastic primordial dwarfism (Edery et al., 2011; He et al., 2011). However, to date, mutations in the major spliceosomal snRNA genes have not been associated with disease, perhaps in part due to their ubiquitous expression and essential function. Furthermore, unlike the *U4atac* gene, the snRNAs of the major spliceosome are encoded by multiple genes and pseudogenes in metazoans (Marz et al., 2008), suggesting that these genes are highly redundant. Although differing in organization (e.g., U1 and U2 genes exist in large chromosomal

clusters in the human genome, whereas other snRNA genes are not clustered; Manser and Gesteland, 1982; Van Arsdell and Weiner, 1984; Westin et al., 1984), sequence analysis of snRNA genes suggests that they have apparently undergone concerted evolution, i.e., members of gene families are identical or nearly so within a species (Marz et al., 2008; Pavelitz et al., 1995). However, the effect of polymorphisms in individual members of these repetitive gene families on pre-mRNA splicing and the extent to which the expression of single genes is independently regulated are largely unknown.

Here, we report that a 5 nucleotide (nt) deletion in one member of a cluster of mouse U2 snRNA genes causes neurodegeneration and alternative splicing defects, including the retention of small introns. Our study provides definitive evidence for the causative role of splicing dysfunction in neurodegeneration and a model to dissect the role of major spliceosomal snRNAs on the regulation of mammalian pre-mRNA splicing.

RESULTS

Progressive Neurodegeneration in *NMF291* Mutant Mice

The *NMF* (Neuroscience Mutagenesis Facility) *291* mutation was identified in a chemical mutagenesis screen for recessive mutations that result in neurological phenotypes (Bult et al., 2004). Mice homozygous for this mutation developed mild tremors by 8 weeks of age, which progressed to overt truncal ataxia by 12 weeks (see Movie S1 available online). At 4 weeks of age, the brains of mutant mice appeared grossly normal (Figures S1A–S1D). However, histological analysis revealed granule cells with pyknotic nuclei in the mutant cerebellum beginning at 4 weeks of age (data not shown). Neuron loss was progressive, and by 4 months of age, most granule cells had degenerated (Figures 1A–1F). However, other cerebellar neurons, including Purkinje cells, did not degenerate, even in aged mice (data not shown). Although neuron death was most severe in the cerebellum, later-onset degeneration of granule cells in the dentate gyrus region of the hippocampus was also observed (Figures S1E–S1H).

To determine the nature of neuron death, immunostaining with activated caspase-3 antibodies was performed on cerebellar sections from 6-week-old mice. Many immunopositive granule cells were observed in the mutant, but not the wild-type (WT) cerebellum, suggesting that mutant neurons undergo apoptosis (Figures 1G and 1H). Granule cell apoptosis was confirmed by TUNEL (TdT-mediated dUTP nick end labeling) analysis (Figures 1I and 1J).

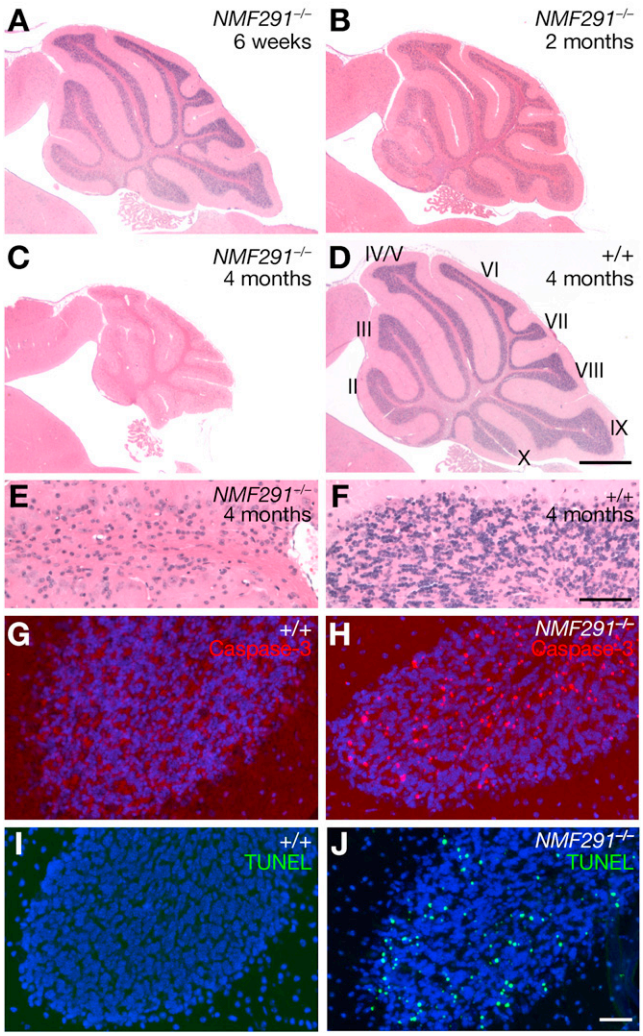

Figure 1. Progressive Granule Cell Degeneration in the *NMF291*$^{-/-}$ Cerebellum

(A–F) Hematoxylin and eosin-stained sagittal sections of WT (+/+) and *NMF291*$^{-/-}$ cerebella. Cerebellar lobules are indicated by Roman numerals (D). (E and F) Higher-magnification images of lobule IV/V from (C) and (D).

(G–J) Cleaved caspase-3 immunostaining (G and H) and TUNEL analysis (I and J) of sections from 6-week-old cerebella. Sections were counterstained with Hoechst 33342.

Scale bars, 500 μm (D), 50 μm (F), and 10 μm (J). See also Figure S1 and Movie S1.

The *NMF291* Mutation Deletes 5 nt in the *Rnu2-8* U2 snRNA

The *NMF291* mutation was initially localized to distal Chromosome 11 by a genome scan analysis of F2 mice using polymorphic microsatellite markers. Additional recombination mapping narrowed the mutation interval to a 0.52 cM (0.34 Mb) region between *D11Mit200* and *D11Mit199* containing eight protein-coding genes (Figures 2A, 2B, and S2A). No coding sequence polymorphisms between mutant and WT DNA were found in these genes, nor did we observe differences in the expression of the cerebellar transcripts of these genes between genotypes (data not shown).

In addition to the protein-coding genes, a cluster of five U2 snRNA (*Rnu2-6* to *Rnu2-10*) genes also resides in the *NMF291* critical interval (Figure 2B). The RNAs encoded by these genes are identical, except for a single nucleotide polymorphism in *Rnu2-6* (Figure S2B). Sequencing of mutant genomic DNA revealed a 5 bp deletion between nt 30 and 34 (30AGUGU34) in a highly conserved region of the *Rnu2-8* transcription unit (Figures 2C and 2D). This deletion removes the first 2 nt of the U2 consensus branch site recognition sequence (BSRS)

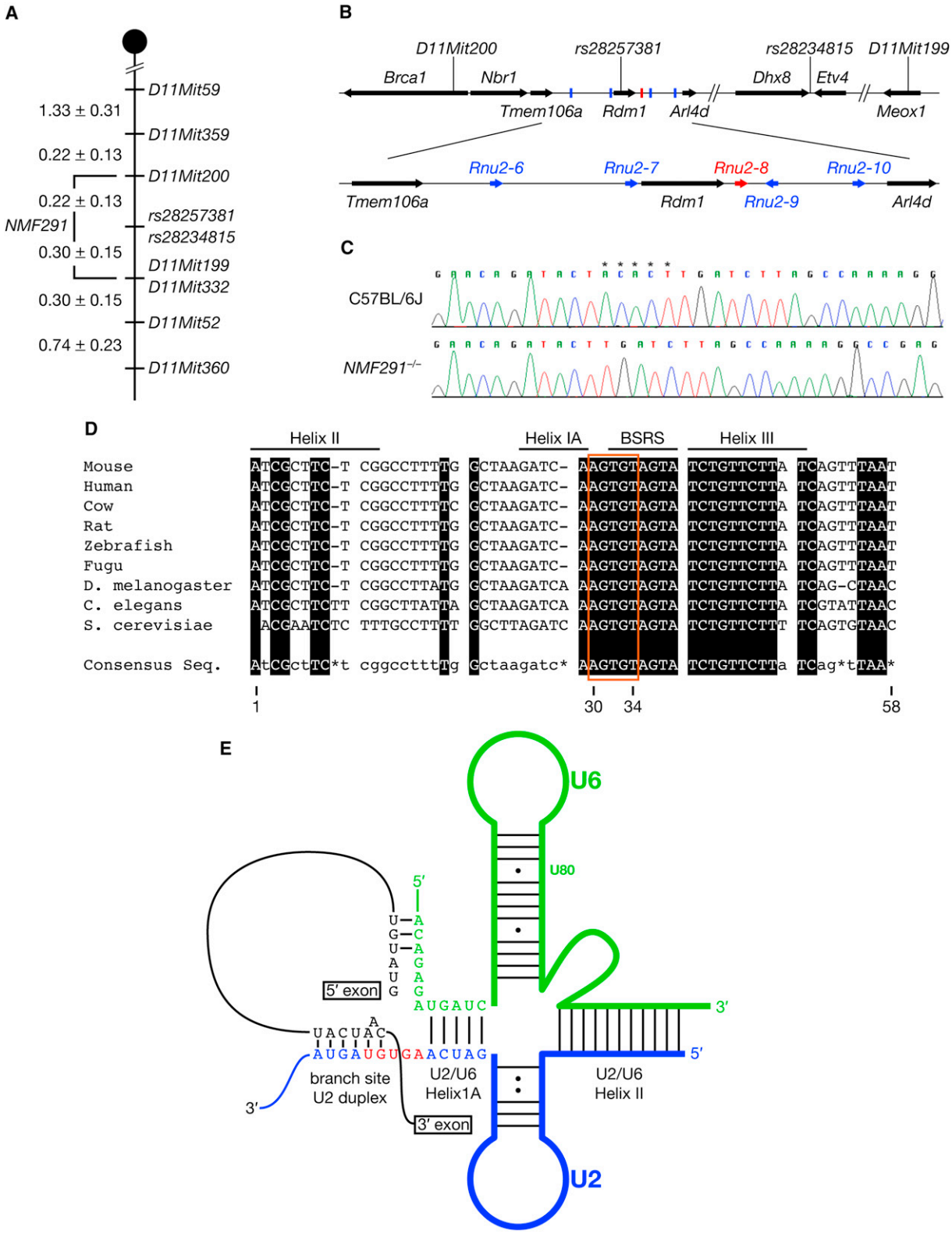

Figure 2. The *NMF291* Mutation Is a 5 nt Deletion in a U2 snRNA Gene

(A) The *NMF291* mutation was mapped to Chromosome 11 between *D11Mit200* and *D11Mit199* (values are in cM ± SEM).

(B) The *NMF291* critical interval contains eight protein-coding genes (arrows) and five U2 snRNA genes (*Rnu2-6*–*Rnu2-10*; bars, top panel).

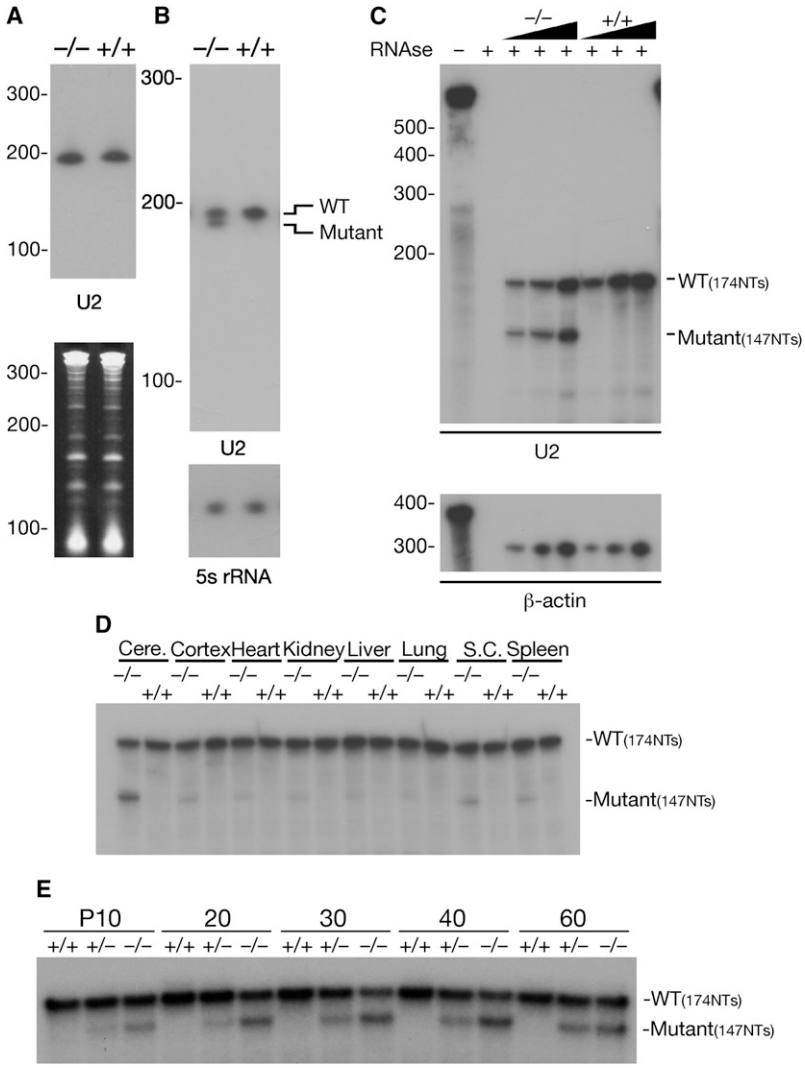

Figure 3. The Expression of *Rnu2-8* Is Temporally and Spatially Regulated

(A and B) Total RNA from WT and *NMF291*$^{-/-}$ (−/−) P30 cerebella was separated by denaturing acrylamide gels for shorter (A) or longer (B) periods and subsequently analyzed by northern blot analysis using an U2-specific oligonucleotide probe. For loading controls, the gel was stained with ethidium bromide (A, bottom), or the membrane was rehybridized with a probe for 5S rRNA (B).

(C) RPA using increasing amounts of cerebellar RNA (0.2–1 μg) from P30 WT and *NMF291*$^{-/-}$ mice. For loading controls, RPA was also performed using a β-actin RNA probe.

(D) RPA analysis of U2 snRNAs in various tissues taken from P30 WT and *NMF291*$^{-/-}$ mice.

(E) RPA analysis of U2 snRNAs in WT, *NMF291*$^{+/-}$ (+/−), and *NMF291*$^{-/-}$ cerebella at different postnatal (P) ages (days after birth). Cere., cerebellum; S.C., spinal cord.

See also Figure S3.

RNase protection assays (RPAs) using cerebellar RNA isolated from P30 WT and mutant mice. Total U2 snRNA levels were similar between the WT and the *NMF291*$^{-/-}$ cerebellum (Figure 3A), and both WT and the deletion-containing *Rnu2-8* RNAs were detected in the mutant cerebellum (Figures 3B and 3C), with the mutant transcript found at 78.9% ± 6.3% (n = 6) of the level of the WT U2 snRNA (or ~45% of total U2 levels). Similar analysis of highly pure granule cell cultures demonstrated that both WT and mutant U2 RNAs were expressed within the same cell type (data not shown). Finally, immunoprecipitation experiments using Y12 antibody, which precipitates U snRNPs (Lerner et al., 1981), demonstrated that the mutant U2 snRNAs were assembled into mutant cerebellar U2 snRNPs (Figures S3A and S3B), consistent with previous reports that the free snRNA pool is relatively very small and unstable (Sauterer et al., 1988).

Mammalian U2 snRNAs, like other U snRNAs, are believed to be ubiquitously and highly expressed (Egloff et al., 2008; Hernandez, 2001). However, neurodegeneration in *NMF291*$^{-/-}$ mice was very distinct, with profound neuron loss occurring within the cerebellum beginning at P30. To determine if expression of mutant *Rnu2-8* correlates with the specificity of pathological changes, we performed RPA and northern blot assays using neuronal and non-neuronal tissues from the P30 WT and

(33GUAGUA38) and the 3 nt linker region (30AGU33) between the BSRS and U2/U6 helix IA (Figures 2D and 2E) (Wahl et al., 2009). The deletion was not observed in genomic DNA from several other inbred stains, including C57BL6/J and 129S4/SvJae, from which the F1 ES cells used for mutagenesis were derived (data not shown).

Rnu2-8 Is Spatially and Temporally Regulated

To confirm that the U2 gene disrupted by the *NMF291* deletion is indeed expressed, we performed northern blot analysis and

(C) Sequence chromatograms of WT (C57BL6/J) and mutant (*NMF291*$^{-/-}$) *Rnu2-8* genomic DNA amplified using unique primers outside of the transcription unit. Asterisk (*) indicates nucleotides deleted in the mutant genome.

(D) Deleted nucleotides are evolutionarily conserved. Conserved nucleotides are boxed in black and indicated in uppercase letters in the consensus sequence. Nucleotides with one or more mismatches or absent across species are indicated in the consensus sequence in lowercase letters or with an asterisk, respectively. The U2 BSRS, and the nucleotides in helices IA, II, and III, which base pair with U6 snRNA, are indicated. Nucleotides are numbered according to the mouse sequence.

(E) The schematic of RNA:RNA interactions contributing to the first step of splicing. The 5 nt deletion in *Rnu2-8* is highlighted in red.

See also Figure S2.

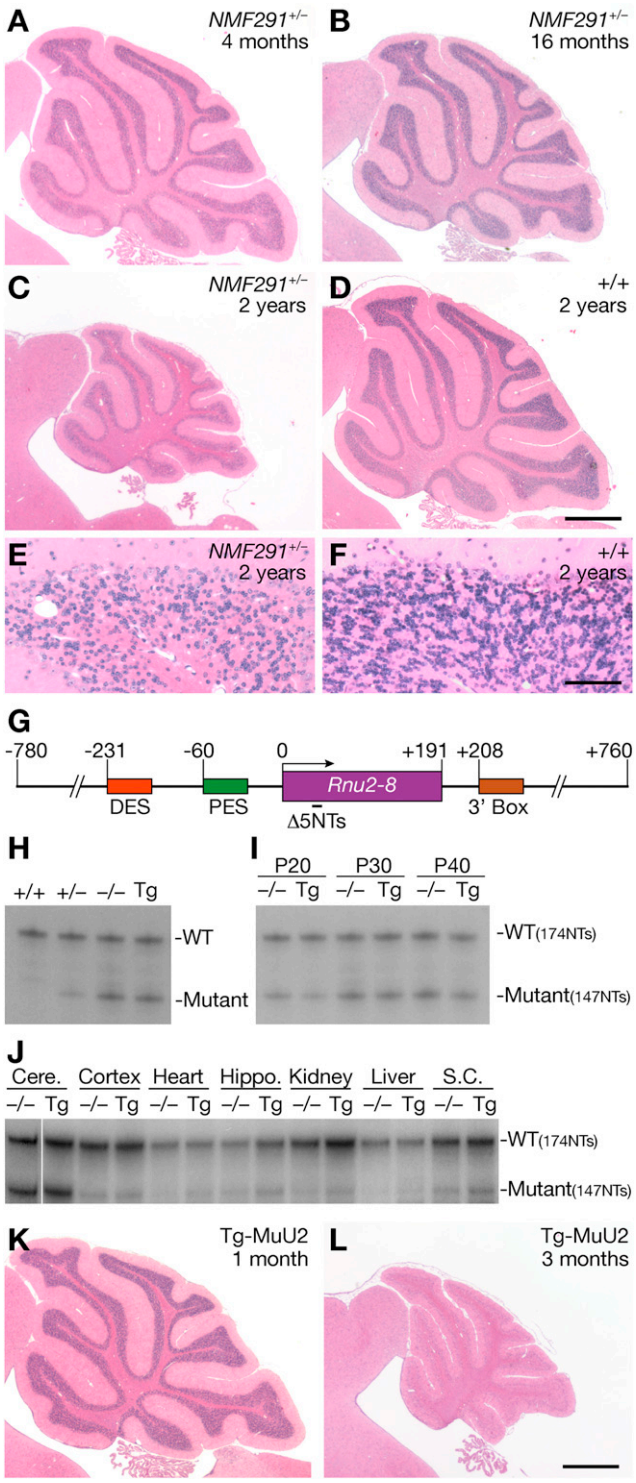

Figure 4. Mutant *Rnu2-8* Acts in a Dosage-Dependent Fashion on Neuron Survival

(A–F) Hematoxylin and eosin-stained sagittal sections of *NMF291*$^{+/-}$ and WT (+/+) cerebella. (E and F) Higher-magnification images of lobule IV/V from (C) and (D).

(G) The 1.5 kb DNA fragment, containing the transcription unit of the mutant *Rnu2-8* and its 5′ and 3′ flanking sequences, used for pronuclear injection.

(H) RPA analysis of cerebellar RNA from P30 WT, *NMF291*$^{+/-}$, *NMF291*$^{-/-}$ mice, and mice hemizygous for the mutant *Rnu2-8* transgene (Tg).

(I) RPA analysis of cerebellar RNA from P20, P30, and P40 *NMF291*$^{-/-}$ mice and mice hemizygous for the transgene (Tg).

(J) RPA analysis of tissues from P30 *NMF291*$^{-/-}$ and hemizygous Tg-MuU2 mice. Note that the *NMF291*$^{-/-}$ cerebellar lane was run on a separate gel.

(K and L) Hematoxylin and eosin-stained sagittal sections of Tg-MuU2 cerebella. DES, distal sequence element; PES, proximal sequence element. Scale bars, 500 μm (D and L) and 50 μm (F). See also Figure S4.

homozygous mutant mice (Figures 3D and S3C). Surprisingly, mutant *Rnu2-8* was differentially expressed between tissues, with highest levels observed in the cerebellum. Furthermore, mutant *Rnu2-8* expression was also temporally regulated in the postnatal cerebellum. Mutant U2 RNAs comprised ~20%–25% of the total U2 RNA levels in the P10 and P20 *NMF291*$^{-/-}$ cerebellum but rose to ~45% of the total level at P30 (Figures 3E, S3D, and S3E). This increase was maintained at P40 but dropped slightly at P60, likely due to neuron loss in the mutant cerebellum. This temporal regulation of expression was also observed in heterozygous mice, where amounts of mutant U2 RNA were approximately half of that observed in homozygous mice (Figures 3E and S3E). Together, these data suggest that mammalian U2 snRNAs display previously unsuspected temporal and spatial variation with the expression of mutant *Rnu2-8* correlating with the onset and specificity of neurodegeneration in the *NMF291*$^{-/-}$ mouse.

Mutant *Rnu2-8* Induces Neurodegeneration in a Dosage-Dependent Manner

Although mice homozygous for the *NMF291* mutation were originally ascertained in our screen, the site of the *Rnu2-8* deletion, the multicopy nature of the U2 genes, and the expression of WT U2 snRNAs in the mutant cerebellum suggested that this mutation might act in a gene dosage-dependent fashion. To investigate this possibility, we performed histological analysis of the cerebellum of *NMF291*$^{+/-}$ mice. Apoptotic granule cells were observed in the cerebellum of 1-month-old and older *NMF291*$^{+/-}$ mice, but the number of dying neurons was considerably reduced compared to that observed in homozygous *NMF291* mice (data not shown). Differences in the overall size of the *NMF291*$^{+/-}$ cerebellum were not obvious until mice were close to 2 years of age, when mild tremors were apparent, and histological analysis revealed that many granule cells had degenerated (Figures 4A–4F).

To further test the mechanism of the *Rnu2-8* mutation, we generated mice transgenic for a 1.5 kb genomic DNA fragment containing the mutant *Rnu2-8* transcriptional unit and the basal regulatory elements necessary for U2 transcription and processing (Figure 4G) (Egloff et al., 2008; Hernandez, 2001). Mice from one transgenic line (Tg-MuU2) expressed mutant *Rnu2-8* in the cerebellum, and expression was temporally and spatially regulated similar to that observed in *NMF291*$^{-/-}$ mice (Figures 4H–4J and S4A). Like *NMF291*$^{-/-}$ mice, hemizygous mice from this line developed pronounced ataxia by 12 weeks of age (data not shown). Histological analysis revealed dying granule cells in the cerebellum of 1-month-old transgenic mice, and by 3 months of age, most granule cells had died, similar to the

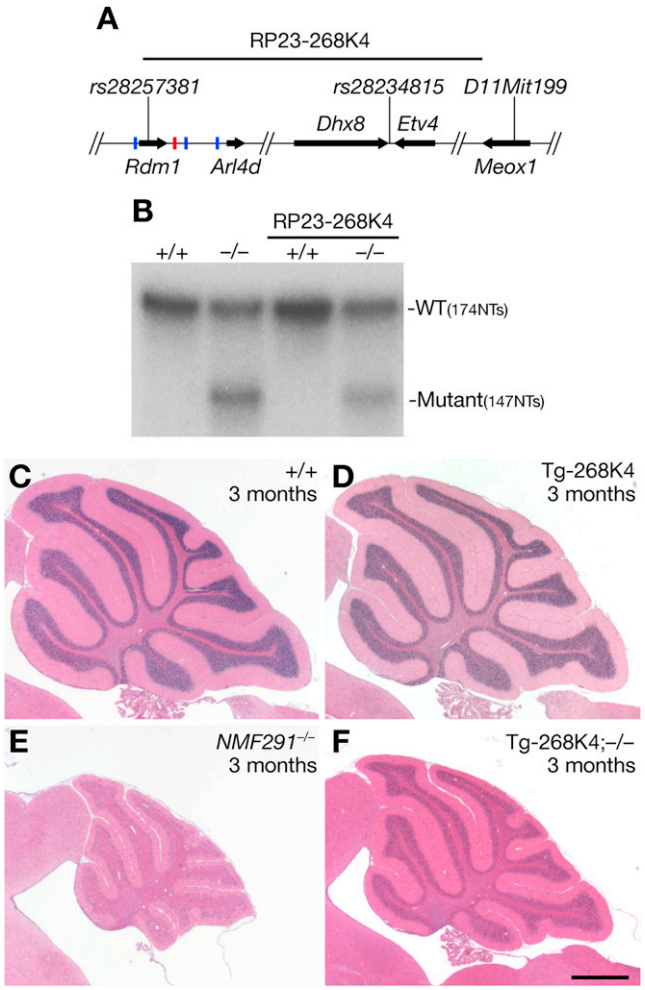

Figure 5. Transgenic Expression of WT U2 snRNAs Partially Rescues the *NMF291*$^{-/-}$ Phenotype

(A) Schematic of the RP23-268K4 BAC, containing three snRNA genes (*Rnu2-8*, red bar; *Rnu2-9* and *-10*, blue bars), used for transgenesis.

(B) RPA of cerebellar RNA from 1-month-old WT (+/+) or *NMF291*$^{-/-}$ (–/–) mice with or without the BAC transgene (RP23-268K4).

(C–F) Hematoxylin and eosin-stained sagittal sections of WT (+/+), RP23-268K4 (Tg-268K4), *NMF291*$^{-/-}$, and Tg-268K4; –/– cerebella.

Scale bar, 500 μm (F). See also Figure S5.

time course of neuron death in *NMF291*$^{-/-}$ mice (Figures 4K and 4L; data not shown). As observed in *NMF291*$^{-/-}$ mice, neuron loss in the dentate gyrus was observed in 3-month-old transgenic mice (Figures S4B and S4C).

If the severity of neurodegeneration is indeed dependent on the ratio of mutant to WT snRNAs, then the complementary experiment in which an increase in expression of WT U2 RNA on the *NMF291*$^{-/-}$ background should lead to attenuation of pathology. To test this hypothesis, we generated a transgenic mouse line carrying a BAC (bacterial artificial chromosome RP23-268K4) containing *Rnu2-8* and two other U2 genes (*Rnu2-9* and *-10*; Figure 5A). This line was crossed to *NMF291* mice to generate *NMF291*$^{-/-}$ mice carrying the BAC transgene. The percentage of mutant/total U2 snRNA was reduced in the cerebellum of Tg-268K4; *NMF291*$^{-/-}$ and Tg-268K4; *NMF291*$^{+/-}$ mice relative to that observed in the cerebellum of age-matched *NMF291*$^{-/-}$ and *NMF291*$^{+/-}$ mice (Figures 5B, S5A, and S5B). Neurodegeneration was also decreased in the cerebellum of 3-month-old Tg-268K4; *NMF291*$^{-/-}$ mice relative to that of age-matched *NMF291*$^{-/-}$ mice (Figures 5C–5F). Surprisingly, when mutant U2 RNAs represented ~17% of total U2 levels, little granule cell loss was observed in aged Tg-268K4; *NMF291*$^{+/-}$ mice (Figures S5C–S5F). When the percentage of mutant/total U2 RNA increased to ~25% as observed in the *NMF291*$^{+/-}$ cerebellum, neurodegeneration was slowly progressive (Figures 4A–4F). However, when this percentage reached ~45% (as in the P30 *NMF291*$^{-/-}$ and Tg-MuU2 cerebellum), rapid granule neuron loss was observed (Figures 1C and 4L). Taken together, our data demonstrate that the expression of the mutant *Rnu2-8* gene is sufficient to induce granule cell death even in the presence of WT U2 expression, and the extent of neuron loss is dependent on the expression level of the mutant U2 snRNAs relative to that of the WT U2 snRNA.

Expression of the Mutant U2 snRNA Decreases Splicing Efficiency

The central role of U2 snRNA in pre-mRNA splicing suggested that abnormalities in this process underlie neurodegeneration in *NMF291*$^{-/-}$ mice. To study the impact of the mutant *Rnu2-8* on pre-mRNA splicing, we employed a previously reported splicing reporter construct, TN24 (ISS+), which encodes both β-galactosidase and luciferase separated by an exon-intron-exon cassette (Kollmus et al., 1996; Nasim et al., 2002). Although β-galactosidase is constitutively expressed from this plasmid, luciferase is only expressed when accurate splicing occurs between the adenovirus 5′ exon and the alternatively spliced SK exon of human *Tpm3* (see diagram in Figure 6C).

HEK293T cells were transfected with ISS+ alone, or cotransfected with the reporter and a 1.5 kb genomic DNA fragment containing the WT or the mutant (Δ5nt) U2 transcription unit (Figures 6A–6C). As controls, cells were cotransfected with the reporter and a plasmid encoding the RNA-binding protein hnRNPG, which has been shown to silence splicing of this exon-intron-exon cassette via binding of the 25 bp intronic-splicing silencer (ISS) (Nasim et al., 2002). Transfection of WT *Rnu2-8* did not have a significant effect on reporter splicing as determined by the ratio of luciferase/β-galactosidase activity or by RT-PCR (Figure 6C). However, transfection of mutant *Rnu2-8* led to a significant decrease (28%; $p < 0.01$) in the splicing efficiency of the reporter compared to that of cells transfected with reporter alone.

Similar experiments were performed using the same reporter lacking the 25 bp ISS (ISS–) (Nasim et al., 2002) (Figure 6D). In agreement with the role of the ISS sequence in splicing silencing, we observed a 4- to 5-fold increase in splicing of this reporter over that of the reporter containing the ISS sequence. As previously shown (Nasim et al., 2002), the inhibitory effect of *hnRNPG* expression on ISS– reporter splicing was greatly reduced (Figure 6D). As observed for the ISS+ reporter, splicing of the ISS– reporter was not changed by expression of the WT U2. However, in contrast to the attenuation of ISS+ reporter splicing

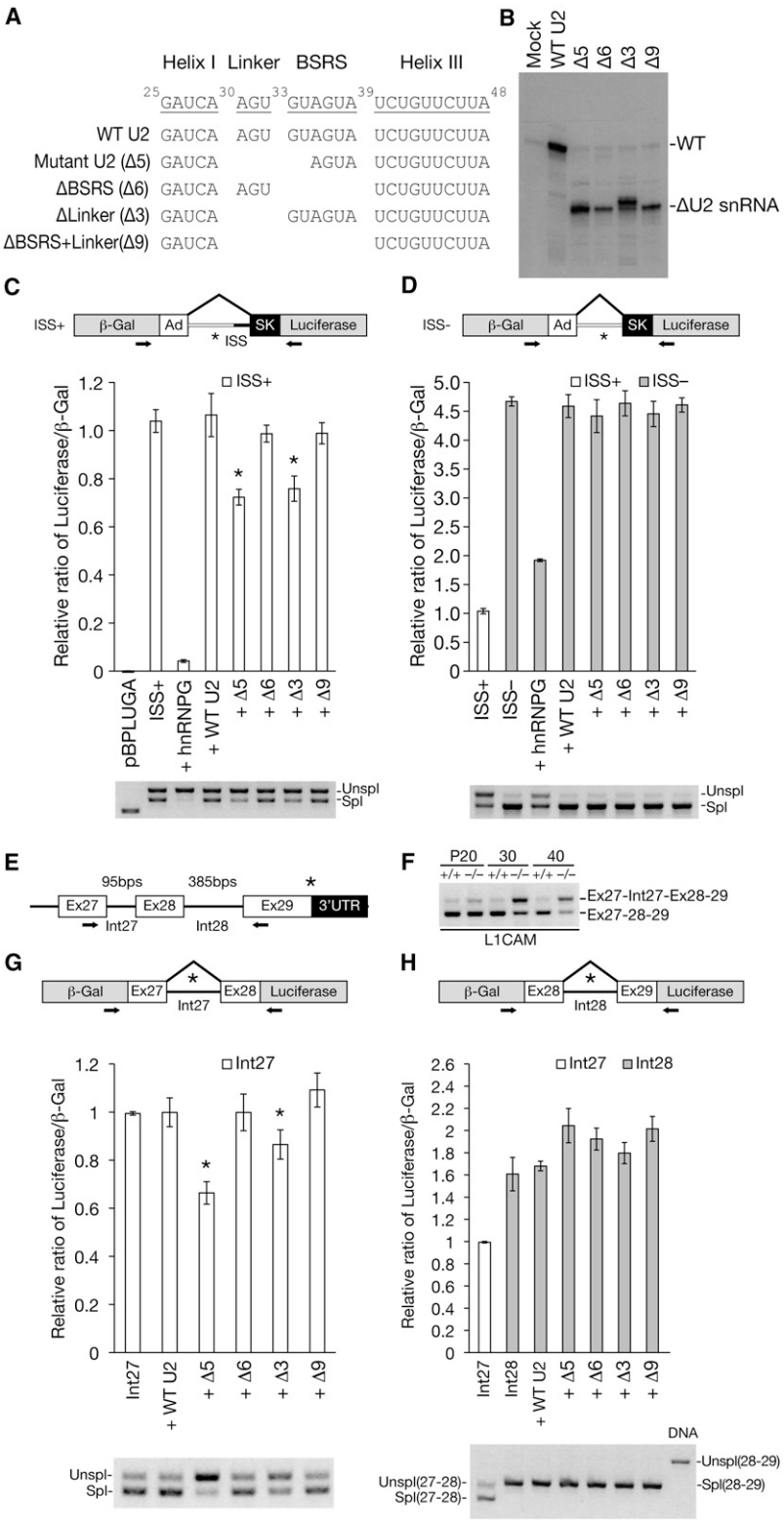

Figure 6. Mutant *Rnu2-8* Selectively Decreases Splicing Efficiency of Introns

(A) The sequences of WT and deletion (Δ) U2 constructs used for cell transfection experiments.

(B) RPA analysis of RNA from mock-transfected HEK293T cells or cells transfected with WT or ΔU2 plasmids.

(C and D) HEK293T cells were transfected with the ISS+ splicing reporter (C) or the ISS− splicing reporter (D), or cotransfected with WT or ΔU2 constructs as indicated. The splicing of pBPLUGA parental vector is shown in (C) as a control, and the splicing of the ISS+ reporter is shown in (D) as a reference. The splicing efficiency of the reporters was measured by luciferase/β-Gal (β-galactosidase) activity (top panels in C and D) and confirmed by RT-PCR (bottom panels). Values represent mean ± SEM, n = 3; *p < 0.01; one-way ANOVA. Asterisk (*) and arrows in reporter diagrams denote stop codons and RT-PCR primers, respectively.

(E) A diagram of the 3′ region of the *L1CAM* gene. Asterisk (*) denotes stop codon. Arrows indicate RT-PCR primers.

(F) RT-PCR was performed on WT (+/+) and *NMF291*$^{-/-}$ (−/−) cerebellar cDNA at indicated ages.

(G and H) HEK293T cells were transfected with *L1CAM* exon 27-intron 27-exon 28 (G) and exon 28-intron 28-exon 29 (H) splicing reporters with or without WT or ΔU2 constructs as indicated. Splicing of these reporters was analyzed as described above in (C) and (D). As references, the spliced RT-PCR products of exon 27-intron 27-exon 28 reporter and the unspliced PCR product amplified from the exon 28-intron 28-exon 29 reporter plasmid (DNA) are also shown in (H). Values represent mean ± SEM, n = 3; *p < 0.01; one-way ANOVA. Asterisks (*) in reporter diagrams denote stop codons.

by expression of the mutant U2 construct, expression of the mutant U2 did not significantly affect splicing of the ISS− reporter. These results suggest that alterations in splicing efficiency mediated by the expression of the mutant U2 snRNA may be dependent on the presence of splicing regulatory sequences.

The presence of intronic or exonic splicing regulatory sequences often accompanies alternative splicing of pre-mRNA (Black, 2003); thus, we initially analyzed several alternative-splicing events that were previously reported to occur in the human cerebellum (Wang et al., 2008). Of the 20 alternative splicing events, including 1 in the neural cell adhesion molecule L1 (*L1CAM*), 4 displayed obvious changes in relative isoform expression between the WT and *NMF291*$^{-/-}$ cerebellum (data not shown). PCR amplification of the distal exons of the *L1CAM* transcript from WT cerebellar RNA generated two isoforms: the major form containing exons 27-28-29, and a minor isoform that retains the 95 bp intron located between exons 27 and 28 (Figures 6E and 6F). Coincident with the decrease of the fully spliced isoform, the abundance of the intron 27-containing isoform was increased in mutant cerebellar RNA. Interestingly, these alterations in splicing were most dramatic in the P30 and P40 cerebellum, demonstrating that the change in the ratio of splicing variants was temporally regulated in a manner coincident with expression of the mutant U2 snRNA.

To directly evaluate the effects of the mutant U2 on splicing of intron 27, we generated *L1CAM* splicing reporters. A cassette containing exon 27, the alternatively spliced intron 27, and exon 28, or a cassette with exon 28, the constitutively spliced intron 28, and exon 29 were cloned into the pBPLUGA plasmid (Figures 6G and 6H). These plasmids were cotransfected into HEK293T cells with the WT or mutant *Rnu2-8* plasmid. Transfection of the intron 27-containing reporter resulted in both spliced and unspliced transcripts as evidenced by RT-PCR (Figure 6G). In contrast only spliced transcripts were observed in cells transfected with the intron 28-containing reporter, and luciferase/β-galactosidase activity was increased accordingly (Figure 6H). Overexpression of the WT U2 had no effect on splicing of either reporter. However, in agreement with our in vivo data, expression of mutant *Rnu2-8* caused a decrease in splicing efficiency (34%; $p < 0.01$) of intron 27, but not of intron 28, the splicing efficiency of which was increased for unknown reasons (Figures 6G and 6H). These reporter data confirm that expression of the mutant U2 disrupts splicing of select introns.

Deletion of the U2/U6 Helix IA Linker Is Sufficient to Disrupt Splicing

The 5 nt deletion in *Rnu2-8* removes 2 nt of the BSRS, which recognizes and forms a duplex with the intronic branch site (BS) of the pre-mRNA that is important for the spliceosome assembly and the first catalytic step of splicing (Wahl et al., 2009). In addition, the *NMF291* deletion removes the 3 nt linker between the BSRS and the sequence that forms the U2/U6 helix IA. The distance between these two sequences has been shown to change splicing kinetics in yeast (McGrail et al., 2006; Ryan and Abelson, 2002; Smith et al., 2009). To further understand the underlying mechanism of mutant *Rnu2-8*-induced splicing defects, we created a series of U2 deletion plasmids: Δ6, in which the entire BSRS was deleted; Δ3, in which the linker sequence between BSRS and U2/U6 helix IA was deleted; and Δ9, in which both the entire BSRS and the linker were deleted (Figure 6A).

Experiments in yeast demonstrated that mutations in U2 snRNA, which disrupt the duplex formation between the BSRS and the BS, inhibit spliceosome assembly and result in the degradation of these RNAs (Smith et al., 2009). In agreement with these studies, we consistently observed lower expression levels of Δ6 and Δ9 *Rnu2-8* RNAs, both of which lack the BSRS, compared to that observed for the WT, Δ5 (the *NMF291* mutant form), and Δ3 *Rnu2-8* RNAs in transfected cells (Figure 6B). Cotransfection of the Δ6 or the Δ9 plasmid with the ISS+ reporter did not affect reporter splicing (Figure 6C). However, expression of the Δ3 construct significantly decreased (24%; $p < 0.01$) splicing of the ISS+ reporter, closely mimicking the repression of splicing that was observed when Δ5 *Rnu2-8* was cotransfected with the reporter. Also as observed with cotransfection of Δ5 *Rnu2-8*, expression of Δ3 construct had no effect on splicing of ISS− splicing reporter (Figure 6D).

Similarly, expression of the Δ3 *Rnu2-8* plasmid was sufficient to reduce splicing (13%; $p < 0.01$) of intron 27 from the *L1CAM* intron 27-containing splicing reporter, although not as efficiently as cotransfection of the reporter with Δ5 *Rnu2-8*, suggesting that the deletion of 2 nt of the BSRS may also contribute to the Δ5 effect on splicing (Figure 6G). Cotransfection of the Δ3 plasmid with the intron 28-containing reporter again led to an increase rather than decrease of splicing, as did expression of the Δ6 and Δ9 plasmids (Figure 6H). Our data suggest that expression of a U2 snRNA with either the *NMF291*-associated 5 nt deletion or lacking the linker sequence between the BSRS and the U2/U6 helix IA disrupts select intron splicing.

Abnormal Alternative Splicing in the *NMF291* Mutant Cerebellum

To analyze alternative splicing in the *NMF291* mutant cerebellum, exon expression was examined by Affymetrix mouse exon 1.0 ST microarrays. Microarrays were hybridized with RNA from three WT and three *NMF291*$^{-/-}$ cerebella isolated at P30, a time when the mutant U2 RNA is expressed at peak levels, but few neurons have degenerated (Figures S1A–S1D, 3E, and S3E). A total of 123 genes were differentially expressed between the WT and mutant cerebellum, as demonstrated by analysis of signal across all probe clusters for a gene (fold change ≥ 1.5; $p < 0.05$) (Table S1A). Differential expression of most (78%) of these genes was relatively low (1.5- to 2-fold), suggesting that overall gene expression was not dramatically altered in the P30 mutant cerebellum.

Paired analysis of the exon splicing index (SI), which was calculated by normalizing exon expression to gene level expression (Clark et al., 2007; de la Grange et al., 2010), revealed that the expression of 206 exons in 178 genes was differentially expressed between the WT and mutant cerebellum (SI fold change ≥ 1.5; $p < 0.05$) (Table S1B). These exons were compared to the comprehensive list of known human and mouse splice variants in the FAST DB database (de la Grange et al., 2007), and 146 (71%) events, representing all major types of alternative splicing patterns, were previously annotated as alternatively spliced

(Table S1B; Figure 7A). To validate our exon array results, RT-PCR was performed using cerebellar cDNA from four independent mice of each genotype. Of these events, 92% (12 of 13) were validated as differentially spliced between the WT and mutant cerebellum (Figure S6A; data not shown).

Interestingly, 14% of the differentially spliced events detected by exon array analysis were annotated as alternatively spliced introns, although introns normally represent a very minor (1%–3%) class of alternative splicing events (Chacko and Ranganathan, 2009; de la Grange et al., 2010; Wang et al., 2008). To examine this more closely and to expand our exon array results, we performed RNA-Seq analysis. Libraries were prepared from cerebellar mRNA from three P30 mutant and two P30 WT mice and sequenced. The resulting reads were aligned to the mouse genome reference sequence via SpliceMap (http://www.stanford.edu/group/wonglab/SpliceMap/), an algorithm that maps exon-exon junctions without relying on previous exon annotations for recovering the splicing junctions (Au et al., 2010). A total of $53.48 \pm 6.35 \times 10^6$ reads per sample were uniquely mapped to the mouse genome, and 61.23% ± 1.18%, 20.80% ± 1.54%, and 6.20% ± 0.19% of these reads uniquely mapped to exons, introns, and splice junctions, respectively (Table S1C).

To identify alternative splicing pattern changes between the WT and *NMF291*$^{-/-}$ cerebellum, splicing junction reads were extracted and normalized for isoform expression to generate the Relative Junction Index (RJI) (Figure S6). Comparison of the RJI between the two genotypes identified 1,636 junctions that were differentially expressed (RJI ratio ≥ 2.0; $p < 0.05$; Table S1D). In addition, 52 and 1,137 junction reads that were present only in the WT and mutant data sets, respectively, indicated that many splicing variants in the mutant cerebellum were not present, or present at a very low levels, in the WT cerebellum (Table S1E). As described above, RT-PCR using WT and mutant cerebellar cDNA was performed to test differential splicing of junctions. A total of 20 of 20 junctions that were originally identified in both genotypes and 20 of 21 (95%) of the junctions identified only in 1 genotype were validated (Figures S6B and S6C; data not shown).

To examine global abnormalities in splicing of introns in the mutant cerebellum, we calculated the Relative Intron retention Index (RII) from our WT and mutant RNA-Seq data sets (Figure S6). Comparison of WT and mutant RIIs indicated that 3,978 introns were retained at higher levels in the mutant cerebellum (RII ratio ≥ 2; $p < 0.05$, Figure 7B; Table S1F), including intron 27 of *L1CAM* (RII ratio = 3.55; $p = 0.0012$). In contrast, we identified only 362 introns that were retained at higher levels in the WT cerebellum (RII ratio ≥ 2; $p < 0.05$). To check the validity of our analysis, we performed RT-PCR on 23 introns that were present at higher levels in the mutant transcriptome by RNA-Seq, and all were validated (Figures S6D and S6E; data not shown). Furthermore, 19 of 23 (82.61%) of these introns, like intron 27 of *LICAM*, and 5 of 7 RT-PCR-validated introns identified by exon array, were also present in WT cerebellum as a minor isoform (Figures S6A and S6D). These results indicate that these introns represent alternative splicing events and are likely to be suboptimal pre-mRNA substrates even in presence of the WT spliceosome. Previous studies have shown that small introns are prone to being retained in human and mouse transcripts in physiological conditions (Sakabe and de Souza, 2007). These prompted us to check the size distribution of the intron retention events identified by RNA-Seq. Indeed, 30.62% of the retained introns in the mutant cerebellum were less than 100 bp, which largely differs from the size distribution of introns in the mouse genome (RefSeq; 5.31% < 100 bp) or those significantly retained in the WT cerebellum (3.31% < 100 bp) (Figure 7C). As expected, differences in splicing of small introns removed by the U12-dependent minor spliceosome were not observed in the mutant cerebellum (Figure S6F). Thus, both exon array and RNA-Seq analysis demonstrated that a group of alternative splicing events, including the splicing of small introns, was altered in the *NMF291*$^{-/-}$ cerebellum.

To check the overlap of our exon array and RNA-Seq analysis, we compared intron retention events (Table S1H). Of these events, 96.4% (27 of 28) detected by exon array displayed differences in the same direction in RNA-Seq data, although only 46.4% (13 of 28) passed our stringent threshold set for RNA-Seq analysis. Although differential events in other splicing event categories ascertained by both analyses were clearly validated by RT-PCR, little overlap was observed in the data sets, likely due to the different experimental and analysis parameters used in the two methods (see Extended Experimental Procedures).

The role of U2 snRNA as a basal component of the spliceosome would predict that splicing of transcripts encoding proteins across many functional classes would be disrupted in the mutant cerebellum. Indeed, splicing alterations between the WT and mutant cerebellum occur in genes with many predicted cellular roles (Tables S1B and S1D–S1F). However, Gene Ontology (GO) analysis of the differentially expressed junctions and spliced introns detected by RNA-Seq and exon array analysis revealed that genes annotated to GO terms of nucleoplasm (GO:0005654) were significantly enriched, as were those annotated to ribonucleotide binding (GO:0032553) (Table S1G). Interestingly, after these two functional clusters, the most significantly enriched genes in the differentially spliced intron data set were annotated to mRNA processing (GO:0006397), including those annotated to the spliceosomal complex (GO:0005681) (Figure 7D; Table S1G). Differentially expressed exons and genes also showed significant enrichment for mRNA processing, although at higher p values.

DISCUSSION

We demonstrate that a mutation in one of the multicopy mouse U2 snRNA genes causes defects in pre-mRNA splicing, leading to neurodegeneration. U2 snRNAs play an essential role in formation of the catalytically active spliceosome by base pairing with both the intron branch point and the U6 snRNA (Wahl et al., 2009). Expression of the mutant U2 snRNA alters pre-mRNA splicing at selective splice sites that are often associated with alternative splicing, demonstrating that U-snRNA dysfunction, like downregulation of core spliceosomal proteins, can influence splice site choice (Corioni et al., 2011; Park et al., 2004; Saltzman et al., 2011; Shaw et al., 2007).

One of the main pathological features of the *NMF291*$^{-/-}$ cerebellum is the increased retention of small introns, which likely

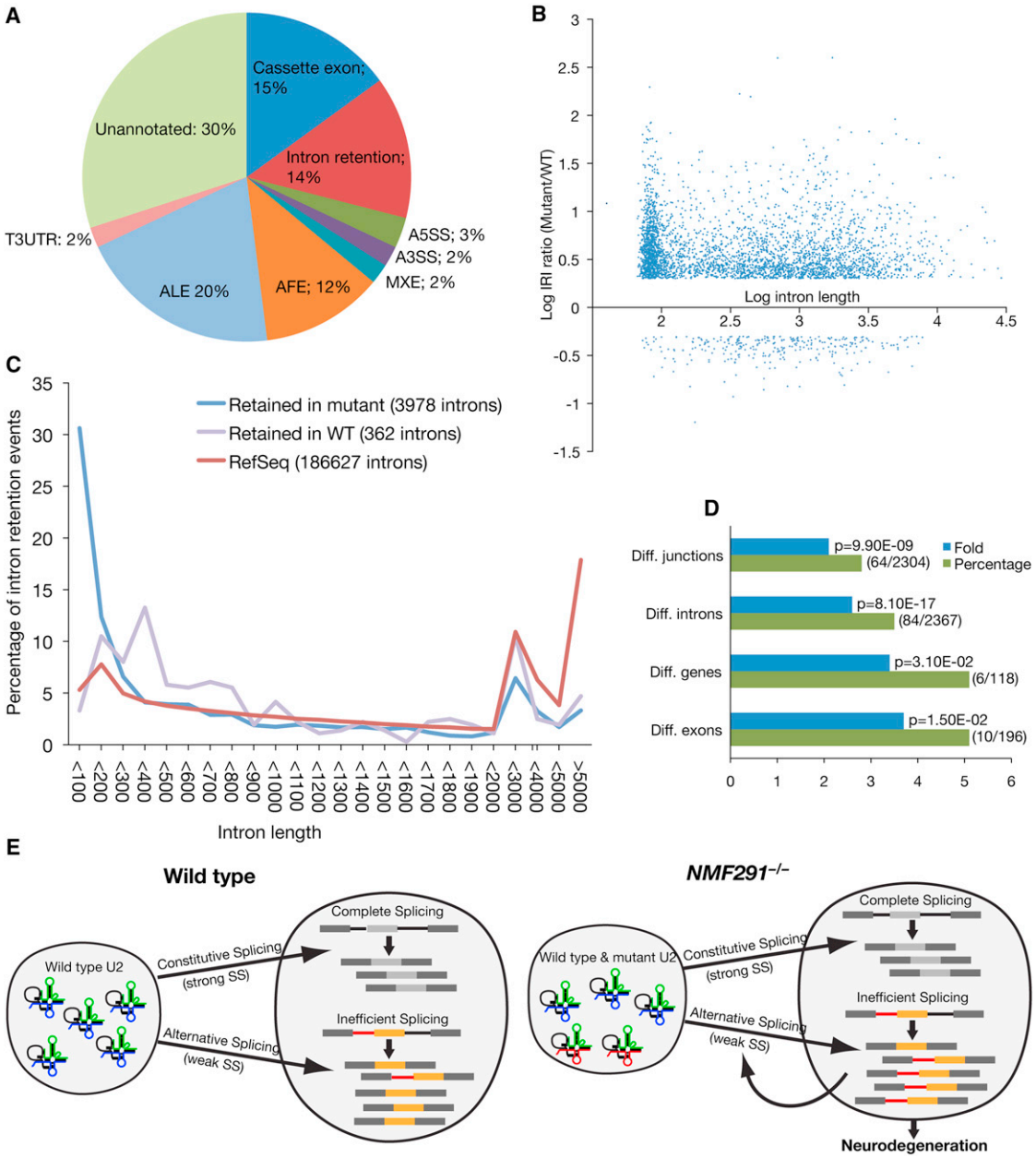

Figure 7. Global Splicing Abnormalities in the *NMF291*$^{-/-}$ Cerebellum

(A) Types of alternative splicing events identified by exon array analysis as differentially spliced between the WT and the *NMF291*$^{-/-}$ cerebellum. A3SS, alternative 3′ splice site; A5SS, alternative 5′ splice site; AFE, alternative first exon; ALE, alternative last exon; MXE, mutually exclusive exon; T3UTR, truncated 3′UTR.

(B) The log of the mutant/WT IRI generated by RNA-Seq analysis plotted against the log of the intron length (bp).

(C) Significantly retained introns in the cerebellum of *NMF291*$^{-/-}$ or WT mice, or RefSeq introns were grouped by length and plotted as a percentage of the total introns.

(D) GO analysis of genes annotated to the pre-mRNA splicing GO term were significantly enriched in the differentially spliced exons (Diff. junctions) and introns (Diff. introns) identified by RNA-Seq, and differentially spliced exons (Diff. exons) and differentially expressed genes (Diff. genes) identified by exon array. Percentage is the number of genes (the numerator in parentheses) annotated to the GO term divided by the total number of inputted genes (the denominator in parentheses). Fold enrichment is the magnitude of enrichment of input genes relative to all mouse genes annotated to pre-mRNA splicing. The p value indicates the significance of gene-term enrichment with a modified Fisher's exact test.

(E) The working model for our findings. The splicing status and biological consequences of expression of WT (blue) and *NMF291* mutant (red) U2 snRNAs in WT and *NMF291*$^{-/-}$ neurons are shown. Our in vivo and in vitro data suggest that expression of mutant U2 snRNA disrupts splicing at many suboptimal or weaker splice sites, including some of those used in alternative splicing. These changes in alternative splicing may be further amplified by altered splicing of RNA-processing factors caused directly by mutant U2 snRNAs or by autoregulation.

See also Figure S6 and Tables S1A–S1H.

represent unique spliceosomal substrates. Unlike splicing of large introns, which is thought to first occur by pairing of splice sites across the exon ("exon definition"), splicing of short introns likely occurs by pairing of 5′ and 3′ splice sites across the intron ("intron definition") (Berget, 1995). Furthermore, even under normal physiological conditions, many of the highly retained introns in the mutant cerebellum are not fully spliced, consistent with the observation that weak splicing sites often flank small introns (Lim and Burge, 2001; Sakabe and de Souza, 2007). Given the disruption of short intron splicing and other alternative splicing events, it is plausible that mutant U2 snRNPs are fully functional on optimal, but not suboptimal, substrates (Figure 7E).

Interestingly, we found that mRNA-processing genes were significantly enriched among the alternative splicing events differentially expressed between the WT and mutant cerebellum, suggesting that neurons may utilize alternative splicing to regulate the function of proteins involved in RNA splicing and processing in an effort to restore splicing homeostasis. Indeed, studies have shown that a number of splicing regulators autoregulate their expression and activity via transcriptional feedback loops and alternative splicing (Ni et al., 2007; Saltzman et al., 2011; Wollerton et al., 2004). However, rather than reestablishing homeostasis, these splicing alterations could in fact act to amplify the amount of abnormal splicing and ultimately prove deleterious. It will be intriguing to see whether the expression level and/or alternative splicing status of these mRNA-processing genes is also affected in SMA patients or ALS/FTD patients with mutations in *TDP-43* or *FUS/TLS*.

The ultimate cause of neuron death in the mutant cerebellum is unclear. Cell death could be caused by the generation of proteins with altered function or by the production of RNAs containing abnormal sequences, which could themselves be toxic as previously reported for trinucleotide repeat expansion diseases (Li et al., 2008). Retained introns may also contribute to neuron death by sequestering splicing regulators and/or other RNA binding proteins. In addition, many of these introns likely harbor premature translation termination codons (PTCs) that would be predicted to trigger the nonsense-mediated mRNA-decay (NMD) pathway. In addition to its role in degradation of abnormal transcripts, NMD also regulates many natural PTC-containing transcripts, including those involved in synaptic physiology and cellular stress (Gardner, 2010; Giorgi et al., 2007). Enhanced and/or prolonged NMD activation could overwhelm the NMD pathway, causing dysregulation of natural NMD targets that might be essential for cell survival, or itself cause cellular stress.

Finally, our data demonstrate the potential for disease-causing mutations in multicopy genes. Although a single U2 gene is present in yeast, multiple copies of these genes exist in higher organisms, each producing identical or nearly identical products. Indeed, the region on human Chromosome 17p21 (homologous to the *Rnu2-6* to *Rnu2-10*-containing region on mouse Chromosome 11) also contains a cluster of stably inherited U2 genes that vary in copy number from 5 to 25 (Van Arsdell and Weiner, 1984; Westin et al., 1984). In addition to our findings of temporal and spatial regulation of a mouse U2 gene, developmental regulation of other snRNA genes, including U2 snRNA genes, has been reported (Forbes et al., 1984; Lund et al., 1985; Sierra-Montes et al., 2005; Stefanovic et al., 1991). Furthermore, the developmental arrest associated with homozygosity for a mutation in 1 of 12 *C. elegans* U1 genes raises the possibility of differences in expression and/or function between *C. elegans* U1 genes (Zahler et al., 2004). Whether individual human U2s (or other multicopy genes) are differentially expressed during development, in different cell types, or even as a result of pathogenic processes is unknown. However, the potential for discrete regulation of individual members of multigene families, combined with their potential for copy number variation, increases the prospect of uncovering disease-causing mutations in repetitive genes.

EXPERIMENTAL PROCEDURES

Mice

The *NMF291* mutant strain was derived from EMS-treated ES cells and a two-generation mating scheme, as described previously (Munroe and Schimenti, 2009). Genetic mapping of the *NMF291* mutation was performed using an intersubspecific intercross (B6; 129 *NMF291* × CAST/Ei). The Jackson Laboratory Animal Care and Use Committee approved all animal protocols.

Histology Analysis

Hematoxylin and eosin staining was performed on Bouin's fixed tissue. Cleaved Caspase-3 (Cell Signaling) immunostaining and TUNEL assays (Roche) were performed as described previously (Zhao et al., 2005). At least three mice of each genotype were used for all histological analyses.

RPA, Northern Blot Assay, and RT-PCR Assay

Total RNA was extracted by TRIzol (Invitrogen) and treated with DNase I (Ambion). RPA analysis was performed as suggested by the manufacturer's instructions (Ambion). For northern blots, total RNA was separated by 10% denaturing polyacrylamide gel, and the membrane was hybridized with end-labeled DNA oligo probes. RT-PCR was performed on random-primed cDNA (Invitrogen). Primers used for RT-PCR are described in Table S2. Density of bands in scanned X-ray films was determined by ImageQuant 5.2 software (Amersham).

Constructs, Cell Culture, Transfection, and Luciferase Assays

The mutant *Rnu2-8* DNA fragment used for generating transgenic mice and the corresponding WT DNA fragment were cloned into pCR2.1-TOPO for expression of WT and mutant U2 snRNA in cultured cells. The Δ3, Δ6, and Δ9 U2 snRNA and ISS− expression constructs were generated by site-directed mutagenesis (Stratagene). Primers used for construct generation are described in Table S2B. HEK293T cells were used for transient transfection (Lipofectamine 2000; Invitrogen). Luciferase and β-galactosidase activities (Promega) were measured in a multilabel counter 48 hr after transfection. Statistical significance was determined by ANOVA analysis (SPSS).

Exon Array, RNA-Seq, and Functional GO Analysis

Data treatment of Mouse Exon 1.0 ST Arrays (Affymetrix) was done by the EASANA analysis and the interface visualization system (GenoSplice Technology, http://www.genosplice.com), which is based on the FAST DB annotations (de la Grange et al., 2007). Probe selection and statistical analysis were preformed as previously described (Clark et al., 2007; de la Grange et al., 2010). The GEO (Gene Expression Omnibus) accession number for our exon array data is GSE33069. For RNA-Seq, mRNA purification and DNA library preparation were performed according to the manufacturer's protocol (Illumina). The library was sequenced on Illumina GAIIX using paired-end read strategy. For de novo identification of junctions, the reads were inputted to SpliceMap 3.3.6 (Au et al., 2010) and aligned to the mouse reference genome. A workflow chart of our RNA-Seq analysis is shown in Figure S6G. RefSeq intron length information was extracted from UCSC. The GO analysis was conducted by using DAVID bioinformatics resources 6.7 (Huang da et al., 2009). Primers

used for exon array and RNA-Seq validation experiments are described in Table S2C.

ACCESSION NUMBERS

Our exon array data have been deposited into the GEO. The GEO accession number is GSE33069. The databank accession numbers for the *Rnu2-6*, *Rnu2-7*, *Rnu2-8*, *Rnu2-9*, and *Rnu2-10* sequences reported in this paper are JN863957, JN863958, JN863956, JN863959, and JN863960, respectively.

SUPPLEMENTAL INFORMATION

Supplemental Information includes Extended Experimental Procedures, six figures, two tables, and one movie and can be found with this article online at doi:10.1016/j.cell.2011.11.057.

ACKNOWLEDGMENTS

We thank The Jackson Laboratory sequencing, gene expression, histology, microinjection, and multimedia services for their assistance. We also thank W.H. Wong for discussions on RNA-Seq analysis, J. Blake and C. Bult for discussion on GO analysis, L. Beverly-Staggs and J. Cook for mouse husbandry assistance, P. de la Grange for exon array analysis, J. Hammer and L. Zhao for graphics assistance, J. McCarthy and M. Nasim for plasmids, and R. Burgess, G. Cox, and M. Hibbs for comments on the manuscript. This work was partially supported by an institutional National Cancer Institute core grant (JAX), and the work of J.C.M. was partially supported by NIH Grants R01HG004634 and R01HG005717. S.L.A. is an investigator of the Howard Hughes Medical Institute.

Received: April 26, 2011
Revised: August 6, 2011
Accepted: November 8, 2011
Published: January 19, 2012

REFERENCES

Au, K.F., Jiang, H., Lin, L., Xing, Y., and Wong, W.H. (2010). Detection of splice junctions from paired-end RNA-seq data by SpliceMap. Nucleic Acids Res. *38*, 4570–4578.

Berget, S.M. (1995). Exon recognition in vertebrate splicing. J. Biol. Chem. *270*, 2411–2414.

Black, D.L. (2003). Mechanisms of alternative pre-messenger RNA splicing. Annu. Rev. Biochem. *72*, 291–336.

Bult, C., Kibbe, W.A., Snoddy, J., Vitaterna, M., Swanson, D., Pretel, S., Li, Y., Hohman, M.M., Rinchik, E., Takahashi, J.S., et al. (2004). A genome end-game: understanding gene function in the nervous system. Nat. Neurosci. *7*, 484–485.

Chacko, E., and Ranganathan, S. (2009). Comprehensive splicing graph analysis of alternative splicing patterns in chicken, compared to human and mouse. BMC Genomics *10* (*Suppl 1*), S5.

Clark, T.A., Schweitzer, A.C., Chen, T.X., Staples, M.K., Lu, G., Wang, H., Williams, A., and Blume, J.E. (2007). Discovery of tissue-specific exons using comprehensive human exon microarrays. Genome Biol. *8*, R64.

Cooper, T.A., Wan, L., and Dreyfuss, G. (2009). RNA and disease. Cell *136*, 777–793.

Corioni, M., Antih, N., Tanackovic, G., Zavolan, M., and Krämer, A. (2011). Analysis of in situ pre-mRNA targets of human splicing factor SF1 reveals a function in alternative splicing. Nucleic Acids Res. *39*, 1868–1879.

de la Grange, P., Dutertre, M., Correa, M., and Auboeuf, D. (2007). A new advance in alternative splicing databases: from catalogue to detailed analysis of regulation of expression and function of human alternative splicing variants. BMC Bioinformatics *8*, 180.

de la Grange, P., Gratadou, L., Delord, M., Dutertre, M., and Auboeuf, D. (2010). Splicing factor and exon profiling across human tissues. Nucleic Acids Res. *38*, 2825–2838.

Edery, P., Marcaillou, C., Sahbatou, M., Labalme, A., Chastang, J., Touraine, R., Tubacher, E., Senni, F., Bober, M.B., Nampoothiri, S., et al. (2011). Association of TALS developmental disorder with defect in minor splicing component U4atac snRNA. Science *332*, 240–243.

Egloff, S., O'Reilly, D., and Murphy, S. (2008). Expression of human snRNA genes from beginning to end. Biochem. Soc. Trans. *36*, 590–594.

Forbes, D.J., Kirschner, M.W., Caput, D., Dahlberg, J.E., and Lund, E. (1984). Differential expression of multiple U1 small nuclear RNAs in oocytes and embryos of Xenopus laevis. Cell *38*, 681–689.

Gardner, L.B. (2010). Nonsense-mediated RNA decay regulation by cellular stress: implications for tumorigenesis. Mol. Cancer Res. *8*, 295–308.

Giorgi, C., Yeo, G.W., Stone, M.E., Katz, D.B., Burge, C., Turrigiano, G., and Moore, M.J. (2007). The EJC factor eIF4AIII modulates synaptic strength and neuronal protein expression. Cell *130*, 179–191.

He, H., Liyanarachchi, S., Akagi, K., Nagy, R., Li, J., Dietrich, R.C., Li, W., Sebastian, N., Wen, B., Xin, B., et al. (2011). Mutations in U4atac snRNA, a component of the minor spliceosome, in the developmental disorder MOPD I. Science *332*, 238–240.

Hernandez, N. (2001). Small nuclear RNA genes: a model system to study fundamental mechanisms of transcription. J. Biol. Chem. *276*, 26733–26736.

Huang da, W., Sherman, B.T., and Lempicki, R.A. (2009). Systematic and integrative analysis of large gene lists using DAVID bioinformatics resources. Nat. Protoc. *4*, 44–57.

Kollmus, H., Flohé, L., and McCarthy, J.E. (1996). Analysis of eukaryotic mRNA structures directing cotranslational incorporation of selenocysteine. Nucleic Acids Res. *24*, 1195–1201.

Lagier-Tourenne, C., Polymenidou, M., and Cleveland, D.W. (2010). TDP-43 and FUS/TLS: emerging roles in RNA processing and neurodegeneration. Hum. Mol. Genet. *19*(R1), R46–R64.

Lefebvre, S., Bürglen, L., Reboullet, S., Clermont, O., Burlet, P., Viollet, L., Benichou, B., Cruaud, C., Millasseau, P., Zeviani, M., et al. (1995). Identification and characterization of a spinal muscular atrophy-determining gene. Cell *80*, 155–165.

Lemmens, R., Moore, M.J., Al-Chalabi, A., Brown, R.H., Jr., and Robberecht, W. (2010). RNA metabolism and the pathogenesis of motor neuron diseases. Trends Neurosci. *33*, 249–258.

Lerner, E.A., Lerner, M.R., Janeway, C.A., Jr., and Steitz, J.A. (1981). Monoclonal antibodies to nucleic acid-containing cellular constituents: probes for molecular biology and autoimmune disease. Proc. Natl. Acad. Sci. USA *78*, 2737–2741.

Li, L.B., Yu, Z., Teng, X., and Bonini, N.M. (2008). RNA toxicity is a component of ataxin-3 degeneration in Drosophila. Nature *453*, 1107–1111.

Licatalosi, D.D., and Darnell, R.B. (2006). Splicing regulation in neurologic disease. Neuron *52*, 93–101.

Lim, L.P., and Burge, C.B. (2001). A computational analysis of sequence features involved in recognition of short introns. Proc. Natl. Acad. Sci. USA *98*, 11193–11198.

Lund, E., Kahan, B., and Dahlberg, J.E. (1985). Differential control of U1 small nuclear RNA expression during mouse development. Science *229*, 1271–1274.

Manser, T., and Gesteland, R.F. (1982). Human U1 loci: genes for human U1 RNA have dramatically similar genomic environments. Cell *29*, 257–264.

Marz, M., Kirsten, T., and Stadler, P.F. (2008). Evolution of spliceosomal snRNA genes in metazoan animals. J. Mol. Evol. *67*, 594–607.

McGrail, J.C., Tatum, E.M., and O'Keefe, R.T. (2006). Mutation in the U2 snRNA influences exon interactions of U5 snRNA loop 1 during pre-mRNA splicing. EMBO J. *25*, 3813–3822.

Mordes, D., Luo, X., Kar, A., Kuo, D., Xu, L., Fushimi, K., Yu, G., Sternberg, P., Jr., and Wu, J.Y. (2006). Pre-mRNA splicing and retinitis pigmentosa. Mol. Vis. *12*, 1259–1271.

Munroe, R., and Schimenti, J. (2009). Mutagenesis of mouse embryonic stem cells with ethylmethanesulfonate. Methods Mol. Biol. *530*, 131–138.

Nasim, M.T., Chowdhury, H.M., and Eperon, I.C. (2002). A double reporter assay for detecting changes in the ratio of spliced and unspliced mRNA in mammalian cells. Nucleic Acids Res. *30*, e109.

Ni, J.Z., Grate, L., Donohue, J.P., Preston, C., Nobida, N., O'Brien, G., Shiue, L., Clark, T.A., Blume, J.E., and Ares, M., Jr. (2007). Ultraconserved elements are associated with homeostatic control of splicing regulators by alternative splicing and nonsense-mediated decay. Genes Dev. *21*, 708–718.

Park, J.W., Parisky, K., Celotto, A.M., Reenan, R.A., and Graveley, B.R. (2004). Identification of alternative splicing regulators by RNA interference in Drosophila. Proc. Natl. Acad. Sci. USA *101*, 15974–15979.

Pavelitz, T., Rusché, L., Matera, A.G., Scharf, J.M., and Weiner, A.M. (1995). Concerted evolution of the tandem array encoding primate U2 snRNA occurs in situ, without changing the cytological context of the RNU2 locus. EMBO J. *14*, 169–177.

Polymenidou, M., Lagier-Tourenne, C., Hutt, K.R., Huelga, S.C., Moran, J., Liang, T.Y., Ling, S.C., Sun, E., Wancewicz, E., Mazur, C., et al. (2011). Long pre-mRNA depletion and RNA missplicing contribute to neuronal vulnerability from loss of TDP-43. Nat. Neurosci. *14*, 459–468.

Ryan, D.E., and Abelson, J. (2002). The conserved central domain of yeast U6 snRNA: importance of U2-U6 helix Ia in spliceosome assembly. RNA *8*, 997–1010.

Sakabe, N.J., and de Souza, S.J. (2007). Sequence features responsible for intron retention in human. BMC Genomics *8*, 59.

Saltzman, A.L., Pan, Q., and Blencowe, B.J. (2011). Regulation of alternative splicing by the core spliceosomal machinery. Genes Dev. *25*, 373–384.

Sauterer, R.A., Feeney, R.J., and Zieve, G.W. (1988). Cytoplasmic assembly of snRNP particles from stored proteins and newly transcribed snRNA's in L929 mouse fibroblasts. Exp. Cell Res. *176*, 344–359.

Shaw, S.D., Chakrabarti, S., Ghosh, G., and Krainer, A.R. (2007). Deletion of the N-terminus of SF2/ASF permits RS-domain-independent pre-mRNA splicing. PLoS One *2*, e854.

Sierra-Montes, J.M., Pereira-Simon, S., Smail, S.S., and Herrera, R.J. (2005). The silk moth Bombyx mori U1 and U2 snRNA variants are differentially expressed. Gene *352*, 127–136.

Smith, D.J., Konarska, M.M., and Query, C.C. (2009). Insights into branch nucleophile positioning and activation from an orthogonal pre-mRNA splicing system in yeast. Mol. Cell *34*, 333–343.

Stefanovic, B., Li, J.M., Sakallah, S., and Marzluff, W.F. (1991). Isolation and characterization of developmentally regulated sea urchin U2 snRNA genes. Dev. Biol. *148*, 284–294.

Tollervey, J.R., Curk, T., Rogelj, B., Briese, M., Cereda, M., Kayikci, M., König, J., Hortobágyi, T., Nishimura, A.L., Zupunski, V., et al. (2011). Characterizing the RNA targets and position-dependent splicing regulation by TDP-43. Nat. Neurosci. *14*, 452–458.

Van Arsdell, S.W., and Weiner, A.M. (1984). Human genes for U2 small nuclear RNA are tandemly repeated. Mol. Cell. Biol. *4*, 492–499.

Wahl, M.C., Will, C.L., and Lührmann, R. (2009). The spliceosome: design principles of a dynamic RNP machine. Cell *136*, 701–718.

Wang, E.T., Sandberg, R., Luo, S., Khrebtukova, I., Zhang, L., Mayr, C., Kingsmore, S.F., Schroth, G.P., and Burge, C.B. (2008). Alternative isoform regulation in human tissue transcriptomes. Nature *456*, 470–476.

Westin, G., Zabielski, J., Hammarström, K., Monstein, H.J., Bark, C., and Pettersson, U. (1984). Clustered genes for human U2 RNA. Proc. Natl. Acad. Sci. USA *81*, 3811–3815.

Wollerton, M.C., Gooding, C., Wagner, E.J., Garcia-Blanco, M.A., and Smith, C.W. (2004). Autoregulation of polypyrimidine tract binding protein by alternative splicing leading to nonsense-mediated decay. Mol. Cell *13*, 91–100.

Zahler, A.M., Tuttle, J.D., and Chisholm, A.D. (2004). Genetic suppression of intronic +1G mutations by compensatory U1 snRNA changes in *Caenorhabditis elegans*. Genetics *167*, 1689–1696.

Zhang, Z., Lotti, F., Dittmar, K., Younis, I., Wan, L., Kasim, M., and Dreyfuss, G. (2008). SMN deficiency causes tissue-specific perturbations in the repertoire of snRNAs and widespread defects in splicing. Cell *133*, 585–600.

Zhao, L., Longo-Guess, C., Harris, B.S., Lee, J.W., and Ackerman, S.L. (2005). Protein accumulation and neurodegeneration in the woozy mutant mouse is caused by disruption of SIL1, a cochaperone of BiP. Nat. Genet. *37*, 974–979.

EXTENDED EXPERIMENTAL PROCEDURES

Mice

The *NMF291* mutant strain was derived from chimeric mice generated from 129S4/SvJae X C57BL/6J F1 ES cells treated with EMS (0.4 μg/ml) and used in a two-generation mating scheme as described (Munroe and Schimenti, 2009). To generate the mutant U2 snRNA transgenic mice, a DNA fragment containing the transcription unit of the mutant *Rnu2-8* and its upstream 780bp and downstream 569bp, was amplified by PCR from the *NMF291* homozygous genomic DNA (Forward, 5′-ctcttgcctagatgggcttg-3′; Reverse, 5′-tctctgcctctatggggttt-3′). The purified DNA fragment was microinjected into the pronuclei of C57BL/6J embryos and founders were identified using PCR. DNA sequencing of amplicons of this primer pair was performed to genotype *NMF291* mice. Genetic mapping of the *NMF291* mutation was performed using an intersubspecific intercross (B6; 129 NMF291 × CAST/Ei). The Jackson Laboratory Animal Care and Use Committee approved all animal protocols.

Histology, Immunohistochemistry, and TUNEL Assay

Mice were intracardically perfused with Bouin's fixative or 4% paraformaldehyde for histology and immunohistology, respectively. Brains were postfixed and embedded in paraffin. Cleaved Caspase-3 (Cell Signaling) immunostaining and TUNEL assays (Roche) were performed as described previously (Zhao et al., 2005).

Immunoprecipitation of snRNPs from Cerebellar Extracts

Frozen mouse cerebella were homogenized with 1ml of reconstitution buffer (20mM HEPES-KOH pH 7.9, 50mM KCl, 5mM $MgCl_2$, 0.2mM EDTA, 5% glycerol) containing 0.01% NP40 as previously described (Gabanella et al., 2007). Homogenates were then passed through a 25G needle five times and centrifuged 15 min at 10,000 rpm at 4°C. Supernatants were collected for IP experiments and protein concentration was measured. Five μg of either the Sm Antigen (Y12) antibody (Lab Vision) or mouse normal IgG (Santa Cruz Biotechnology) conjugated to Dynabeads Protein G (Invitrogen) were incubated with 400μg of cerebellar extracts added to RSB-500 buffer (500mM NaCl, 10mM Tris-HCl pH 7.4, 2.5mM $MgCl_2$) containing 0.1% NP40, protease inhibitor cocktail (Roche), and phosphatase inhibitors (50mM NaF, and 0.2mM Na_3VO_4) at 4°C for 8 hr. After five washes with the same buffer, bound RNAs were recovered from IP products by proteinase K treatment, phenol/chloroform extraction, and ethanol precipitation. Detection of total and mutant U2 snRNAs was performed by real-time PCR as described in Figure S3A.

RNase Protection, Northern Blot, and RT-PCR Assays

Total RNA was extracted from mouse tissues and HEK293 cells using TRIzol (Invitrogen) and treated with DNase I (Ambion). RT-PCR was performed on random-primed cDNA using primer sets described in Tables S2A–S2C. For the RPA probe, a DNA fragment covering nts 7-180 (174nts) of the *Rnu2-8* transcription unit (191nts) was cloned into pCR2.1-TOPO (Invitrogen). The ^{32}P-radiolabeled RNA probe was generated by in vitro transcription of the linearized plasmid and gel purified. RPA analysis was performed as suggested by the manufacturer's instructions (Ambion). Briefly, total RNA was hybridized with radiolabeled RNA probe at 42°C overnight. Non-hybridized RNA was digested by RNase A/T1, and the resulting protected RNA fragments were separated on a 10% denaturing polyacrylamide gel. Density of bands in the scanned X-ray films was determined by ImageQuant 5.2 software (Amersham). Statistical significance was determined by ANOVA and paired t- test (SPSS). For Northern blots, total RNA was also separated on a 10% denaturing polyacrylamide gel. The membrane was hybridized with ^{32}P-end-labeled DNA oligonucleotides corresponding to U2 snRNA (5′- tatcagatattaaactgataagaacagatact-3′) or 5 s rRNA (5′- cctgcttagcttccgagatca-3′).

Constructs and Mutagenesis

For expression of wild-type and mutant U2 snRNA in HEK293T cells, the mutant *Rnu2-8* DNA fragment used to generate transgenic mice and the corresponding wild-type fragment were cloned into pCR2.1-TOPO. The Δ3, Δ6, and Δ9 U2 snRNA expression constructs were generated from the wild-type U2 construct by site-directed mutagenesis (Stratagene). The ISS- (pTN23) reporter was generated from the ISS+ (pTN24) plasmid (Nasim et al., 2002) by deleting the 25bp ISS using the same mutagenesis method. The L1CAM exon27-intron27-exon28 and exon28-intron 28-exon29 cassettes were amplified from C57BL/6J genomic DNA and inserted in frame into pBPLUGA at the SalI and BamHI sites (Kollmus et al., 1996). Primers used for construct generation are described in the Table S2B.

Cell Culture, Transfection, and Luciferase Assays

HEK293T cells grown in DMEM medium containing 10% FBS, were used for transient transfection studies. Briefly, 3 × 10^5 cells/well were plated in a 12-well plate 24 hr before transfection with Lipofectamine 2000 (Invitrogen). 48 hr after transfection, cells were harvested in Passive Lysis Buffer (Promega). Luciferase and β-galactosidase activities were measured as per manufacturer's instructions (Promega) in a multilabel counter. Statistical significance was determined by ANOVA analysis (SPSS).

Functional GO Analysis

The gene lists of differentially expressed genes and exons identified by exon array, differentially expressed junctions found in one or both genotypes and retained introns identified by RNA-Seq, were uploaded into DAVID bioinformatics resources 6.7

(http://david.abcc.ncifcrf.gov/) (Huang da et al., 2009). The functional annotation chart and clustering analysis modules were employed for gene-term enrichment analysis.

Exon Array

Total RNA was isolated by TRIzolPlus (Invitrogen) and cDNA was synthesized, labeled and fragmented using the Affymetrix GeneChip WT Terminal Labeling kit. GeneChip® Mouse Exon 1.0 ST Arrays (Affymetrix) were hybridized with 2.3μg of biotin-labeled cDNA for 16 hr at 45°C. Post-hybridization staining and washing were performed according to manufacturer's protocols using the Fluidics Station 450 instrument (Affymetrix). Arrays were scanned with a GeneChipTM Scanner 3000 (Affymetrix) laser confocal slide scanner.

Affymetrix Expression Console Software was used for array quality assessment. Exon array data treatment was done by the EASANA® analysis system and interface visualization (GenoSplice Technology, http://www.genosplice.com), which is based on the FAST DB® annotations (de la Grange et al., 2007; de la Grange et al., 2005). Data were normalized by using quantile normalization method. Background correction was made using the anti-genomic probes. Probe selection was made as previously described (Clark et al., 2007; de la Grange et al., 2010). Briefly, only probes targeting exons annotated from full-length cDNA were kept for analysis. Among these pre-selected probes, bad quality probes (e.g., probes labeled as ''cross-hybridizing'' by Affymetrix) and probes with intensity signal too low compared to background probes with the same GC content were removed from analysis. Probes with a detection above background (DABG) p value ≤ 0.05 in at least half of chips were considered for further statistical analysis as previously described (Clark et al., 2007; de la Grange et al., 2010). Exon intensities were normalized to the overall intensity of the corresponding gene for each replicate to obtain the normalized exon intensities (NI). The NI of each exon was then compared to that of the other genotype to give the fold change or splicing index. Paired statistical analyses were performed on gene signal intensities and on the splicing index using a Student's paired t test. Results for both gene and exon levels were considered statistically significant at p values < 0.05 and fold-change ≥ 1.5. Note that statistical corrections for sample size were not used to compute p values, thus these values were only used for relative ranking purposes. Primers used for exon array validation are described in the Table S2C. The GEO (Gene Expression Omnibus) accession number for our exon array data is GSE33069.

RNA-Seq Methods

Purification of mRNA, double-stranded cDNA preparation and ligation of barcode-containing adaptors were performed using the mRNA-Seq Sample Prep kit according to the manufacturer's protocol (Illumina). Size selection (300bp) was performed by agarose gel electrophoresis, and PCR was performed to enrich the adaptor-modified DNA fragments. Validation of DNA fragment size was performed using an Agilent Technologies 2100 Bioanalyzer, and DNA concentration was determined by quantitative PCR, following the manufacturer's protocol (Kapa Biosystems). The DNA library was sequenced on an Illumina GAIIX using a 76nt paired-end read strategy following the manufacturer's protocol. The sequences were initially mapped to the mouse genome using CASAVA (Illumina) for assessment of sequence quality. The barcoded reads were separated allowing for 2 mismatches in the barcode tag, and analyzed for their base composition. Any bases at the start of the read deviating from an approximately uniform distribution were removed as they might represent adaptor sequence contamination. After pre-processing, one base was removed from the beginning of all the reads.

For de novo identification of junctions, the pre-processed reads were inputted to SpliceMap 3.3.6 (Au et al., 2010) and aligned to the mouse reference genome (mm9) (Figure S6G). For junctions found only in one genotype, the junctions where the median read number within a genotype was < 3 were filtered out. SpliceMap is not based on previous annotations and thus entire exons adjacent to junction reads were not readily defined. Furthermore the length of ~93.1% of exons in mouse genome is greater than 50bps (Sakharkar et al., 2005). Therefore, we recovered the RPKM (Mortazavi et al., 2008) value of 25bp, which is the minimal exon size SpliceMap 3.3.6 can utilize, upstream and downstream of the donor and acceptor sites of the junction. The larger RPKM value of the two sides was recorded to generate the maxRPKM_25 to represent the isoform expression level. Any junctions in which the ratio of the maxRPKM_25 between the two genotypes was ≥ 2 were also removed. For junctions that appeared in both genotypes, we normalized the junction counts to the isoform expression (maxRPKM_25) to generate the Relative Junction Index (RJI). The log value of RJI was used for two-tailed t tests. Note that statistical corrections for sample size were not used to compute p values for RNA-Seq data, thus these values were only used for relative ranking purposes. To identify differentially expressed junctions with high reliability, we only included the junctions if the median count of junctions within the genotype with higher RJI value was ≥ 3, the ratio of RJI between two genotypes was ≥ 2, and the p value was < 0.05. For intron retention, we only considered reads for further analysis if the maximal median of intron RPKM within one genotype ≥ 2. The maximal RPKM of adjacent exons located to the 5′ and 3′ of the intron (maxRPKM_exon) was recovered for representing the isoform expression. The intron RPKM was normalized to the maxRPKM_exon to generate the Relative Intron retention Index (RII) and the log value of RII was used for two-tailed t tests. To recover retained introns with high reliability, we only included the introns that the ratio of RII between two genotypes was ≥ 2 and the p value was < 0.05.

To associate junctions with genes, junctions were assigned to a given gene if the nearest exon to the donor and acceptor sequence belonged to the same gene in RefSeq annotations, or if the junction matched uniquely to a RefSeq annotated junction. To extract intron length information from RefSeq, annotations were downloaded from UCSC and the length between all annotated exons was recorded. Primers used for RNA-Seq validation are described in Table S2C.

Analysis of Exon Array and RNA-Seq Data Overlap

To analyze the overlap between exon array and RNA-Seq data, we recorded the exon array probe position, which is annotated by the EASANA visualization interface, and localized it in our RNA-Seq data set. For intron retention events detected by exon array, the fold change of the corresponding events from RNA-Seq data was calculated by the ratio of Relative Intron retention Index (RII). For other alternative splicing events detected by exon array, the RNA-Seq junction reads spanning the array probe were recorded if the reads appeared in at least 2 replicates and the ratio of the Relative Junction Index (RJI) was converted into the fold change. If multiple junctions spanned the exon probe, we did not include the event into the comparison analysis. Only 17 non-intron retention events identified by exon array passed these criteria, and our RNA-seq data set indicated 15/17 with the same up-/downregulation direction as detected by exon array. However, these events failed to meet the stringent thresholds set for differential expressed junctions.

SUPPLEMENTAL REFERENCES

Au, K.F., Jiang, H., Lin, L., Xing, Y., and Wong, W.H. (2010). Detection of splice junctions from paired-end RNA-seq data by SpliceMap. Nucleic Acids Res. *38*, 4570–4578.

Clark, T.A., Schweitzer, A.C., Chen, T.X., Staples, M.K., Lu, G., Wang, H., Williams, A., and Blume, J.E. (2007). Discovery of tissue-specific exons using comprehensive human exon microarrays. Genome Biol. *8*, R64.

de la Grange, P., Dutertre, M., Correa, M., and Auboeuf, D. (2007). A new advance in alternative splicing databases: from catalogue to detailed analysis of regulation of expression and function of human alternative splicing variants. BMC Bioinformatics *8*, 180.

de la Grange, P., Dutertre, M., Martin, N., and Auboeuf, D. (2005). FAST DB: a website resource for the study of the expression regulation of human gene products. Nucleic Acids Res. *33*, 4276–4284.

de la Grange, P., Gratadou, L., Delord, M., Dutertre, M., and Auboeuf, D. (2010). Splicing factor and exon profiling across human tissues. Nucleic Acids Res. *38*, 2825–2838.

Gabanella, F., Butchbach, M.E., Saieva, L., Carissimi, C., Burghes, A.H., and Pellizzoni, L. (2007). Ribonucleoprotein assembly defects correlate with spinal muscular atrophy severity and preferentially affect a subset of spliceosomal snRNPs. PLoS One *2*, e921.

Huang, W., Sherman, B.T., and Lempicki, R.A. (2009). Systematic and integrative analysis of large gene lists using DAVID bioinformatics resources. Nat. Protoc. *4*, 44–57.

Kollmus, H., Flohé, L., and McCarthy, J.E. (1996). Analysis of eukaryotic mRNA structures directing cotranslational incorporation of selenocysteine. Nucleic Acids Res. *24*, 1195–1201.

Mortazavi, A., Williams, B.A., McCue, K., Schaeffer, L., and Wold, B. (2008). Mapping and quantifying mammalian transcriptomes by RNA-Seq. Nat. Methods *5*, 621–628.

Munroe, R., and Schimenti, J. (2009). Mutagenesis of mouse embryonic stem cells with ethylmethanesulfonate. Methods Mol. Biol. *530*, 131–138.

Nasim, M.T., Chowdhury, H.M., and Eperon, I.C. (2002). A double reporter assay for detecting changes in the ratio of spliced and unspliced mRNA in mammalian cells. Nucleic Acids Res. *30*, e109.

Pessa, H.K., Ruokolainen, A., and Frilander, M.J. (2006). The abundance of the spliceosomal snRNPs is not limiting the splicing of U12-type introns. RNA *12*, 1883–1892.

Sakharkar, M.K., Perumal, B.S., Sakharkar, K.R., and Kangueane, P. (2005). An analysis on gene architecture in human and mouse genomes. In Silico Biol. (Gedrukt) *5*, 347–365.

Zhao, L., Longo-Guess, C., Harris, B.S., Lee, J.W., and Ackerman, S.L. (2005). Protein accumulation and neurodegeneration in the woozy mutant mouse is caused by disruption of SIL1, a cochaperone of BiP. Nat. Genet. *37*, 974–979.

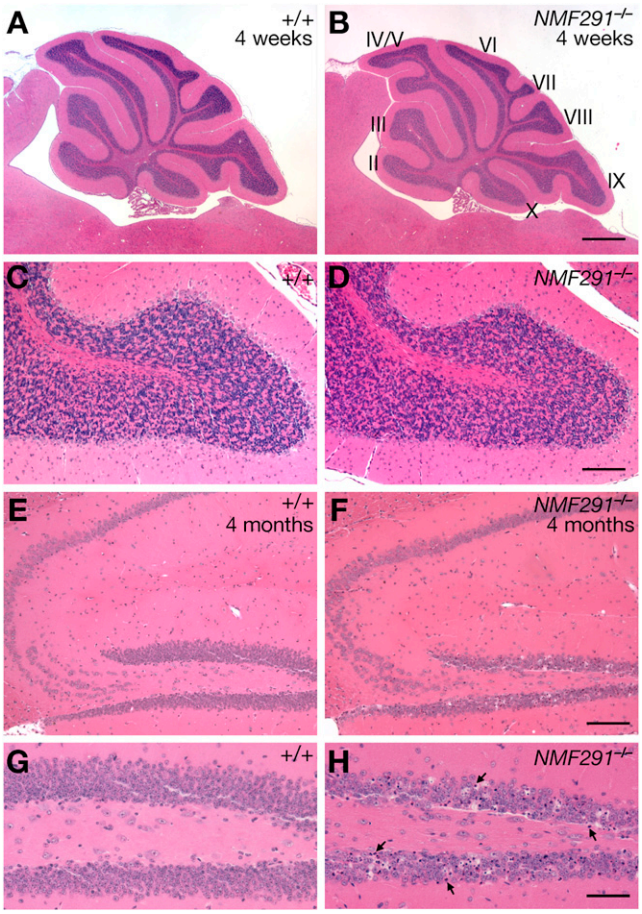

Figure S1. Brain Morphology of *NMF291*$^{-/-}$ Mice, Related to Figure 1

(A–D) Sagittal sections of one-month-old wild-type (+/+, A) and *NMF291*$^{-/-}$ (B) cerebella were stained with hematoxylin and eosin. Cerebellar lobules are indicated by Roman numerals (B). Higher magnification images of lobule IX from wild-type (C) and *NMF291*$^{-/-}$ (D) cerebella.

(E–H) Sagittal sections of the hippocampus of 4-month-old wild-type (E) and *NMF291*$^{-/-}$ (F) mice stained with hematoxylin and eosin. Higher magnification images of the dentate gyrus region from the wild-type (G) and *NMF291*$^{-/-}$ (H) hippocampus. Examples of pyknotic nuclei are labeled by arrows (H). Scale bars: (B), 500 μm; (D), 50 μm; (F), 50 μm; (H), 25 μm.

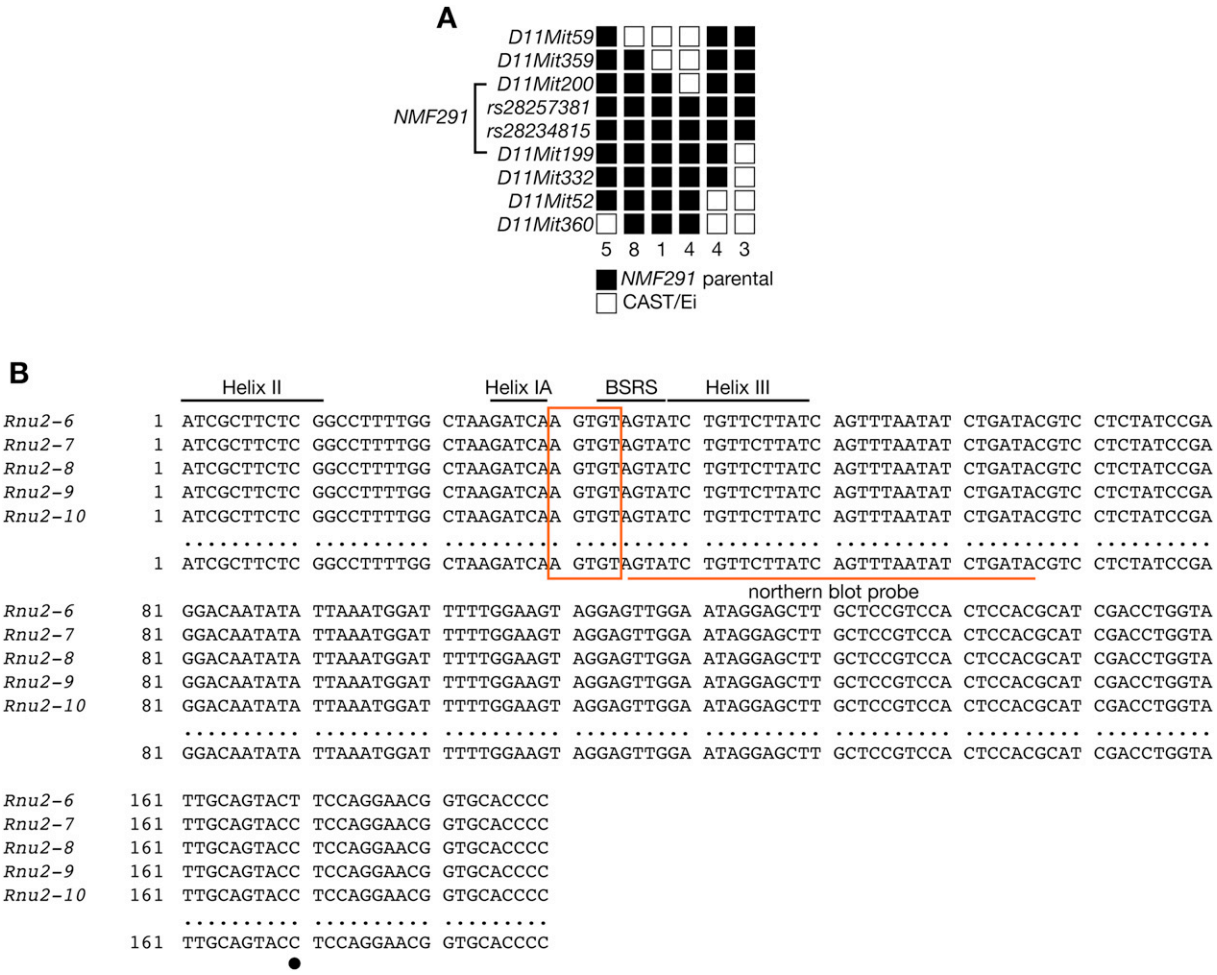

Figure S2. Genetic Mapping of the *NMF291* Mutation and Conservation of *Rnu2-6–Rnu2-10* snRNAs, Related to Figure 2

(A) Haplotypes of recombinant chromosomes from affected mice demonstrated that the *NMF291* mutation is located between *D11Mit200* and *D11Mit199*. The number of mice obtained for each haplotype is shown.

(B) The sequences of *Rnu2-6 – Rnu2-10* snRNAs are identical except for a single nucleotide polymorphism (filled circle) at nucleotide 170 in *Rnu2-6* RNA. The *NMF291* 5-nucleotide deletion is boxed and the U2/U6 Helix Ia, II, and III, and U2 branch site recognition sequences (BSRS) are labeled. The region corresponding to the DNA oligonucleotide probe used for Northern blot analyses is underlined.

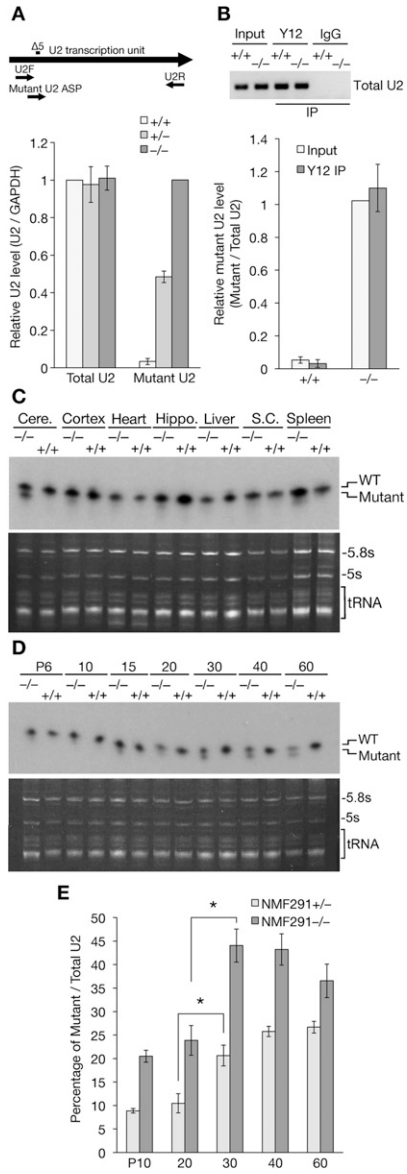

Figure S3. Spatial and Temporal Expression of the Mutant U2 snRNAs and Incorporation of Mutant RNA into Cerebellar U2 snRNPs, Related to Figure 3

(A) Allele specific real-time PCR primers (top) for detecting total U2 snRNA (U2F & U2R) and mutant U2 snRNA (Mutant U2 ASP & U2R) were validated in P30 wild-type (+/+), *NMF291*$^{+/-}$, and *NMF291*$^{-/-}$ cerebellar cDNA (bottom). To generate relative U2 levels, we first normalized total and mutant U2 expression levels to GAPDH levels. Then we defined the wild-type (+/+) normalized total U2 level and *NMF291*$^{-/-}$ normalized mutant U2 level as arbitrary unit one for relative total and mutant U2 expression level, respectively. Note that the relative total U2 snRNA levels in the P30 wild-type, *NMF291*$^{+/-}$, and *NMF291*$^{-/-}$ cerebellum are similar, and that the mutant allele specific primers preferentially (~30 fold) amplify mutant U2 in *NMF291*$^{-/-}$ cerebellar cDNA relative to wild-type U2 in wild-type cerebellar cDNA.

(B) Incorporation of mutant U2 snRNAs into U2 snRNPs in the *NMF291*$^{-/-}$ cerebellum. Immunoprecipitation (IP) experiments were performed using cerebellar supernatants from wild-type and *NMF291*$^{-/-}$ mice. RT-PCR (primers; U2F & U2R, top) detected the total U2 snRNAs present in the input supernatant and in the IP products of the Y12 (*Sm* Antigen) antibody, but not in IP products of the control (normal mouse IgG). Real-time PCR using mutant allele-specific primers demonstrated that the mutant U2 RNAs were present in the mutant input supernatant and Y12 IP products, but not in that of wild-type (bottom).

(C and D) Northern blot analysis of wild-type (+/+) and *NMF291*$^{-/-}$ (–/–) total RNA from P30 neuronal and non-neuronal tissues (C) or from the cerebellum of mice at different postnatal (P) ages (D). The U2 DNA oligo probe for Northern blot is shown in Figure S2B. Ethidium bromide-stained RNA gels are shown as loading controls, and 5.8 s and 5 s rRNA, and tRNA are indicated. Cere, cerebellum; Hippo, hippocampus; S.C., spinal cord.

(E) Quantitative analysis of RNase protection assays performed on *NMF291*$^{+/-}$ and *NMF291*$^{-/-}$ cerebellar RNA at different postnatal (P) ages (days after birth). Values are expressed as the percentage of mutant/total U2 snRNA. Each genotype at each time point was supported by at least three independent mouse samples. *$p < 0.001$, one-way ANOVA.

In all panels, values represent mean ± SEM, n = 3.

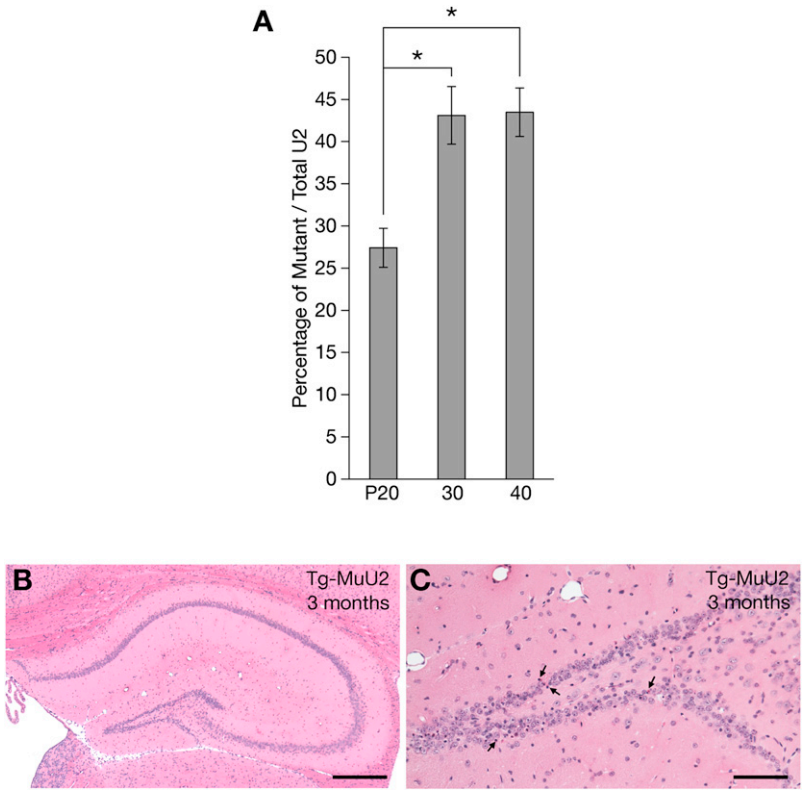

Figure S4. Granule Neuron Loss in Hippocampal Dentate Gyrus Region of Mutant *Rnu2-8* Transgenic Mice, Related to Figure 4

(A) Quantitative analysis of RNase protection assays of Tg-MuU2 mice at different postnatal (P) ages (days after birth). Values are expressed as the percentage of mutant U2 of the total U2 snRNA. Each genotype at each time point was supported by at least three independent mouse samples. *$p < 0.001$, one-way ANOVA. Values represent mean ± SEM, n = 3.

(B and C) Hematoxylin and eosin stained coronal sections of the hippocampus from 3-month-old Tg-MuU2 mice shown at low (B) and higher (C) magnification. Pyknotic nuclei are indicated by arrows (C). Scale bars: (A), 75 μm; (B), 30 μm.

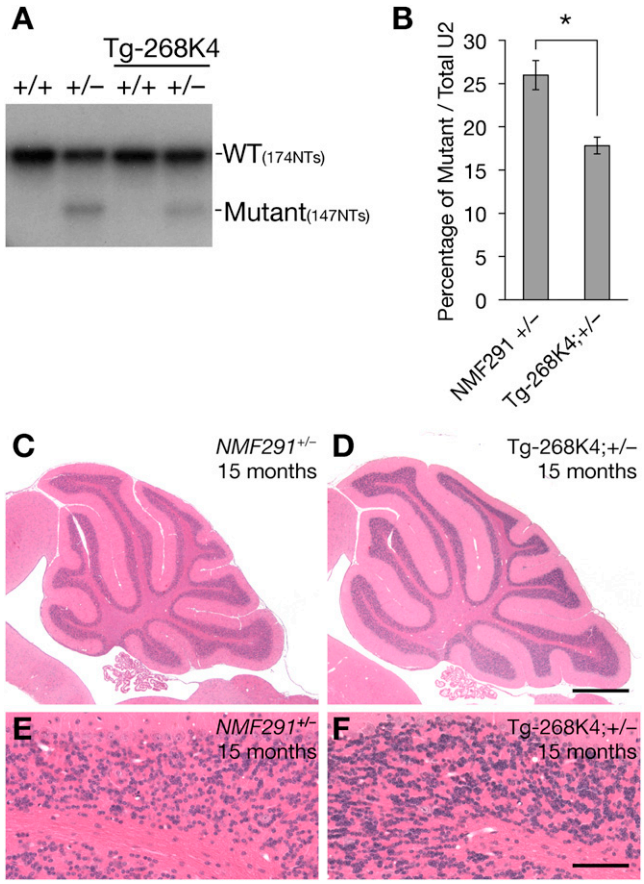

Figure S5. Expression of Wild-Type U2 snRNAs Decreases Neuron Death in Aged Tg-268K4; *NMF291*$^{+/-}$ Mice, Related to Figure 5

(A) RNase protection assays were performed on cerebellar RNA from 15-month-old wild-type (+/+), *NMF291*$^{+/-}$ (+/–), Tg-268K4; +/+, and Tg-268K4; *NMF291*$^{+/-}$ mice.

(B) Quantitative analysis of RNase protection assays of cerebellar RNA from 15-month-old *NMF291*$^{+/-}$ and Tg-268K4; *NMF291*$^{+/-}$ (Tg-268K4; +/–) mice. Values are expressed as the percentage of mutant U2 of the total U2 snRNA. Each genotype was supported by at least three independent mouse samples. *$p < 0.001$, paired t test. Values represent mean ± SEM, n = 3.

(C–F) Hematoxylin and eosin stained sagittal cerebellar sections from aged *NMF291*$^{+/-}$ (+/–; C, E) and Tg-268K4; *NMF291*$^{+/-}$ (Tg-268K4; +/–; D, F) mice. Higher magnification of lobule IV-V is shown in E, F. Note the decreased granule cell loss in the aged Tg-268K4; *NMF291*$^{+/-}$ cerebellum relative to that observed in that of *NMF291*$^{+/-}$ mice. Scale bars: (D), 500 μm; (F), 50 μm.

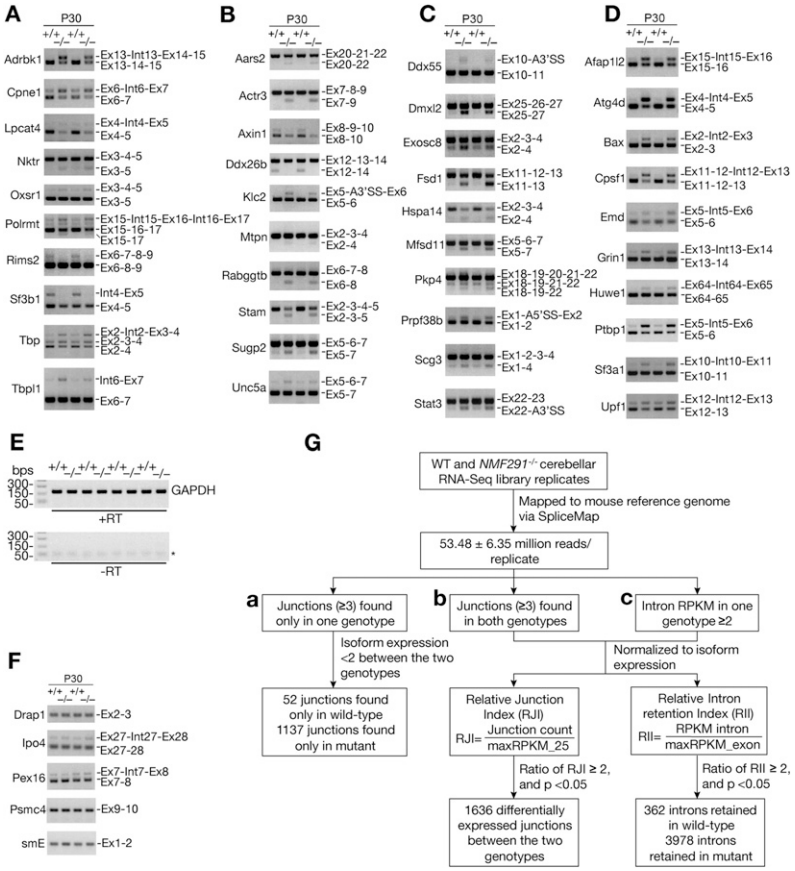

Figure S6. Exon Array and RNA-Seq Analysis, Related to Figure 7

(A) RT-PCR analysis of alternative splicing events predicted to vary between wild-type and *NMF291*$^{-/-}$ mice by exon array analysis. RT-PCR analysis was performed on cerebellar RNA obtained from four pairs of P30 wild-type (+/+) and *NMF291*$^{-/-}$ (–/–) mice, independent of the mice used for the exon array experiment. The identity of RT-PCR products was confirmed by amplicon size and by DNA sequencing. Ten representative reactions from two pairs of wild-type and *NMF291*$^{-/-}$ samples are shown.

(B–D) RT-PCR analysis of junctions differentially expressed between wild-type and mutant cerebella as detected by RNA-Seq analysis. Splicing events in (B) were detected by RNA-Seq as unique junction reads only found in one genotype (median read count $\geq$ 3, and ratio of maxRPKM_25 $\leq$ 2). (C) Junction reads differentially expressed between the two genotypes (ratio of RJI $\geq$ 2, $p < 0.05$). (D) RT-PCR analysis of intron retention events that were predicted by RNA-Seq to increase in the mutant cerebellum. Note these introns were also retained in the wild-type cerebella as a minor form. RT-PCR analysis was performed on cerebellar RNA obtained from four pairs of P30 wild-type (+/+) and *NMF291*$^{-/-}$ (–/–) mice, independent of the mice used for the RNA-Seq experiment. The identity of RT-PCR products was confirmed by amplicon size. Ten representative reactions from two pairs of wild-type and *NMF291*$^{-/-}$ samples (B-D) are shown.

(E) cDNA used for RT-PCR validation of exon array and RNA-Seq analysis was free of genomic DNA contamination. GAPDH was amplified (40 PCR cycles) using a primer pair located within a single exon of the mouse GAPDH gene in the plus RT samples (top), but not in the corresponding minus RT controls (bottom). * indicates PCR primers (bottom).

(F) U12-dependent splicing events were not affected in *NMF291*$^{-/-}$ cerebella. The splicing of five U12-type introns (Pessa et al., 2006) was examined in cerebellar cDNA generated from four pairs of P30 wild-type and *NMF291*$^{-/-}$ mice. The length of *Drap1*, *Ipo4*, *Pex16*, *Psmc4*, and *smE* introns is 85, 117, 85, 182, and 419bps, respectively. Representative gel pictures of reactions from two pairs of wild-type and *NMF291*$^{-/-}$ samples are shown.

(G) RNA-Seq analysis workflow. RNA-Seq libraries were prepared using cerebellar mRNA. Three *NMF291*$^{-/-}$ and two wild-type (WT) mice were used as biological replicates. Libraries were sequenced on an Illumina GAIIX using a 76nt paired-end read strategy and reads were aligned to mouse genome reference via SpliceMap 3.3.6 allowing for a maximum of 4 mismatches. After bar code removal, the length of a mapped read for one end of the pair was 69bp. 53.48 ± 6.35 million reads per replicate were uniquely mapped to the mouse genome. (a) For junctions only found in one genotype, junctions with a median read number $\geq$ 3 were further analyzed. The maximal RPKM of 25bp upstream and downstream of the donor and acceptor site of the adjacent exons (maxRPKM_25) was computed to represent the isoform expression level. Junctions in which the ratio of the maxRPKM_25 $\geq$ 2 between the two genotypes were excluded to avoid potential false positives introduced by differential expression of RNA isoforms between WT and mutant mice. Using these filters, 52 and 1137 junctions were identified as only found in WT and mutant cerebella, respectively. (b) For junctions that were found in both genotypes, we further analyzed those with a median read number $\geq$ 3 for at least one genotype. Junction counts were normalized to the isoform expression (maxRPKM_25) to generate the Relative Junction Index (RJI), and the log value of the RJI was used for a two-tailed t tests. 1636 junctions with a RJI ratio $\geq$ 2 between two genotypes and a p value < 0.05 were identified as differentially expressed between genotypes. (c) For analysis of intron retention, we identified introns with a maximal median of intron RPKM $\geq$ 2 for at least one genotype. The maximal RPKM of adjacent exons (maxRPKM_exon) was computed to represent expression levels of the transcript isoform, and the Relative Intron Retention Index (RII) was generated by normalizing the intron RPKM to the maxRPKM_exon. Two-tailed t tests were performed on the log value of RII. 362 and 3978 introns were identified as differentially retained introns in WT and mutant, respectively, with an RII $\geq$ 2 between the genotypes and a p value < 0.05.